Fall 2017

# Mathematical models for polymer-nematic interactions

Ensela Mema
*New Jersey Institute of Technology*

## ABSTRACT

## MATHEMATICAL MODELS FOR POLYMER-NEMATIC INTERACTIONS

**by**
**Ensela Mema**

This dissertation considers a mathematical model that consists of a nematic liquid crystal layer sandwiched between two parallel bounding plates, across which an external field may be applied. Particular attention is paid to the effect of an applied field on the layer as well as the interaction between the liquid crystal molecules and the molecules of the substrate. The system studied may be considered as a simple model of a Liquid Crystal Display (LCD) device, and the results obtained are discussed and interpreted within this context.

The first part of this dissertation considers a study that investigates how the number and type of solutions for the director orientation within the layer change as the field strength, anchoring conditions and material properties of the nematic liquid crystal layer vary. During this investigation, particular attention is paid to how the inclusion of flexoelectric effects alters the Freedericksz and saturation thresholds.

In the second part of the dissertation, the interaction between nematic liquid crystal (NLC) and polymer coated substrates with and without an external applied field is considered. Under certain conditions, such polymeric substrates can interact with the NLC molecules, exhibiting a phenomenon known as *director* gliding or *easy axis* gliding. Mathematical models for gliding, inspired by the physics and chemistry of the interaction between the NLC and polymer substrate are presented. These models, though simple, lead to non-trivial results, including loss of bistability under gliding. Perhaps surprisingly, it is observed that externally imposed switching between the steady states of a bistable system may reverse the effect of gliding, preventing loss of bistability if switching is sufficiently frequent. These findings may be

of relevance to a variety of technological applications involving liquid crystal devices, and particularly to a new generation of flexible Liquid Crystal Displays (LCDs) that implement polymeric substrates.

Finally, this dissertation considers how well the proposed models fit published experimental data. The results of two experimental papers are discussed, and a quantitative fit of the mathematical model to the data is made.

# MATHEMATICAL MODELS FOR POLYMER-NEMATIC INTERACTIONS

by
Ensela Mema

A Dissertation
Submitted to the Faculty of
New Jersey Institute of Technology
and Rutgers, The State University of New Jersey–Newark
in Partial Fulfillment of the Requirements for the Degree of
Doctor of Philosophy in Mathematical Sciences

Department of Mathematical Sciences, NJIT
Department of Mathematics and Computer Science, Rutgers–Newark

January 2017

**APPROVAL PAGE**

**MATHEMATICAL MODELS FOR POLYMER-NEMATIC INTERACTIONS**

**Ensela Mema**

---

Dr. Linda J. Cummings, Dissertation Co-Advisor — Date
Professor of Mathematics, New Jersey Institute of Technology

---

Dr. Lou Kondic, Dissertation Co-Advisor — Date
Professor of Mathematics, New Jersey Institute of Technology

---

Dr. Michael R. Booty, Committee Member — Date
Professor of Mathematics, New Jersey Institute of Technology

---

Dr. Ian Griffiths, Committee Member — Date
Royal Society University Research Fellow, Oxford University

---

Dr. Richard O. Moore, Committee Member — Date
Associate Professor of Mathematics, New Jersey Institute of Technology

## BIOGRAPHICAL SKETCH

**Author:** Ensela Mema

**Degree:** Doctor of Philosophy

**Date:** January 2017

### Undergraduate and Graduate Education:

- Doctor of Philosophy in Mathematical Sciences,
  New Jersey Institute of Technology, Newark, NJ, 2017
- Bachelors of Science in Mathematics,
  City University of New York, College of Staten Island, Staten Island, NY, 2011

**Major:** Mathematical Sciences

### Presentations and Publications:

E. Mema, L. Kondic, L.J. Cummings, "A mathematical model for zenithal director gliding in a NLC layer," (In preparation).

E. Mema, L. Kondic, L.J. Cummings, "Effects of flexoelectricity and weak anchoring on a Freedericksz Transition cell," submitted to *Physical Review E* (in review).

E. Mema, L. Kondic, L.J. Cummings, "Effect of an applied electric field on a weakly anchored nonplanar nematic liquid crystal layer," *American Physical Society March Meeting*, Baltimore, MD, 2016.

E. Mema, L. Kondic, L.J. Cummings, "Substrate-induced gliding in a nematic liquid crystal layer," *Physical Review E*, 92, 062513, 2015.

T.G. Anderson, E. Mema, L. Kondic, L.J. Cummings, "Transitions in Poiseuille flow of nematic liquid crystal," *International Journal of Nonlinear Mechanics*, 75, pp. 15-21, 2015.

E. Mema, L. Kondic, L.J. Cummings, "Substrate induced gliding for a nematic liquid crystal layer," *American Physical Society March Meeting*, San Antonio, TX, 2015.

L.J. Cummings, E. Mema, C. Cai, L. Kondic, "Electric-field variations within a nematic-liquid-crystal layer," *Physical Review E*, 90, 012503, 2014.

D.J. Coffield Jr., A.M. Spagnuolo, M. Shillor, E. Mema, B. Pell, A. Pruzinsky, A. Zetye, "A model for Chagas disease with oral and congenital transmission," *PLoS ONE*, 8, e67267, 2013.

*To my parents, Shkelqim and Luljeta; my sisters, Eralda and Rediola; and my boyfriend, Eric. Thank you for your endless support and encouragement throughout the years.*

## ACKNOWLEDGMENT

I would like to express my deepest gratitude to my advisors Profs. Linda J. Cummings and Lou Kondic for their endless patience, support and guidance throughout the years. I have been very fortunate to have two extremely caring advisors, always available to answer my questions, sometimes even on a weekend. I thank them for giving me the opportunity to work with them, for being patient and understanding during the weeks in which I did not get a lot work done, for always encouraging me to present our work in multiple conferences and workshops, for their immense help in writing and editing multiple manuscripts and countless other reasons.

I would like to thank Professor Michael Booty, Professor Richard Moore and Dr. Ian Griffiths for taking the time to serve on my thesis committee and learn about my project. Their suggestions and critiques are essential in the completion and improvement of this work.

I would also like to thank the Department of Mathematical Sciences for giving me the opportunity to pursue a degree at such a prestigious university. In particular, I would like to thank Eileen Michie for her guidance and support when I had departmental difficulties.

Special thanks go to fellow graduate student Aminur Rahman, Ivana Seric, Szu-Pei Fu, Lenka Kovalcinova, Pejman Sanaei and Michael Lam for the countless discussions and late nights.

Finally, I would like to thank my parents for their endless moral support and encouragement, always doing everything in their power to make my PhD journey easier. I thank my sisters and my boyfriend, who patiently listened to my rants and believed in me even when I did not believe in myself.

This research was supported by the National Science Foundation under grant NSF-DMS-1211713.

## TABLE OF CONTENTS

**TABLE OF CONTENTS**
**(Continued)**

**Chapter** **Page**

## LIST OF TABLES

**Table** **Page**

## LIST OF FIGURES

**Figure** **Page**

## LIST OF FIGURES
## (Continued)

**Figure** **Page**

## LIST OF FIGURES
## (Continued)

**Figure** **Page**

# CHAPTER 1

# INTRODUCTION

Liquid crystals (LC) are used in many aspects of everyday life, ranging from the development of high-strength plastics and mineral slurries to fat transport in our bodies [36]. Such a wide variety of applications has piqued the interest of researchers around the world and has led to the exploration of many aspects of liquid crystals. An exciting direction over the past several decades has been the development of liquid crystal display (LCD) devices [2]. These devices exploit the birefringence property of nematic liquid crystals (NLCs), namely their ability to rotate the plane of polarized light, to obtain two distinct optical configurations: the "bright" and "dark" pixels of the display [46]. A typical LCD device consists of millions of pixels, each consisting of a nematic liquid crystal layer sandwiched between two parallel plates, and crossed polarizers. The amount of light passing through the layer depends on the orientation of the NLC molecules, which in turn depends on the boundary conditions at the plates (the preferred orientation of molecules at the boundaries, known as *anchoring*) and the external forces (usually an applied electric field). When an electric field is applied across the layer, the LC molecules align with the field and cannot rotate the polarized light beam, so that it cannot pass the second polarizer and the pixel remains "dark". On the contrary, if no electric field is applied, the LC molecules have a preferred orientation dictated by the boundary conditions that allows the polarized light beam to be rotated so that it passes the second crossed polarizer, forming a "bright" pixel in the display [46].

An electric field can change the molecular orientation because NLC materials consist of rod-like molecules which have a dipole moment. As such, applying an electric field causes the NLC molecules to align parallel or perpendicular to the electric field direction according to the orientation of their dipole moment. If the dipole

moment is parallel to the long molecular axis then the molecules align parallel to the electric field; in contrast, if it is perpendicular to the long axis then they will align perpendicular to the electric field. In addition to this dielectric effect, the asymmetric and polar nature of the molecules induces a distortion in the form of molecular splay and bend; the so-called "flexoelectric" effect.

The effect of an applied external field on a confined NLC layer has been widely investigated with particular attention paid to the Freedericksz transition cell [18, 23]. A Freedericksz transition cell consists of a NLC layer bounded between two parallel plates where an electric field is applied in a direction perpendicular to the layer. It is observed that, when the anchoring at the bounding plates is strong and planar (parallel to the plates), the nematic director field (representing the local average molecular orientation) aligns parallel to the bounding plates throughout the entire layer when the applied field strength is low. As the applied field increases past a critical value (known as the *Freedericksz threshold*), a new director configuration, which aligns partially with the applied field in the interior of the layer while respecting the strong planar anchoring at the boundaries, is favored energetically [23]. In the presence of weak planar surface anchoring, the same observations hold initially as the field is increased. However now, as the electric field is increased further still, a second critical value, known as the *saturation threshold* is reached. The *saturation threshold* is the magnitude of the applied field at which the director aligns fully with the electric field direction, breaking the anchoring of the director at the surfaces [16, 35]. This is also often called the weak Freedericksz transition phenomenon. In this scenario three steady-state director configurations exist: (i) the director aligns parallel to the anchoring orientation at the boundary; (ii) the director aligns parallel to the electric field; and (iii) the director adopts a nontrivial solution for which there is a balance between surface anchoring and electric field effects.

Previous investigations of the Freedericksz Transition account mostly for the dielectric contribution to the bulk free energy, neglecting flexoelectric effects. Some studies consider the effect of flexoelectricity in a Freedericksz transition cell with strong and weak anchoring [17,19]. In Chapter 3, we consider a Freedericksz transition cell accounting for both dielectric and flexoelectric contributions to the free energy, with anchoring of arbitrary strength at both bounding surfaces. Particular attention is paid to how the inclusion of flexoelectricity affects the Freedericksz and saturation thresholds. We also consider systematically the effect of anchoring strength on the results, and study how changes of the anchoring boundary conditions affect the results.

In a conventional LCD device, as outlined above, the application of an electric field is required to obtain two optically distinct steady states and although conventional LCD technology is widely used in modern electronic devices, such devices have high power consumption (and hence short battery life). *Bistable* technology offers a NLC layer (the pixel) that can sustain two optically distinct steady states in the absence of an applied field [11, 13, 15, 17, 29]. Examples of bistable devices include the Zenithal Bistable nematic Device (ZBD) [7], the Post-Aligned Bistable nematic Device (PABD) [44], the Bistable Nematic (BiNem) device etc [15]. In the ZBD and PABD, bistability is obtained by using a specially shaped cell where the NLC is enclosed between two substrates of a given topography. Because the NLC molecules have a preferred orientation at the boundaries, the shape of the substrate will affect the director orientation throughout the layer; and if the shape is chosen suitably, two stable configurations exist. The BiNem device uses an applied electric field to break the weak anchoring at one of the substrates creating flow effects that lead to a "uniform" and a "twisted" steady state [15]. In a bistable device, an applied field is needed only to switch between states while in a conventional LCD device an applied field is used to create and maintain two distinct states [13].

Cummings *et al.* have investigated possible theoretical designs for bistable nematic LCD devices in [12,13,15] based on the premise that both anchoring strength and orientation can be controlled at a device boundary. Assuming that any chosen combination of anchoring conditions can be engineered, these authors investigate the design parameters that would allow for production of bistable LCD devices. In Chapter 3, we rely on their investigation to tune the anchoring conditions to permit bistability and study how flexoelectricity affects each director configuration in a bistable system and how the Freedericksz and saturation thresholds are affected.

In most LCD technology the boundary surfaces are made out of glass, chosen for its transparency and robust anchoring properties. With the increase in interest in *flexible* electronic devices, polymer-based devices are now the subject of research. Such devices have the potential to improve existing portable devices by offering manufacturing cost reduction, energy savings and better product performance. Using flexible bounding surfaces for a nematic layer to create a LCD device pixel poses additional challenges however. One challenge is the interaction between the substrate and the liquid crystal. Flexible substrates are often coated by polymeric materials such as PVCN-F or polyimide Nissan SE3510 [9,28]. NLC molecules have a preferred orientation (anchoring) at the boundary plates, often dictated by the coating material and/or different mechanical and chemical treatments the substrate undergoes during the manufacture process. Anchoring may be weak or strong. In both cases, the substrate is characterized by an "easy axis", the axis along which the interaction energy between the substrate and liquid crystal molecules is minimized. If anchoring is strong, the NLC molecules align nearly parallel to the easy axis at the boundary. If anchoring is weak, the NLC molecules may deviate from the easy axis, generating a surface and elastic torque, which balance one another. Experiments have shown that if a strong applied torque exists for extended periods of time, the easy axis can slowly rotate, a phenomenon known as *easy axis gliding* or *director gliding* [26–28].

Director gliding may occur at the interface between a NLC and a polymeric surface as a result of prolonged exposure to an external force (e.g., an electric field) [26–28,38,39,42,43] or as a result of a bulk elastic distortion induced by different anchoring conditions (specifically different anchoring angles). Each scenario leads to a slow reorientation of the easy axis which can be observed in the form of image sticking in LCD devices [31]. Image sticking is a phenomenon where an outline (ghost image) of a previously displayed image remains visible on an LCD screen after the image has been removed. This results in a polarization build-up within individual pixels which affects the optical properties of the display.

Two mechanisms have been proposed to describe the gliding phenomenon observed in experiments: the first, introduced by Vetter *et al.* in [42] describes gliding in terms of adsorption/desorption of the LC molecules on the solid substrate as follows: initially the LC molecules are absorbed along the initial direction of the director in the cell. As an electric field is applied across the layer, the director reorients according to the electric field, leading to the absorption of LC molecules along this new direction. As a consequence, the symmetry axes of the angular distribution function of the absorbed molecules reorients as well as the associated easy axis [9].

The second mechanism, proposed by Kurioz *et al.* in [30], describes gliding as follows: due to weak anchoring imposed on the boundary, applying an electric field reorients the director on the surface, which drags the flexible fragments of the polymer surface. This results in the reorientation of both the liquid crystal molecules and flexible fragments with the rate determined by the anchoring strength and the liquid crystal-flexible fragment interaction. Both mechanisms describe the gliding phenomenon in the most general way and to our knowledge the mathematical models resulting from each mechanism have not been compared against the experimental data observed [9].

A principal goal of this dissertation is to present a mathematical model that aims to capture both (i) the fast evolution of the NLC molecules within a NLC layer as an electric field is applied perpendicular to the bounding plates and (ii) the slow reorientation of the "easy axis" in the NLC-substrate interface. The dissertation is laid out as follows: in Chapter 2, we derive the basic governing equations that describe the evolution of a director field within an NLC layer in the absence of director gliding. These equations will form the backbone of our subsequent work as we proceed to investigate the effect of the applied field (in particular flexoelectric effects) on the NLC layer (Chapter 3) and then extend the modeling to account for the effects of director gliding (Chapters 4 and 5).

In Chapter 3, we investigate in detail how an applied electric field affects the evolution of the director field, for both weak and strong boundary anchoring, in a Freedericksz Transition cell. We categorize the three solutions that may exist, and explore how the flexoelectric effect affects the stability of each solution (the Freedericksz and saturation thresholds). We also investigate how changes in the anchoring conditions (anchoring strength and orientation) affect solutions, in both monostable and bistable simulations.

In Chapter 4, we move on to consider the director gliding phenomenon, first in the absence of an applied field. We develop two mathematical models that aim to capture the slow dynamics of the easy axis reorientation, driven here by the different anchoring conditions imposed at the two bounding plates. This, together with our neglect of the dielectric and flexoelectric contributions to the free-energy density, permits an analytical solution for the director. In line with what is known about the relative time scales of gliding and director reorientation in the bulk, we consider a quasistatic model in which the director angle depends on time only via the changes in anchoring angles on the long (gliding) time scale. The proposed model permits bistability, and therefore we study this aspect of the system under gliding also.

In Chapter 5, we expand the mathematical models developed in Chapter 4 to capture the easy axis reorientation under prolonged application of an electric field across the NLC layer. Here, we consider the experiments carried out by Joly *et al.* [28] and Buluy *et al.* [9] which present experimental evidence for gliding of the zenithal director angle. We compare the gliding data observed in each experiment with the numerical results obtained from our gliding model and, with appropriate fitting, observe very good agreement between model and data.

In Chapter 6, we summarize the present work and describe possible future extensions of our gliding project.

# CHAPTER 2

## BASIC MATHEMATICAL MODEL

Throughout this dissertation, a star superscript will be used to denote a dimensional physical quantity (unstarred equivalents being dimensionless). We consider a layer of nematic liquid crystal of thickness $h^*$, placed between two parallel bounding surfaces at $z^* = 0$ and $z^* = h^*$ as shown in Figure 2.1. The local average molecular orientation throughout the layer is described by a unit vector director field $\boldsymbol{n}$, which we assume lies in the $(x^*, z^*)$ plane, with its properties varying in the $z^*$-direction only. Hence, we consider a one-dimensional model where the director is expressed in terms of a single angle, $\theta(z^*) \in (-\pi/2, \pi/2]$, the angle the director makes with the $z^*$-axis: $\boldsymbol{n} = (\sin\theta, 0, \cos\theta)$. We assume that an electric field $\boldsymbol{E}^* = E^*(0, 0, 1)$ is applied in the $z^*$-direction, perpendicular to the bounding plates. The generated field is assumed to be uniform everywhere as if the field were applied in vacuo. In reality, the molecules of the NLC layer contain electric dipoles that interact with the applied field, causing it to deviate from its uniform state. However, it has been demonstrated [14] that the uniform field approximation is good under certain conditions, which we will discuss later in Chapter 3.

The mathematical model is based on the Ericksen-Leslie continuum theory for nematics [21,32,33], where the total energy density of a liquid crystal layer comprises bulk and surface energy densities, that are functions of the director orientation $\boldsymbol{n}$. To simplify the model, we make the common assumption that the bend and splay elastic constants of the NLC are equal in magnitude [18, 41]. In the presence of a uniform electric field, the bulk energy density consists of the elastic, dielectric and

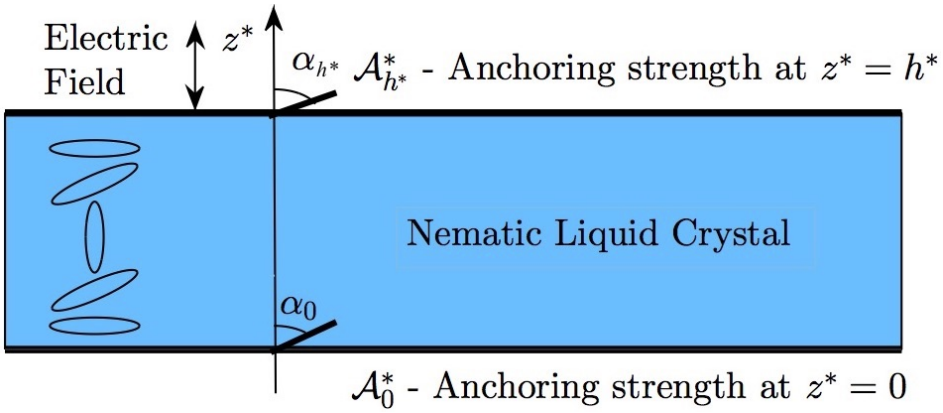


**Figure 2.1** Sketch showing the setup and summarizing the key parameters in dimensional coordinates.

flexoelectric contributions $W_e^*, W_d^*, W_f^*$ given by [10, 18, 41]

$$2W_e^* = K^*[(\nabla^* \cdot \boldsymbol{n})^2 + ((\nabla^* \times \boldsymbol{n}) \times \boldsymbol{n})^2], \tag{2.1}$$

$$2W_d^* = -\varepsilon_0^*(\varepsilon_\parallel - \varepsilon_\perp)(\boldsymbol{n} \cdot \boldsymbol{E}^*)^2, \tag{2.2}$$

$$W_f^* = -\boldsymbol{E}^* \cdot (e_1^*(\nabla^* \cdot \boldsymbol{n})\boldsymbol{n} + e_3^*(\nabla^* \times \boldsymbol{n}) \times \boldsymbol{n}), \tag{2.3}$$

where $K^*$ represents the single elastic constant for the NLC (i.e. $K^* = K_1^* = K_3^*$). The constant $\varepsilon_0^* = 8.854 \times 10^{-12}$ $\mathrm{C^2N^{-1}m^{-2}}$ is the permittivity of free space and $\varepsilon_\parallel$ and $\varepsilon_\perp$ are the relative dielectric permittivities parallel and perpendicular to the long axis of the nematic molecules. We consider the common case in which the NLC molecules align parallel with the electric field (rather than perpendicular to it) hence $\varepsilon_\parallel - \varepsilon_\perp > 0$. The constants $e_1^*$ and $e_3^*$ are the flexoelectric coefficients, different for each liquid crystal type. The flexoelectric effect typically arises because NLC molecules possess shape asymmetry [5,8]. A detailed investigation of the effect of flexoelectricity on the NLC layer can be found in Chapter 3.

The total free energy of the system $J^*$ (per unit area of bounding plates) is given by

$$J^* = \int_0^{h^*} W^* dz^* + g_0^*|_{z^*=0} + g_{h^*}^*|_{z^*=h^*} \tag{2.4}$$

where $g^*_{\{0,h^*\}}$ are the surface anchoring energies at boundaries $z^* = 0, h^*$ and, under the assumptions outlined above, $W^* = W^*_e + W^*_d + W^*_f$ simplifies to

$$W^* = \frac{K^*}{2}\theta^2_{z^*} - \frac{E^{*2}\varepsilon^*_0(\varepsilon_\parallel - \varepsilon_\perp)}{2}\cos^2\theta + \frac{E^*(e^*_1 + e^*_3)}{2}\theta_{z^*}\sin 2\theta. \tag{2.5}$$

For the surface energy contributions, we use the Rapini-Papoular form [40]: $g^*_{\{0,h^*\}} = (\mathcal{A}^*_{\{0,h^*\}}/2)\sin^2(\theta - \alpha_{\{0,h^*\}})$, where $\alpha_{\{0,h^*\}}$ are the preferred anchoring angles at $z^* = 0, h^*$, respectively, and $\mathcal{A}^*_{\{0,h^*\}}$ are the associated anchoring strengths. From a formal mathematical viewpoint, surface anchoring is strong if the molecules at each surface align exactly with the preferred anchoring angles at the corresponding surfaces; and it is weak if the molecules may deviate from the preferred orientation. Strictly speaking therefore, strong anchoring is achieved only in the limit $\mathcal{A}^* \to \infty$.

We follow several authors (e.g., Kedney and Leslie [29], Davidson and Mottram [17], Cummings *et al.* [13]) in assuming that the system evolves as a gradient flow to its total free energy minimum. This process can be represented as follows:

$$\langle \mu^*\theta_{t^*}, \eta\rangle + \langle W^*_\theta, \eta\rangle + \langle W^*_{\theta_{z^*}}, \eta_{z^*}\rangle + [\tilde{\nu}^*\eta\theta_{t^*} + \eta g^*_{h^*\theta}]|_{z=h^*} + [\eta\tilde{\nu}^*\theta_{t^*} + \eta g^*_{0\theta}]|_{z=0} = 0,$$

where $\eta$ is a sufficiently smooth test function and the parameters $\mu^*$ and $\tilde{\nu}^*$ represent the bulk and surface rotational viscosities associated with the NLC molecules (see [13, 17, 29]). The angle brackets here represent an inner product, $\langle a, b\rangle = \int_0^{h^*} ab\ dz^*$. Integration by parts leads to the following evolution equation and boundary conditions:

$$\mu^*\theta_{t^*} = K^*\theta_{z^*z^*} - \frac{\varepsilon^*_0(\varepsilon_\parallel - \varepsilon_\perp)E^{*2}}{2}\sin 2\theta, \tag{2.6a}$$

$$\tilde{\nu}^*\theta_{t^*} = K^*\theta_{z^*} - \frac{\mathcal{A}^*_0}{2}\sin 2(\theta - \alpha_0) + \frac{E^*(e^*_1 + e^*_3)}{2}\sin 2\theta\bigg|_{z^*=0}, \tag{2.6b}$$

$$-\tilde{\nu}^*\theta_{t^*} = K^*\theta_{z^*} + \frac{\mathcal{A}^*_{h^*}}{2}\sin 2(\theta - \alpha_{h^*}) + \frac{E^*(e^*_1 + e^*_3)}{2}\sin 2\theta\bigg|_{z^*=h^*}. \tag{2.6c}$$

So far, we have derived a mathematical model that describes the evolution of the director field in a NLC layer bounded by two parallel plates where a uniform electric field of strength $E^*$ can be applied across the layer. In the following chapters, we build on this basic model to undertake several studies that focus on the effect flexoelectricity and weak anchoring on a Freedericksz Transition cell (Chapter 3); the effect of director gliding driven solely by different anchoring conditions at the two cell boundaries (Chapter 4); and the effect of director gliding driven by prolonged application of an electric field across the layer (Chapter 5). A combination of analytical and numerical techniques will be used to address these problems.

# CHAPTER 3

# EFFECTS OF FLEXOELECTRICITY AND WEAK ANCHORING ON A FREEDERICKSZ TRANSITION CELL

## 3.1 Introduction

This chapter focuses on the effects of flexoelectricity and weak anchoring in a Freedericksz Transition cell (Figure 2.1; in the classical case $\alpha_0 = \alpha_1 = \pi/2$ [6,19,35]) and when the anchoring conditions (anchoring strength and anchoring angles) vary. The flexoelectric effect typically arises because NLC molecules possess shape asymmetry [5, 8]. When they align in an electric field, distortions may be induced. For example, if molecules are slightly pear-shaped, being fatter at one end than the other, then when all the "pears" align in a field a splay distortion will be induced due to the fat ends occupying more space than the thin ends. Similarly, if molecules are slightly banana-shaped, and all the "bananas" align in an electric field, then a net bend distortion results. Flexoelectricity is also possible in symmetric polar liquid crystals such as 5CB. In this case, polar liquid crystals tend to form dimers with antiparallel alignment between molecular dipoles. In the presence of an electric field, the alignment is not completely antiparallel leading to a net polarization which couples to a bend and splay distortion [5, 8].

In this chapter, we investigate the effects of flexoelectricity in a weak Freedericksz transition cell, specifically as regards the number of available director configurations and how transitions between them occur. It is well known that a Freedericksz transition cell consists of three director configurations in the presence of weak anchoring: the horizontal director configuration, observed to be stable when the electric field strength is low (specifically lower than a threshold value called *the Freedericksz threshold*), the director configuration which aligns parallel to the applied field in the interior of the layer while respecting the anchoring conditions at

the boundaries, observed to be stable when the electric field strength is moderate (i.e., past the Freedericksz threshold value); and the director configuration that aligns strictly parallel with the applied field direction, observed when the electric field is increased further, past a second threshold value, known as the *saturation threshold* [35].

The chapter is organized as follows: in Section 3.2, we discuss the nondimensionalization of the governing equations (2.6) presented in Chapter 2. In Section 3.3, we outline our solution strategy, and present selected numerical results, focusing on the effect of flexoelectricity on the director solution. In Section 3.4, we explain the Freedericksz and saturation thresholds and explore how flexoelectricity affects these; and in Section 3.5, we briefly explore how changes in the anchoring conditions affect the results. In our investigation, we focus on the stability of each director configuration, augmenting our numerical results with analytical techniques such as the calculus of variations, and Linear Stability Analysis (LSA), as described in Appendix A. Section 3.6 summarizes our conclusions.

## 3.2 Nondimensionalization of Governing Equations

We nondimensionalize Equations (2.5)-(2.6c) as follows:

$$z = \frac{z^*}{h^*}, \quad t = \frac{t^* K^*}{\tilde{\mu}^* h^{*2}}, \quad W = \frac{h^{*2} W^*}{K^*}, \tag{3.1}$$
$$g_{\{0,1\}} = \frac{g^*_{\{0,h^*\}} h^*}{K^*}, \quad \mathcal{A}_{\{0,1\}} = \frac{h^* \mathcal{A}^*_{\{0,h^*\}}}{K^*},$$

($W$ plays an important role in the calculus of variations approach used in Appendix A) obtaining the following dimensionless boundary value problem:

$$\theta_t = \theta_{zz} - \mathcal{D} \sin 2\theta, \tag{3.2a}$$
$$\tilde{\nu}\theta_t = \theta_z - \frac{\mathcal{A}_0}{2} \sin 2(\theta - \alpha_0) + \frac{\mathcal{F}}{2} \sin 2\theta \quad \text{on} \quad z = 0, \tag{3.2b}$$
$$-\tilde{\nu}\theta_t = \theta_z + \frac{\mathcal{A}_1}{2} \sin 2(\theta - \alpha_1) + \frac{\mathcal{F}}{2} \sin 2\theta \quad \text{on} \quad z = 1, \tag{3.2c}$$

where $\tilde{\nu} = \tilde{\nu}^*/(\mu^* h^*)$ represents the dimensionless surface viscosity and $\mathcal{D}$ and $\mathcal{F}$ represent the relative strengths of dielectric anisotropy and elasticity; and of flexoelectricity and elasticity, respectively:

$$\mathcal{D} = \frac{h^{*2} E^{*2} \varepsilon_0^* (\varepsilon_\parallel - \varepsilon_\perp)}{2K^*}, \qquad \mathcal{F} = \frac{h^* E^* (e_1^* + e_3^*)}{K^*}. \tag{3.3}$$

We consider the common case in which the molecules align parallel to the direction of the electric field, rather than perpendicular to it (i.e, $\varepsilon_\parallel - \varepsilon_\perp > 0$), so $\mathcal{D} > 0$ always in our model. The parameter $\mathcal{F}$ can change sign, if the electric field direction is reversed. The ratio $\Upsilon = \mathcal{F}^2/\mathcal{D}$ is independent of the applied electric field:

$$\Upsilon = \frac{2(e_1^* + e_3^*)^2}{K^* \varepsilon_0^* (\varepsilon_\parallel - \varepsilon_\perp)}. \tag{3.4}$$

$\Upsilon$ is thus a material parameter of the liquid crystal layer, independent of cell design and constant for a specific liquid crystal material.

With characteristic values of $h^* \sim 1 - 20\mu$m, $E^* \sim 1$ V$\mu$m$^{-1}$, $K^* = 8 \times 10^{-12}$N, $e_1^* + e_3^* \sim 5 \times 10^{-12}$Cm$^{-1}$ $- 280 \times 10^{-12}$Cm$^{-1}$ and $\varepsilon_\parallel - \varepsilon_\perp \sim 5$ [8], the dimensionless parameters $\mathcal{F}$ and $\mathcal{D}$ can take a wide range of values ($|\mathcal{F}| \in (5, 125)$ and $\mathcal{D} \in (2, 1100)$). Consistently with this range of values, in Section 3.3, we fix $|\mathcal{F}|$ and $\mathcal{D}$ and vary anchoring strength and field direction (sign($\mathcal{F}$)) to determine the influence on the director configuration throughout the layer. In Section 3.4, we vary $\Upsilon$ (and inherently $\mathcal{F}$) while keeping $\mathcal{D} = 10$ to explore how flexoelectricity affects the Freedericksz and saturation thresholds.

The presentation so far assumes a uniform electric field, but in reality the applied field interacts with the NLC leading to some nonuniformity. Cummings *et al.* [14] studied the validity of the uniform field approximation in our model. They concluded that the approximation is valid in the large field limit, when $|\mathcal{F}| \gg 1$ (with $\Upsilon, \mathcal{A}_0, \mathcal{A}_1 \sim o(|\mathcal{F}|)$) as well as the small field limit (with $\Upsilon \sim |\mathcal{F}| \ll 1$ and $\Upsilon^{-1} \sim |\mathcal{F}| \ll 1$). In the latter case, the director does not feel the nonlinearity that

arises in the electric potential due to the small field strength. Caution should however be exercised in using the uniform field approximation in the case where $\Upsilon \gg 1$ (strong flexoelectric effect) and $|\mathcal{F}| = O(1)$. We present simulation results both in the regime where the uniform approximation is valid and where it may not be. For the latter cases, we note that some corrections to the results may be needed.

The parameters $\mathcal{A}_{\{0,1\}}$ in Equations (3.2) represent the dimensionless anchoring strength at each boundary. In experiments, typical values for strong anchoring hover around $\mathcal{A}^* \sim 10^{-3}\text{Jm}^{-2}$ while $\mathcal{A}^* \sim 10^{-5} - 10^{-6}\text{Jm}^{-2}$ for weak anchoring [37]. Depending on the thickness of the NLC layer, $\mathcal{A}_{\{0,1\}}$ can take a wide range of values $\mathcal{A}_{\{0,1\}} \in (125, 2500)$ (strong anchoring) and $\mathcal{A}_{\{0,1\}} \in (0.125, 25)$ (weak anchoring). Intermediate anchoring strengths are also possible. Consistently with this range of values, in our simulations we use $\mathcal{A}_{\{0,1\}} = 0.1, 1, 5, 10, 20$ to represent weak anchoring and $\mathcal{A}_{\{0,1\}} = 1000$ for strong anchoring. For most of our work here, we consider the case where anchoring is planar at both boundaries, $\alpha_{\{0,1\}} = \pi/2$, with equal anchoring strengths ($\mathcal{A}_0 = \mathcal{A}_1$). This symmetry guarantees monostability (only one stable director configuration for a given electric field strength). In cases where asymmetry is introduced (through anchoring angles), the system can be bistable, admitting two nontrivial director configurations $\theta_{n,1}$ and $\theta_{n,2}$ [13, 15]; such cases are briefly considered in Section 3.5.2.

In the following sections, we use numerical and analytical methods to determine and investigate solutions to the boundary value problem given by Equations (3.2) for various electric field strengths accounting for both dielectric and flexoelectric contributions. In particular, we focus on how the stability of each director solution changes with the electric field strength, and with the material parameter $\Upsilon$, which characterizes the strength of flexoelectricity relative to elasticity. We also extend our investigation to determine the influence of variations in the anchoring strength and angles at the boundaries in both monostable and bistable systems.

### 3.3 Solution Scheme and Numerical Results

We begin by illustrating some key features of the director configurations in the classical case where the anchoring at each boundary is planar ($\alpha_{\{0,1\}} = \pi/2$) and the layer is subjected to an applied perpendicular electric field. Both "strong" and "weak" anchoring are considered. In our numerical simulations, we solve the boundary value problem given by Equations (3.2) using the Crank-Nicolson discretization scheme for the linear parts of the equations. Nonlinear terms are treated explicitly using the forward Euler discretization scheme [4]. A grid size $\Delta z = 10^{-3}$ and $\Delta t = 10^{-4}$ is found sufficient to produce accurate results in all cases considered.

Except where explicitly stated otherwise, the initial condition on all of our simulations is taken as $\theta(z, 0) = \pi z/4$. We note, however, that except for some simulations of Section 3.5.2 (where asymmetric anchoring conditions may lead to bistability), all scenarios considered are monostable, and the final state reached is independent of the initial condition used. Figure 3.1 shows the evolution of the director field in time for two cases: (i) when no electric field is applied across the layer, (ii) when an electric field of moderate strength characterized by $|\mathcal{F}| = 5$ and $\mathcal{D} = 25$ is applied. Strong and weak planar anchoring represented by $\mathcal{A}_{\{0,1\}} = 1000$ (Figure 3.1(a)) and $\mathcal{A}_{\{0,1\}} = 5$ (Figures 3.1(b), 3.1(c)), with $\alpha_{\{0,1\}} = \pi/2$, are considered; for both cases we observe that, in the absence of an electric field, the director evolution is driven purely by the anchoring angles, hence we obtain a director solution that is parallel to the bounding plates ($\theta(z, t) = \pi/2$) throughout the domain (black horizontal lines). In the presence of an electric field however, we expect the molecules to tend to align parallel to the electric field direction since $\mathcal{D} > 0$.

Consistently with our expectations, we observe that for a strongly anchored system (Figure 3.1(a)), the director aligns nearly parallel to the applied field in the interior of the layer and nearly parallel to the walls close to the boundaries (See red lines in Figure 3.1(a)). Although our model includes both dielectric

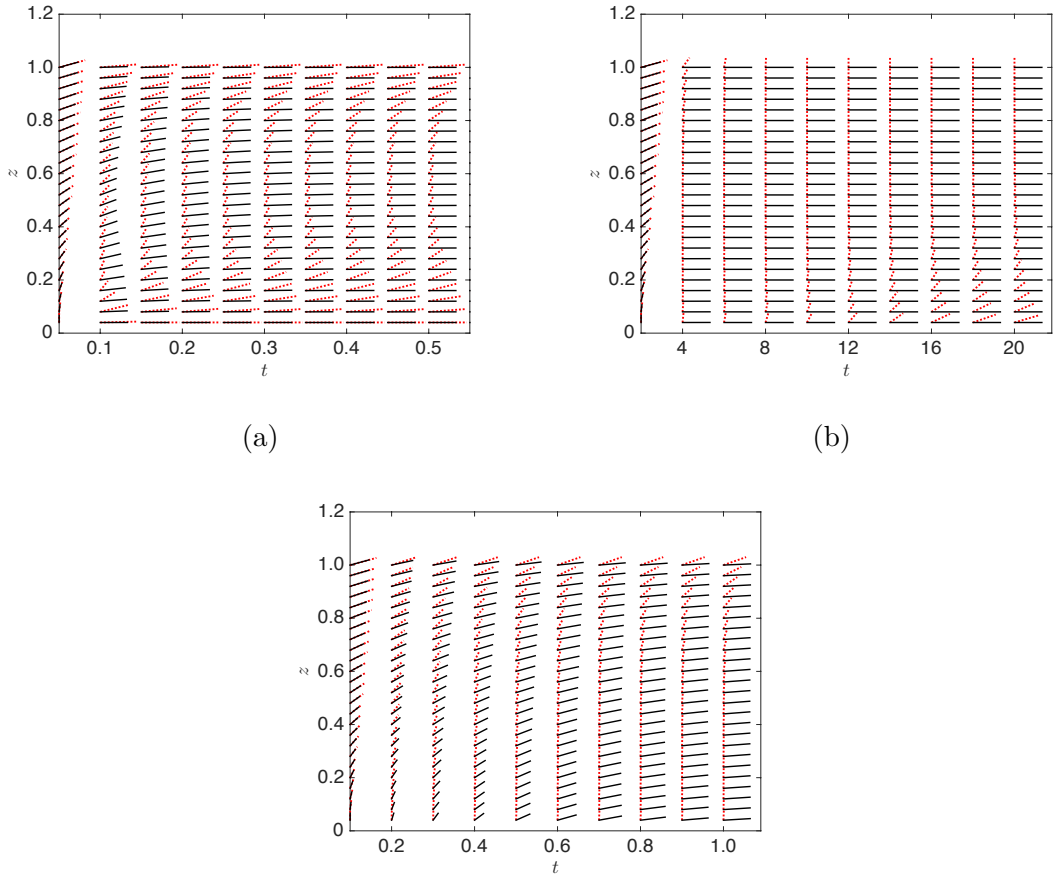


(a) (b)

(c)

**Figure 3.1** Evolution of director field in time for $\alpha_{\{0,1\}} = \pi/2$, with (a) $\mathcal{A}_{\{0,1\}} = 1000$ (strong anchoring), $\mathcal{F} = 5$ and $\mathcal{D} = 25$, (b) $\mathcal{A}_{\{0,1\}} = 5$ (weak anchoring), $\mathcal{F} = 5$ and $\mathcal{D} = 25$ and (c) $\mathcal{A}_{\{0,1\}} = 5$ (weak anchoring), $\mathcal{F} = -5$ and $\mathcal{D} = 25$. All figures show the director evolution in time when no electric field is applied, $\mathcal{D} = \mathcal{F} = 0$ (black lines) and when an electric field of strength $\mathcal{F} = \pm 5$ and $\mathcal{D} = 25$ is applied (red lines).

and flexoelectric contributions, the flexoelectricity is dominated by the surface anchoring in this strongly-anchored case. This may be seen from the boundary conditions, Equations (3.2b)–(3.2c), which are the only place in the model where the flexoelectricity parameter $\mathcal{F}$ and the surface anchoring strengths $\mathcal{A}_{\{0,1\}}$ appear. These boundary conditions suggest that it is the ratio of these two parameters that is key in determining whether flexoelectricity significantly affects the system behavior. We also note from these conditions that, in the symmetric anchoring case considered here ($\mathcal{A}_0 = \mathcal{A}_1$, $\alpha_{\{0,1\}} = \pi/2$), if $\mathcal{F} = 0$, we anticipate symmetry about the layer's centerline $z = 0.5$, but asymmetry when $\mathcal{F} \neq 0$. As the anchoring strength $\mathcal{A}$ increases for fixed $\mathcal{F}$, we would therefore expect that the director configuration observed becomes increasingly symmetric about $z = 0.5$, and this is borne out by Figure 3.1(a), where $\mathcal{F} = 5$ and $\mathcal{A}_{\{0,1\}} = 1000$: the director configuration shown in this figure is almost exactly the same as in the Freedericksz transition cell where the flexoelectric effects are neglected and anchoring is strong [35] (and would be identical to the results of [35] in the formal limit $\mathcal{A}_{\{0,1\}} \to \infty$).

For the weakly anchored system ($\mathcal{A}_{\{0,1\}} = 5$) shown in Figures 3.1(b), 3.1(c) however, we observe significant asymmetry about the cell centerline: the molecules now align parallel to the electric field at the upper boundary $z = 1$ as well as in the interior (see red lines in Figure 3.1(b)). This is a consequence of the asymmetric nature of the molecules discussed earlier which is reflected in the flexoelectric free energy density, see Equation (2.3). Due to the weak anchoring conditions, the flexoelectric distortion plays an important role in the director alignment and hence in the response to the electric field [19, 34, 45]. The direction of the electric field dictates the sign of $\mathcal{F}$. Figure 3.1(c) confirms our expectations that if the sign of $\mathcal{F}$ is reversed, then the director profile is simply reflected about the line $z = 0.5$. For this simple monostable case of symmetric, planar, surface anchoring ($\alpha_0 = \alpha_1 = \pi/2$ and $\mathcal{A}_0 = \mathcal{A}_1$) we next investigate how flexoelectricity changes the steady-state

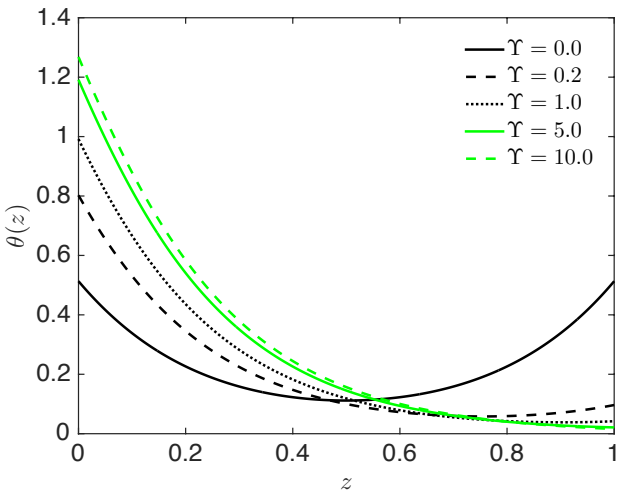


**Figure 3.2** Director solution $\theta(z)$ for different values of the material parameter $\Upsilon$ while keeping $\mathcal{D} = 10$. $\Upsilon = 0$ corresponds to a NLC layer with no flexoelectric contribution. $\Upsilon = 1$ corresponds to the director configuration shown in Figure 3.1(b).

molecular orientation of the NLC layer with weak planar anchoring ($\alpha_{\{0,1\}} = \pi/2$, $\mathcal{A}_{\{0,1\}} = 5$), when an electric field, above the Freedericksz threshold but below the saturation threshold, is applied in the $z$ direction. Neglecting flexoelectricity ($\mathcal{F} = 0$ in Equations (3.2)), but accounting for the weak anchoring, Ref. [35] has shown that a director solution symmetric about $z = 0.5$ is the minimum free energy solution. To study the effects of flexoelectricity we vary the material parameter $\Upsilon$ (given by Equation (3.4)) while keeping $\mathcal{D}$ fixed and observe how the director configuration changes as $\Upsilon$ (and inherently $\mathcal{F}$) is increased. Figure 3.2 shows the steady-state director profiles obtained at large times after solving Equations (3.2) for different values of $\Upsilon$. When $\Upsilon = 0$ (black solid curve), we recover the results of Ref. [35] for weak anchoring but no flexoelectricity. The molecules align nearly parallel to the electric field direction in the interior of the layer while at the boundaries there is a tradeoff between the weak planar anchoring and the field-aligning dielectric effect. As $\Upsilon$ increases (strong flexoelectric effect), the molecules will splay and bend causing the director to align almost parallel to the electric field in the bulk and at the upper boundary. Note that $\Upsilon = 10$ (the largest value used in Figure 3.2) falls under the

case where $\Upsilon \gg 1$ and $\mathcal{F} = \mathcal{O}(1)$, where the uniform field assumption may not be valid [14]. However, assuming that the director solution we calculate here for $\Upsilon = 10$ is not significantly different than that for the true nonuniform field case, we conclude that flexoelectricity plays an important role in the alignment of liquid crystal molecules in the presence of an electric field and it affects the Freedericksz and saturation thresholds.

## 3.4 Stability Analysis and Bifurcations for Symmetric Anchoring Conditions

We now investigate how changing the flexoelectric strength affects the Freedericksz and saturation thresholds in a nematic liquid crystal layer (these thresholds have been extensively studied in the absence of flexoelectricity, see, e.g., [16,18,35,37,41]). In order to do this, we first identify certain properties of Equations (3.2) as well as introduce measures that allow us to quantify our findings. We observe that, with $\alpha_0 = \alpha_1 = \pi/2$, in addition to nontrivial director solutions of the type seen in Figures 3.1 and 3.2 (which we now call $\theta_n$), the boundary value problem (Equations (3.2)) admits two additional steady state solutions that exist for all values of $\mathcal{D}$, $\mathcal{F}$: $\theta_v(z,t) = 0$ (a vertical state) and $\theta_h(z,t) = \pi/2$ (a horizontal state). These solutions are linearly stable only if, when subjected to sufficiently small perturbations, such perturbations die away and the steady state is recovered at large times. Linear stability of each solution type depends on the choice of model parameters, and can be determined either numerically or analytically (see Appendix A for details of our analytical approach). Solutions gain or lose stability as model parameters are varied, and this may be visualized by constructing bifurcation diagrams. In order to construct such diagrams we plot the norm $||\cdot||_2$, of the steady state director solution, defined

as

$$||\theta||_2 = \sqrt{\int_0^1 \theta^2 \, dz}.$$

Since the three distinct solutions $\theta_h$, $\theta_n$, $\theta_v$ have different norms, bifurcations between solution types are clearly visible. Figure 3.3 illustrates the bifurcation diagram obtained by plotting $||\theta||_2$ as a function of $\mathcal{F}$ for several different values of the material parameter $\Upsilon$, which characterizes the strength of the flexoelectric effect. The diagram is obtained using the continuation method as follows: since we anticipate that the horizontal state is a unique steady solution at zero field, we use a weakly perturbed state, $\theta = \pi/2 - \delta$, as the initial condition when $\mathcal{F} = 0$. We then slowly increase $\mathcal{F}$ from $\mathcal{F} = 0$, always using the solution obtained with the previously used smaller value of $\mathcal{F}$ (forward continuation). We also carry out reverse continuation using a similar process: since we anticipate that the vertical state is a unique steady solution at electric field strengths above the saturation threshold ($\mathcal{F} > \mathcal{F}_s$), we use this state with a small perturbation, $\theta = \delta$, as the initial condition for the largest value of $\mathcal{F}$, and thereafter decrease $\mathcal{F}$, at each stage using the previous large-time solution as the new initial condition. When generating our bifurcation diagrams (Figures 3.3–3.9), both forward and reverse continuations are carried out, to reveal any bistability that might be present for a range of electric field strengths. In Figures 3.3 and 3.4 however, we show results for $\mathcal{F} \geq 0$ only (since changing the electric field direction, $\mathcal{F} \to -\mathcal{F}$, simply flips the director solution profile $\theta$ about the centerline $z = 0.5$ (see Figures 3.1(b) and 3.1(c)), leading to bifurcation diagrams symmetric about the vertical axis); and for forward continuation only (since the system is found to be monostable).

For the range of $\mathcal{F}$-values considered here, Figure 3.3 shows that, for small values of $\Upsilon$ (specifically $\Upsilon = 0.5$ and $\Upsilon = 1$), three director configurations are found: the horizontal ($||\theta_h||_2 = \pi/2$) represented by the upper left portion of the graph for

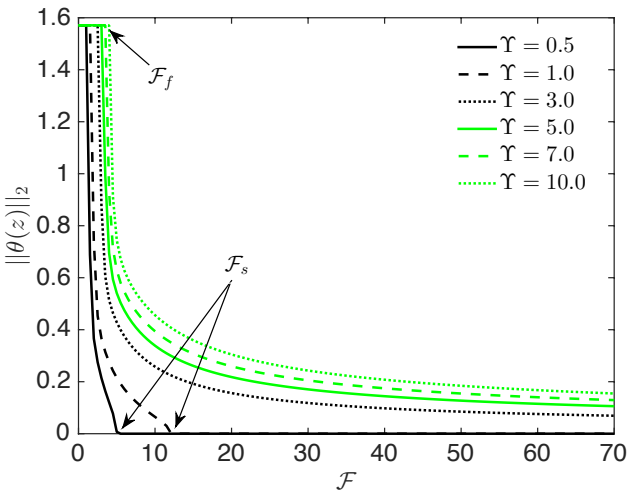


**Figure 3.3** Bifurcation diagram showing $||\theta(z)||_2$ vs $\mathcal{F}$ with $\mathcal{A}_0 = \mathcal{A}_1 = 5$ and $\alpha_0 = \alpha_1 = \pi/2$ for different $\Upsilon$, obtained using continuation in $\mathcal{F}$. $\mathcal{F}_f$ denotes the Freedericksz threshold and $\mathcal{F}_s$ denotes the saturation threshold with the arrows pointing where the thresholds occur for each $\Upsilon$.

all $\Upsilon$, the nontrivial ($0 < ||\theta_n||_2 < \pi/2$) and the vertical ($||\theta_v||_2 = 0$) solutions. In these two cases, the director configuration transitions as follows: at low $\mathcal{F}$ values the horizontal solution $\theta_h$ is obtained. Then, if $\mathcal{F}$ passes a critical value $\mathcal{F}_f$ (Freedericksz transition), the nontrivial solution $\theta_n$ is observed. As $\mathcal{F}$ is increased further still, past a second critical value $\mathcal{F}_s$ (saturation threshold), the vertical solution $\theta_v$ is observed.

These observations are as expected, but the question of how flexoelectricity affects these results has not yet been addressed. Looking at Figure 3.3, we observe that both threshold values increase with $\Upsilon$. While the Freedericksz threshold $\mathcal{F}_f$ is present for all values of $\Upsilon$ considered, the saturation threshold is only seen for the lowest two values of $\Upsilon$, at least for the range of $\mathcal{F}$-values considered here. In order to determine whether the saturation threshold is present for all $\Upsilon \geq 0$, we use an analytical approach based on the calculus of variations. We study specifically the stability of the vertical solution, $\theta_v = 0$. If it can be shown that $\theta_v$ is always stable for sufficiently large $\mathcal{F}$, then we may conclude that a saturation threshold, $\mathcal{F}_s$, should exist, for all $\Upsilon \geq 0$.

The calculus of variations approach proceeds by directly seeking minimizers, $\theta(z)$, of the total free energy $J = h^* J^*/K^*$ (where $J^*$ is defined in Equation (2.4)). Small perturbations to a minimizer, $\theta(z) \to \theta(z)+\epsilon\eta(z), (0 < \epsilon \ll 1)$ induce variations in $J$: $J \to J[\theta+\epsilon\eta] = J_0+\epsilon J_1+\epsilon^2 J_2+\mathcal{O}(\epsilon^3)$. For $\theta(z)$ to be a free energy minimizer, we require $J_1 = 0$ and $J_2 > 0$ for all admissible variations $\eta$ (see Appendix A for more details). Upon obtaining expressions for $J_1$ and $J_2$ (see Equation (A.6–A.8) in Appendix A), it may be seen that, for $\theta(z) = \theta_v = 0$ and any $\Upsilon > 0$, we have $J_1 = 0$, and for sufficiently large $|\mathcal{F}|$ the second variation $J_2 > 0$, hence $\theta(z) = 0$ is a stable solution for such $\mathcal{F}$. It may also be seen from Equation (A.8) that the larger the value of $\Upsilon$, the larger $\mathcal{F}$ must be to guarantee positivity of $J_2$ for all admissible variations $\eta$. Similarly, we are able to show that the horizontal solution $\theta(z) = \theta_h = \pi/2$ is stable for sufficiently small $|\mathcal{F}|$. Hence, the calculus of variations allows us to conclude that inclusion of flexoelectric effects in the model does not affect the fundamental mathematical structure of the system: with the weak anchoring considered here, both Freedericksz and saturation thresholds ($\mathcal{F}_f$ and $\mathcal{F}_s$) always exist, both being increasing functions of $\Upsilon$. We note, for completeness, that the $\Upsilon = 10$ result in Figure 3.3 may lie in the regime where the uniform field approximation begins to lose validity [14].

We next investigate how the strength of the surface anchoring (here assumed the same at both boundaries) affects results, for a fixed value of the material parameter $\Upsilon$. We consider a range of anchoring strength values from $\mathcal{A}_0 = \mathcal{A}_1 = 0.1$ to $\mathcal{A}_0 = \mathcal{A}_1 = 1000$ and obtain a bifurcation diagram by plotting $||\theta||_2$ as a function of $\mathcal{F}$. As shown in Figure 3.4, we observe that both Freedericksz and saturation thresholds are present for all except the largest value of $\mathcal{A}$ used, and both thresholds increase with $\mathcal{A}$. As before, where our numerics are inconclusive we may augment with an analytical approach. The calculus of variations technique outlined earlier again reveals that the vertical solution $\theta_v$ is stable for sufficiently large $\mathcal{F}$ and finite

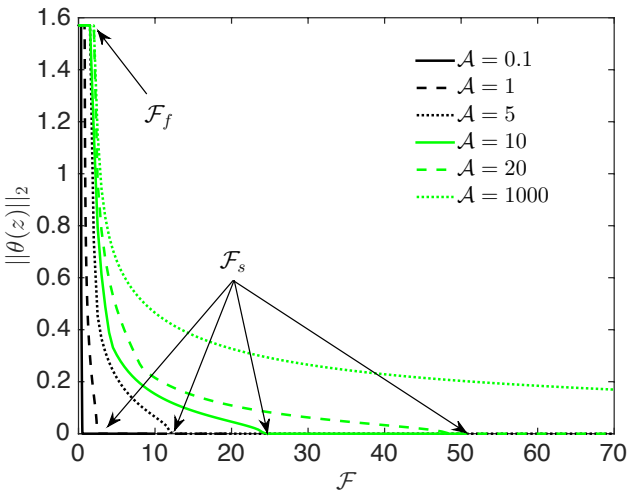


**Figure 3.4** Bifurcation diagram showing $||\theta(z)||_2$ vs $\mathcal{F}$ with $\Upsilon = 1$ for different anchoring strengths: $\mathcal{A}_0 = \mathcal{A}_1 = 0.1, 1, 5, 10, 20, 1000$ obtained using continuation in $\mathcal{F}$. The portion of the diagram where $||\theta||_2 = \pi/2$ represents the horizontal state ($\theta_h(z) = \pi/2$), while $||\theta||_2 = 0$ represents the vertical state ($\theta_v(z) = 0$). The intermediate portion (slowly decaying as $|\mathcal{F}|$ increases) represents the nontrivial solution $\theta_n(z)$ found numerically.

$\mathcal{A}$. Note that in the limit as $\mathcal{A} \to \infty$, positivity of the second variation $J_2 > 0$ (see Equation (A.8) in Appendix A) is not guaranteed, as we recover the Freedericksz transition cell with strong anchoring where the saturation threshold and therefore the vertical solution disappear.

We remind the reader that for the cases considered in Figures 3.3–3.4, the system is monostable: only one steady director configuration is stable for a given electric field strength. In the following section, we consider how breaking the symmetry in the anchoring conditions, specifically, changing the anchoring strength and anchoring angles at each boundary, affects the mathematical structure of the system.

## 3.5 Stability Analysis and Bifurcations for Asymmetric Anchoring Conditions

The coexistence of two (or more) *stable* director configurations gives rise to the potential for development of bistable LCD devices, noted in the introduction. If two stable states exist at zero field then contrast between neighboring pixels could be maintained without use of energy, with an electric field needed only to switch pixels from one configuration to the other as needed [11, 13, 15, 17, 24, 29]. In our model represented by Equations (3.2) we find that breaking the symmetry of the anchoring conditions can lead to bistability. In this section, we see how such bistability arises, and study the effect of flexoelectricity on director profiles, with particular attention paid to how the Freedericksz and saturation threshold are affected.

### 3.5.1 Asymmetric Anchoring Strengths

We begin our investigation into anchoring asymmetry by maintaining planar anchoring at both boundaries ($\alpha_0 = \alpha_1 = \pi/2$), but allowing anchoring strengths to differ. We keep the lower anchoring strength constant at $\mathcal{A}_0 = 10$ and vary the upper anchoring strength in the range $1 \leq \mathcal{A}_1 \leq 12$. We expect the system to retain the same qualitative features of a weak Freedericksz transition cell where all three director configurations ($\theta_h$, $\theta_n$ and $\theta_v$) seen in Figure 3.4 persist despite the different anchoring strengths at each boundary. However, due to the loss of symmetry in the anchoring strength and the inherent dependence of the flexoelectric effect on the direction of the electric field, we now anticipate results for $\mathcal{F} < 0$ to differ from those for $\mathcal{F} > 0$.

Figure 3.5 illustrates the bifurcation diagram, obtained by forward continuation in $|\mathcal{F}|$ from $\mathcal{F} = 0$, showing the stable director configurations for a range of values of $\mathcal{A}_1$. Here, as in Figures 3.3 and 3.4, we use a slightly perturbed horizontal state as an initial condition when $\mathcal{F} = 0$, followed by the solution obtained with the previous electric field strength when $\mathcal{F} \neq 0$ (continuation). For this particular set of

simulations the size of the Freedericksz threshold, $|\mathcal{F}_f|$ increases with $\mathcal{A}_1$ (see inset of Figure 3.5). We also observe that the Freedericksz threshold at positive $\mathcal{F}$, $\mathcal{F}_f^+$, is different than the Freedericksz threshold at negative $\mathcal{F}$, $|\mathcal{F}_f^-|$ for each anchoring strength considered.

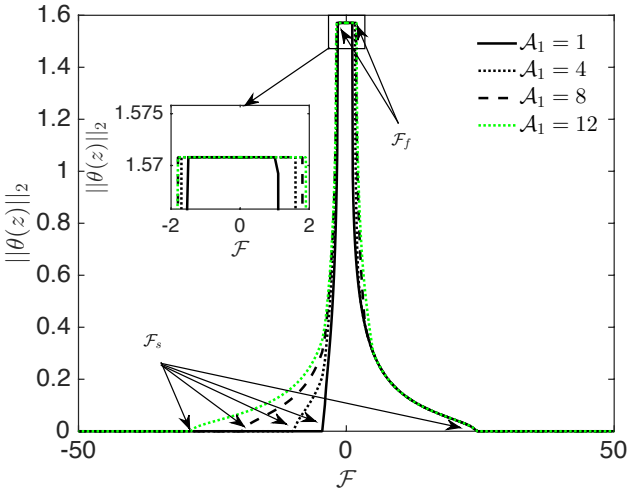


**Figure 3.5** Bifurcation diagram showing $||\theta(z)||_2$ vs $\mathcal{F}$ with $\Upsilon = 1$ for $\mathcal{A}_0 = 10.0$ and $1 \leq \mathcal{A}_1 \leq 12$ using continuation in $\mathcal{F}$.

Figure 3.5 also shows that the saturation threshold at positive $\mathcal{F}$, $(\mathcal{F}_s^+)$ appears to be essentially independent of $\mathcal{A}_1$; but its value at negative $\mathcal{F}$, $(\mathcal{F}_s^-)$ depends strongly on $\mathcal{A}_1$, with $|\mathcal{F}_s^-|$ being an increasing function of $\mathcal{A}_1$. The dependence of the saturation threshold for positive and negative values of $\mathcal{F}$, (denoted by $\mathcal{F}_s^{\{+,-\}}$) on $\mathcal{A}_{\{0,1\}}$ can be understood by considering the behavior of the nontrivial director solution $\theta_n$ with weak anchoring (recall that this solution exists only for $\mathcal{F}$-values between the Freedericksz and saturation thresholds; see, e.g., Figure 3.1 for the symmetric weak anchoring case). Consider the case $\mathcal{F} > 0$ first. It is clear from Figure 3.1(b) that, where $\theta_n$ exists, the director behavior is very different at the two boundaries, respecting the anchoring at $z = 0$ but aligning with the field at $z = 1$. Since the director is already field-aligned at $z = 1$, we would not anticipate that the anchoring strength at that boundary will have much effect on the saturation threshold

value at which the director solution switches to the fully-aligned state – the value of $\mathcal{A}_0$ will be more important. When $\mathcal{F} < 0$ however, the situation is reversed: the director is field-aligned at $z = 0$, while strongly influenced by the surface anchoring at $z = 1$ (Figure 3.1(c)). In this case we expect the value of $\mathcal{A}_1$ to have a significant effect on the saturation threshold, and this is borne out in Figure 3.5.

### 3.5.2 Asymmetric Anchoring Angles

We next investigate how perturbations in the anchoring angles can change the structure of the system; in particular how the Freedericksz and saturation thresholds are affected. We begin by considering a system that is somewhat special: anchoring angles $\alpha_0 = 0$ and $\alpha_1 = \pi/2$ (we call this a semi-symmetric system). The anchoring strengths are set to $\mathcal{A}_0 = \mathcal{A}_1 = 5$ throughout this subsection. Inspection of Equations (3.2) reveals that in this case the horizontal and vertical solutions, $\theta_h = \pi/2$ and $\theta_v = 0$, are still steady solutions, but now we anticipate that $\theta_h$ may no longer be stable at small nonzero fields, since it is favored by just one (not both) boundaries. Hence we expect to see only a saturation threshold as $|\mathcal{F}|$ is increased from zero.

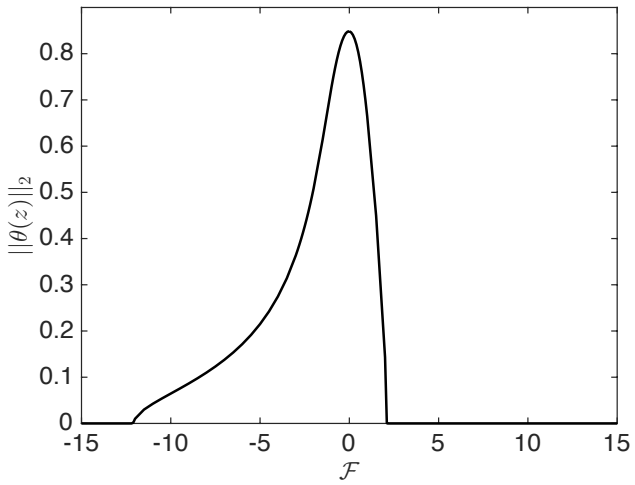


**Figure 3.6** Bifurcation diagram showing $||\theta(z)||_2$ vs $\mathcal{F}$ with $\Upsilon = 1$ for $\mathcal{A}_0 = \mathcal{A}_1 = 5$ and $\alpha_0 = 0$, $\alpha_1 = \pi/2$, obtained using continuation in $\mathcal{F}$.

Figure 3.6 shows the bifurcation diagram for this case. In obtaining the director solutions for each $\mathcal{F}$, we first use $\theta = \pi/2 - \delta$ as an initial guess when $\mathcal{F} = 0$, and thereafter use forward continuation in $|\mathcal{F}|$ (reverse continuation was also carried out with identical results obtained; the system is monostable). We observe that, as anticipated, the horizontal state is never stable. Instead, the system converges to a nontrivial state $\theta_n$, which is stable for small values of $|\mathcal{F}|$. For large enough $|\mathcal{F}|$, the vertical state $\theta_v(z) = 0$ becomes stable while the nontrivial steady state is unstable (or ceases to exist). Therefore, this system does not have a Freedericksz threshold, only a saturation threshold which occurs at $\mathcal{F} \approx -12.5$ for $\mathcal{F} < 0$ and $\mathcal{F} \approx 2.5$ for $\mathcal{F} > 0$. This asymmetry in the saturation threshold is due to the flexoelectric effect.

For $\mathcal{F} > 0$, flexoelectricity helps the director fully align with the electric field at weaker field strength than for $\mathcal{F} < 0$. This can be explained in terms of the nontrivial director configuration for asymmetric anchoring conditions $\alpha_0 = 0$ and $\alpha_1 = \pi/2$. In the absence of an electric field, the director configuration is linear in $z$, satisfying the anchoring conditions Equations (3.2b)–(3.2c) at the boundaries. As an electric field is applied in the positive $z$ direction, the molecules in the bulk and at the upper boundary align with the electric field (c.f. Figure 3.1(b)). Here, however, the molecules at the lower boundary are already aligned with the applied field, hence a fairly low field strength suffices to make the transition from nontrivial to vertical state. On the other hand, when $\mathcal{F} < 0$, the molecules at the upper boundary are dominated by the planar anchoring (c.f. Figure 3.1(c)), and in this case a much higher field is needed to effect the transition from nontrivial to vertical state, confirmed by Figure 3.6.

With a clear picture of the system behavior for the two special cases of (i) equal strength planar anchoring at both boundaries ($\alpha_0 = \alpha_1 = \pi/2$, symmetric case); and (ii) equal strength anchoring that is homeotropic at one boundary and planar at the other ($\alpha_0 = 0$, $\alpha_1 = \pi/2$, semi-symmetric case), we now investigate

how small perturbations to such anchoring conditions change system behavior. We maintain the anchoring strengths $\mathcal{A}_0 = \mathcal{A}_1 = 5$ at each boundary and introduce a small perturbation $\psi$ to the anchoring angles as follows: (i) $\alpha_0 = \pi/2$, $\alpha_1 = \pi/2 - \psi$, (ii) $\alpha_0 = 0$, $\alpha_1 = \pi/2 - \psi$ and (iii) $\alpha_0 = \psi$, $\alpha_1 = \pi/2$. We set $\psi = 0.1$ in all simulations that follow.

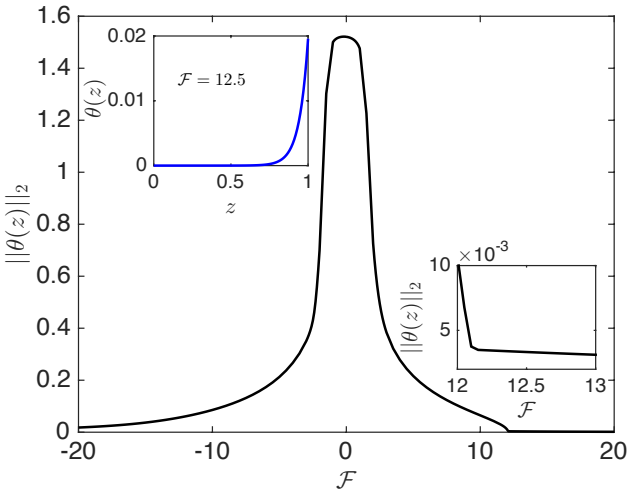


**Figure 3.7** Bifurcation diagram showing $||\theta(z)||_2$ vs $\mathcal{F}$ with $\Upsilon = 1$ for $\mathcal{A}_0 = \mathcal{A}_1 = 5$ and $\alpha_0 = \pi/2$, $\alpha_1 = \pi/2 - \psi$ ($\psi = 0.1$), obtained using forward continuation in $\mathcal{F}$. Inset located at the upper left corner shows the director configuration obtained when $\mathcal{F} = 12.5$. Inset located at the lower right corner shows a zoom of the bifurcation diagram, to clarify the behavior in the range $12 \leq \mathcal{F} \leq 13$ region.

Figure 3.7 shows the bifurcation diagram where $||\theta(z)||_2$ is plotted as a function of $\mathcal{F}$ for $\alpha_0 = \pi/2$ and $\alpha_1 = \pi/2 - \psi$. As in the previous cases, we first use a slightly perturbed horizontal state, $\theta = \pi/2 - \delta$, as initial condition when $\mathcal{F} = 0$, and thereafter use forward continuation in $|\mathcal{F}|$. Since the system is monostable, reverse continuation starting from $|\mathcal{F}| = 20$ with initial condition $\theta = \delta$ leads to identical results. We note that $\theta_h$ and $\theta_v$ are no longer steady state solutions that satisfy Equations (3.2) for the given anchoring angles, hence we do not expect to observe true Freedericksz and saturation thresholds. At zero electric field strength, a nontrivial director solution (nearly horizontal) satisfies the anchoring angles with $||\theta(z)||_2 = 1.52$. As $|\mathcal{F}|$ increases, the nontrivial solution evolves, becoming rapidly

more vertical. Observe that, for $\mathcal{F} \approx 12$, it appears that a saturation threshold is reached, however closer examination (the inset located at the lower right corner in Figure 3.7) reveals that in fact the director never fully breaks the surface anchoring to reach the strictly vertical state $\theta_v = 0$. A boundary layer near $z = 1$ persists (see inset located at the upper left corner of Figure 3.7). Note that the bifurcation diagram shown in Figure 3.7 is far from symmetric in $\mathcal{F}$, being significantly altered from its equivalent (shown in Figures 3.3 and 3.4, reflected about the vertical axis) when $\psi = 0$. This asymmetry is induced purely by the flexoelectric effect. In the absence of flexoelectricity, $\Upsilon = 0$, the bifurcation diagram is symmetric in $\mathcal{F}$.

We now consider perturbations to the system with homeotropic anchoring at one boundary and planar anchoring at the other, with (ii) $\alpha_0 = \psi$, $\alpha_1 = \pi/2$ and (iii) $\alpha_0 = 0$, $\alpha_1 = \pi/2 - \psi$. Once more, $\theta_h$ and $\theta_v$ are no longer steady state solutions that satisfy Equations (3.2) for the given anchoring angles. Hence we do not expect to observe the Freedericksz or saturation thresholds. In fact, both cases (ii) and (iii) are bistable [13, 15], admitting two nontrivial director configurations $\theta_{n,1}$ and $\theta_{n,2}$, hence we must track both solutions in our bifurcation diagrams.

Figure 3.8 shows the bifurcation diagrams for cases (ii) and (iii), where $||\theta(z)||_2$ is plotted as a function of $\mathcal{F}$ for each solution. Since two director configurations exist in the absence of an electric field, we obtain two director solutions for each $\mathcal{F}$ by using $\theta_{n,1}$ and $\theta_{n,2}$ as initial conditions, followed by forward continuation in $|\mathcal{F}|$. In addition, we use a perturbed vertical state $\theta(z) = \delta$ as the initial condition for large $|\mathcal{F}|$, followed by reverse continuation.

Figure 3.8(a) shows the bifurcation diagram for $\alpha_0 = \psi$ and $\alpha_1 = \pi/2$. We observe that when $|\mathcal{F}|$ is small, two stable director configurations given by $\theta_{n,1}$ and $\theta_{n,2}$ exist (solid black line showing the norm of $\theta_{n,1}$ and red dashed line showing the norm of $\theta_{n,2}$). As $|\mathcal{F}|$ increases, one of the solutions disappears; both director solutions have the same norm. Reverse continuation (green dots) converges to the director

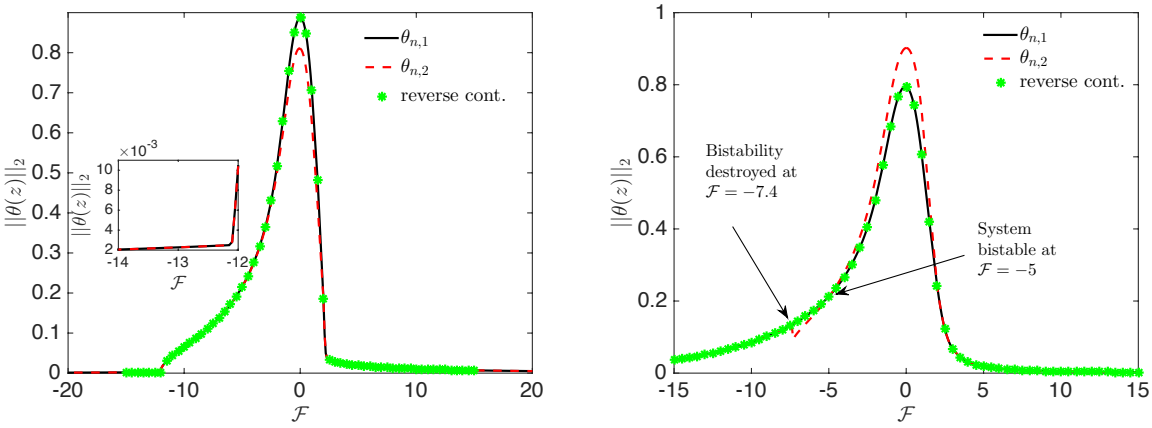


(a) (b)

**Figure 3.8** Bifurcation diagram showing $||\theta(z)||_2$ plotted vs $\mathcal{F}$ with $\Upsilon = 1$ for (a) $\alpha_0 = \psi$ and $\alpha_1 = \pi/2$ and (b) $\alpha_0 = 0$, $\alpha_1 = \pi/2 - \psi$ (with $\psi = 0.1$). Anchoring strengths are set to $\mathcal{A}_0 = \mathcal{A}_1 = 5$. Black solid and red dashed curves are obtained using forward continuation in $|\mathcal{F}|$ while the green dotted curve is obtained using reverse continuation in $|\mathcal{F}|$.

configuration given by $\theta_{n,1}$ which means that one can switch from $\theta_{n,2} \to \theta_{n,1}$ by increasing $|\mathcal{F}|$ but not vice versa. This poses an inconvenience from an applications point of view since, to be useful, a bistable system must allow two-way switching (see [13, 15] for a more detailed investigation of bistability and switching).

As already noted, since $\theta_h$ and $\theta_v$ are not solutions to this perturbed system, there can be no true Freedericksz or saturation threshold. Similarly to Figure 3.7, Figure 3.8(a) has an apparent bifurcation (at $\mathcal{F} \approx -12.5$) but again the inset reveals that the solution is never fully vertical.

Figure 3.8(b) shows the bifurcation diagram for $\alpha_0 = 0$ and $\alpha_1 = \pi/2 - \psi$. As above, we observe that two director configurations $\theta_{n,1}$ and $\theta_{n,2}$ exist for small values of $|\mathcal{F}|$, indicating that the system is bistable. As $|\mathcal{F}|$ increases, the system loses its bistability. Note that for $\mathcal{F} \approx -5$ the two solutions have the same norm in Figure 3.8(b): this does not, however, imply that the director configurations are identical. In fact when $\mathcal{F} \approx -5$, $\theta_{n,1}$ and $\theta_{n,2}$ are distinct solutions, which just happen to have the same $||\theta(z)||_2$ norm, so the system is still bistable here. As $\mathcal{F}$

increases further, however, the system can no longer sustain two stable steady states. Figure 3.8(b) shows that the system loses bistability at $\mathcal{F} \approx -7.4$ for $\mathcal{F} < 0$ and $\mathcal{F} \approx 2$ for $\mathcal{F} > 0$. Beyond these two values the system is monostable. It is curious to note how different the bifurcation structures in Figures 3.8(a) and 3.8(b) are, in particular at negative $\mathcal{F}$-values, while the underlying models are so close.

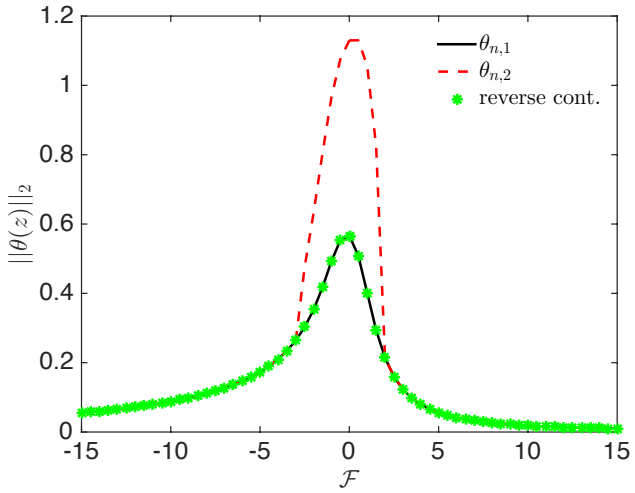


**Figure 3.9** Bifurcation diagram showing $||\theta(z)||_2$ plotted vs $\mathcal{F}$ with $\Upsilon = 1$ for $\alpha_0 = 0$ and $\alpha_1 = \pi/3$. Anchoring strengths are set to $\mathcal{A}_0 = \mathcal{A}_1 = 5$ Black solid and red dashed curves are obtained using forward continuation in $|\mathcal{F}|$ while the green dotted curve is obtained using reverse continuation in $|\mathcal{F}|$.

Finally, we present an example with fully asymmetric boundary conditions, $\alpha_0 = 0$ and $\alpha_1 = \pi/3$. Here as in Figures 3.3–3.8, we plot $||\theta(z)||_2$ as a function of $\mathcal{F}$ by using forward and reverse continuation methods. The behavior of the system is similar to the perturbed semi-symmetric cases shown in Figure 3.8: the system is initially bistable with two director configurations, $\theta_{n,1}$ and $\theta_{n,2}$, and loses bistability as $|\mathcal{F}|$ increases. Also, $\theta_h$ and $\theta_v$ again do not exist, hence there are no Freedericksz and saturation thresholds. As in Figure 3.8, we observe that one can switch only from $\theta_{n,2} \to \theta_{n,1}$ by increasing $|\mathcal{F}|$. Since reverse continuation favors $\theta_{n,1}$, we cannot switch from $\theta_{n,1} \to \theta_{n,2}$ in the asymmetric cases shown here. This finding exemplifies some of the difficulties inherent in designing bistable devices.

Figures 3.5–3.9 have shown that changing the anchoring conditions, even slightly, significantly alters the director configurations present in a Freedericksz transition cell as well as its bifurcation properties (the Freedericksz and saturation thresholds). In particular, we observe that changing the anchoring strength, $\mathcal{A}$, simply increases the Freedericksz and saturation threshold values. Breaking the symmetry in the anchoring angles however, changes the structure of the cell, eliminating the purely horizontal and vertical states present in a classic Freedericksz transition cell. In doing so, one can eliminate both Freedericksz and saturation thresholds.

## 3.6 Conclusions

In this chapter, we use the mathematical model presented in Chapter 2 to describe the evolution of the director field within a confined layer of nematic liquid crystal where an electric field is applied in the $z$ direction and the anchoring conditions vary. We investigate in detail how an applied electric field affects the evolution of the director field in the presence of both dielectric and flexoelectric effects for strong and weak anchoring. We observe that for strong planar anchoring the director aligns vertically in the direction of the electric field in the interior of the layer and aligns nearly parallel to the anchoring angles close to the interface; flexoelectric effects are not observed. In the case of weak planar anchoring, flexoelectricity significantly affects the system's behavior. We find that, at intermediate values of the electric field strength, the director aligns parallel to the electric field in the interior of the layer and at one of the boundaries (which boundary depends on the direction of the electric field). The key characteristics of a weak Freedericksz transition cell persist, however: three director solutions (which we call $\theta_h$, $\theta_n$ and $\theta_v$ for horizontal, nontrivial and vertical states) exist, only one of which is stable at a given electric field strength. Solution $\theta_h$ is stable for $0 < \mathcal{F} < \mathcal{F}_f$ (the Freedericksz transition threshold); solution $\theta_n$ is stable for $\mathcal{F}_f < \mathcal{F} < \mathcal{F}_s$ (the saturation threshold) and solution $\theta_v$ is stable for $\mathcal{F} > \mathcal{F}_s$.

We pay particular attention to the above transition structure when increasing the effect of flexoelectricity by varying the material parameter $\Upsilon = \mathcal{F}^2/\mathcal{D}$ (see Equation (3.4)). We observe that both Freedericksz and saturation thresholds increase with $\Upsilon$ (stronger flexoelectric effect). In addition, we investigate how the Freedericksz and saturation thresholds change as anchoring conditions are varied at each boundary. We show that when the anchoring strength parameters ($\mathcal{A}_{\{0,1\}}$) are varied, the stability of the director configurations does not change, but the Freedericksz and saturation thresholds increase with $\mathcal{A}$. When investigating a system with planar anchoring angles ($\alpha_0 = \alpha_1 = \pi/2$) while varying the anchoring strength only at one boundary, we show that the structure of the system and the saturation threshold at positive $\mathcal{F}$, $\mathcal{F}_s^+$, remain unchanged (three director configurations exist: $\theta_h$, $\theta_n$ and $\theta_v$). The Freedericksz threshold for both positive and negative $\mathcal{F}$, $\mathcal{F}_f^{\{+,-\}}$, and the saturation threshold for negative $\mathcal{F}$, $\mathcal{F}_s^-$, increase in magnitude with $\mathcal{A}_1$. Finally, changing the anchoring angles at the boundaries (nonplanar anchoring angles) reveals that the structure and stability of the possible director configurations changes fundamentally. Here, the horizontal and vertical states are no longer solutions. In some cases bistability is observed, with more than one nontrivial director solution. We find that, while bistability is preserved for weak applied fields, it is typically lost for stronger fields. As the applied field is increased, the system tends to become monostable.

Finally in Appendix A, we present two analytical approaches that help us determine the stability of the director configurations for the weak Freedericksz transition cells. We use the calculus of variations to minimize the total free energy of the system and determine the stability of the horizontal and vertical director configurations. We also carry out Linear Stability Analysis by linearizing Equations (3.2) around the purely vertical and horizontal solutions and we determine

whether perturbations to these solutions exhibit growth or decay in time. We find that our numerical results are strongly supported by the analytical ones.

# CHAPTER 4

# SUBSTRATE INDUCED GLIDING IN A NEMATIC LIQUID CRYSTAL LAYER

## 4.1 Introduction

In this chapter, we present a mathematical model that describes a NLC layer sandwiched between two parallel bounding plates, with different anchoring conditions at each plate, where we assume gliding can occur. As mentioned in Chapter 1, director gliding can occur due to prolonged application of an applied electric field across the layer, or as a result of different anchoring conditions prescribed at each boundary. Here, we focus on the latter case, in which the difference in anchoring angles can lead to a bulk elastic distortion that causes the NLC molecules to deviate from their preferred orientation, leading ultimately to director gliding.

We remark that, although the phenomenon of gliding may occur in both strongly and weakly anchored systems, the model presented in this chapter focuses on gliding in the presence of weak anchoring only, and may require modification before applying to a system with strong anchoring. Furthermore, we focus on gliding of the zenithal (or polar) director angle only, as observed by [28]. We introduce two possible gliding sub-models, and study the effect of each on the director. Although the effect of an applied electric field on gliding is clearly of relevance in applications, we believe that gliding should be first understood precisely in the absence of the field, and that is the focus of this chapter. The model we use permits bistability, and therefore we study this aspect of the system under gliding also.

The chapter is laid out as follows: in Section 4.2 we discuss the modeling assumptions and supplement the mathematical model described in Chapter 2 with two equations used to govern the evolution of the anchoring angles at each surface. One of our modeling assumptions for gliding is that, due to the properties of the polymeric

bounding plates, the anchoring angle cannot change by an arbitrarily large amount from its initial value [27,42]: hence, we limit the change by some prescribed tolerance value, $\alpha_{\text{tol}}$. This assumption is supported by the experimental results reported by Jánossy and Kósa [27], and Joly *et al.* [28]. Section 4.2.1 discusses two possible ways to implement this: in the first, gliding is stopped abruptly when the tolerance is reached; in the second, gliding stops smoothly as $\alpha_{\text{tol}}$ is approached. In addition, Section 4.2 outlines the nondimensionalization process while Section 4.3 presents the results for the two models and Section 4.4 discusses conclusions to be drawn.

## 4.2 Mathematical Model

We will take as our starting point the model given by Equation (2.6) derived in Chapter 2, where the director $\boldsymbol{n}$ is expressed in terms of a single angle, $\theta(z^*) \in (-\pi/2, \pi/2])$. This assumption limits our investigation to gliding of the zenithal or polar director angle only (as observed in [28]), though we note that gliding of the director azimuthal angle may certainly occur in systems with twist, *e.g.*, [27]. With the assumption that the NLC layer is not subjected to any external fields (such as an applied electric field), we can set the electric field strength $E^* = 0$ in Equation (2.6) and obtain the following evolution equations:

$$\begin{aligned} \tilde{\mu}^* \theta_{t^*} &= K^* \theta_{z^* z^*}, \\ \tilde{\nu}^* \theta_{t^*} &= K^* \theta_{z^*} - \frac{{\mathcal{A}_0}^*}{2} \sin 2(\theta - \alpha_0) \quad \text{on} \quad z^* = 0, \\ -\tilde{\nu}^* \theta_{t^*} &= K^* \theta_{z^*} + \frac{{\mathcal{A}_1}^*}{2} \sin 2(\theta - \alpha_{h^*}) \quad \text{on} \quad z^* = h^*. \end{aligned} \tag{4.1}$$

Fundamentally, the anchoring properties of a given polymer surface are due to the orientation of its molecules at the exposed polymer surface, and their interactions with the molecules of the NLC. At a non-gliding surface, the preferred orientation of the molecules is fixed, as dictated by the anchoring conditions. At a gliding

surface, by contrast, the molecules can slowly reorient in time if there is a sustained torque on them due to the molecules of the adjacent NLC. Such a torque arises, for example, if the anchoring conditions within our NLC layer are different at the two bounding surfaces, leading to a director orientation that changes across the layer, with attendant elastic stress throughout the layer (including at the bounding surfaces). Such molecular torques at the bounding surfaces lead to slow variation of the anchoring angles in time: experimentally the anchoring angle is observed to reorient towards the director angle at that surface [22, 25–28, 38, 42]. We introduce two models to capture this gliding behavior. Both models assume that the rate of anchoring reorientation at a surface depends on the difference between the anchoring angle and the director angle at that surface.

The models also incorporate an additional feature, observed in experiments such as those of Jánossy and Kósa [27], Joly *et al.* [28] and Buluy *et al.* [9]: gliding does not continue indefinitely; rather, the anchoring angle stops reorienting after some time under torque. The experimental setup used in [27] consist of a nematic liquid crystal layer placed between two different substrates, only one of which exhibits gliding (azimuthal gliding, rather than the zenithal or polar gliding that we model here but we believe the same mechanisms apply). Anchoring is strong and planar, aligned with a specific rubbing direction, at the upper (non-gliding) substrate; and weak and planar at the lower substrate, where gliding occurs. The layer is exposed to a magnetic field applied perpendicular to the rubbing direction. The anchoring angle at the lower substrate rotates (glides) in time under the magnetic torque. The field is removed after some time (before any steady state is reached, but after significant gliding), and the system is then allowed to evolve under gliding alone. If gliding were unlimited, the system should ultimately glide back to a fully-undistorted state throughout the layer, this being the global energy minimizer. However, this does not happen, indicating that there is some physical constraint on the degree of gliding

that can occur. (Similar observations regarding limited gliding were made by Joly *et al.* [28] and Buluy *et al.* [9] although with a slightly different setup; we discuss these results in detail in Chapter 5.)

Jánossy and Kósa interpret their experimental results by developing a model based on the **Q**-tensor formulation for nematics [18, 27]. Although their model gives very good agreement with the experimental results over reasonable times, it does not capture the fact that the surface director appears not to relax back to its original state in the experiments. By contrast, we base our governing equations on the Ericksen-Leslie theory for nematic liquid crystals. In addition, we account for the observed limited gliding described above by introducing the parameter, $\alpha_{\text{tol}}$, as explained in detail below.

### 4.2.1 Gliding

**4.2.1.1 Gliding Model I: Abrupt Cessation.** In the first gliding model, we assume that the anchoring angle, $\alpha$, changes at a rate directly proportional to its deviation from the adjacent director angle. The anchoring reorientation (gliding) persists until the anchoring angle has changed by a maximal amount $\alpha_{\text{tol}}$ or until $\theta(\cdot, t^*) = \alpha_{\{0,h^*\}}(t^*)$, at which point gliding stops abruptly. Mathematically, this is represented as follows

$$\frac{d\alpha_{\{0,h^*\}}}{dt^*} = \begin{cases} \lambda^*_{\{0,h^*\}}(\theta(\cdot,t^*) - \alpha_{\{0,h^*\}}(t^*)) & \text{if} \quad |\alpha_{\{0,h^*\}}(t^*) - \alpha_{\{0,h^*\}}(0)| < \alpha_{\text{tol}}, \\ 0 & \text{if} \quad |\alpha_{\{0,h^*\}}(t^*) - \alpha_{\{0,h^*\}}(0)| = \alpha_{\text{tol}}, \end{cases} \tag{4.2}$$

where $\theta(\cdot, t^*)$ indicates that $\theta(z^*, t^*)$ is evaluated at the appropriate boundary. Here, $\lambda^*_{\{0,h^*\}}$ are the anchoring relaxation rates at $z^* = 0, h^*$, respectively. When $\alpha_{\text{tol}} = 0$, the interface exhibits no gliding, while as $\alpha_{\text{tol}} \to \pi/2$, the gliding process occurs indefinitely as in the model described in [27]. Unlimited gliding leads ultimately to a

director that is uniform throughout the layer, though this uniform value is unknown *a priori* and will depend on the relative values of the anchoring relaxation rate constants at the two boundaries. The model given by Equation (4.2) introduces gliding in perhaps the simplest possible manner; we will use this simplicity below to gain a better understanding of the basic features of gliding. Before doing so, we introduce our second gliding model.

#### 4.2.1.2 Gliding Model II: Smooth Cessation.

Model I has the advantage of maximal simplicity, but has the perhaps unrealistic feature that gliding halts abruptly once gliding through angle $\alpha_{\text{tol}}$ has occurred. We therefore propose a second gliding model (Model II) with the same essential features as Model I, but here we ensure smooth cessation of gliding by specifying the rate of change of the anchoring angles according to

$$\frac{d\alpha_{\{0,h^*\}}}{dt^*} = \lambda^*_{\{0,h^*\}}[\theta(\cdot,t^*) - \alpha_{\{0,h^*\}}(t^*)]\left(1 - \frac{|\alpha_{\{0,h^*\}}(t^*) - \alpha_{\{0,h^*\}}(0)|}{\alpha_{\text{tol}}}\right). \tag{4.3}$$

Note that the first factor on the right hand side is present in both models, ensuring that the anchoring angle always reorients itself towards the director angle at that interface. The second term leads however to a slowdown of the gliding process as the maximum gliding angle is approached.

### 4.2.2 Scaling and Nondimensionalization

To simplify our models and to identify the important scales, we nondimensionalize. We scale $z^*$ with the cell height $h^*$ and define $t$, the nondimensional time variable, as $t = t^*\lambda^*_0$ where $\lambda^*_0$ is the relaxation rate associated with the lower substrate $z^* = 0$. Relaxation rates can be inferred from experimental data reported in the literature. We use results of Janossy and Kosa [27] to estimate $\lambda^*_{\{0,h^*\}}$. Their experiment consists of a nematic liquid crystal layer sandwiched between two polymer plates where one plate is treated chemically to ensure strong anchoring, while the other is left as a "soft"

plate, exhibiting weak anchoring with gliding. Modifying our model to account for strong anchoring at the plate, $z^* = h^*$, we are able to obtain good agreement between the experimentally-observed evolution of the anchoring angle at the "soft" plate [27] and our model by using $\lambda_0^* \approx 0.0031\,\mathrm{s}^{-1}$ as a relaxation rate in gliding Model I. Hence, we assume this value in our nondimensionalization.

The surface energies $g^*_{\{0,h^*\}}$ (at $z^* = 0, h^*$) are nondimensionalized by $g_{\{0,1\}} = g^*_{\{0,h^*\}} h^*/K^*$ leading to the non dimensional Rapini-Papoular surface energies: $g_{\{0,1\}} = (\mathcal{A}_{\{0,1\}}/2)\sin^2(\theta - \alpha_{\{0,1\}})$, $\mathcal{A}_{\{0,1\}} = (h^*\mathcal{A}^*_{\{0,h^*\}})/K^*$, where $\alpha_{\{0,1\}} \equiv \alpha_{\{0,h^*\}}$. Equations (4.1) in turn become:

$$\begin{aligned} \delta\theta_t &= \theta_{zz} && \text{in} && 0 < z < 1, \\ \delta\tilde{\nu}\theta_t &= \theta_z - \frac{\mathcal{A}_0}{2}\sin 2(\theta - \alpha_0) && \text{on} && z = 0, \\ -\delta\tilde{\nu}\theta_t &= \theta_z + \frac{\mathcal{A}_1}{2}\sin 2(\theta - \alpha_1) && \text{on} && z = 1, \end{aligned} \tag{4.4}$$

where $\delta = h^{*2}\tilde{\mu}^*\lambda_0^*/K^*$ and $\tilde{\nu} = \tilde{\nu}^*/(\tilde{\mu}^* h^*)$. Note that $\delta$ represents the ratio between two timescales: $h^{*2}\tilde{\mu}^*/K^*$ is the time scale of the bulk elastic response of the NLC, while $1/\lambda_0^*$ is the timescale of the gliding response (the estimate above gives a little over 5 minutes for the gliding response, but this timescale may range from a few minutes to several hours depending on the properties of the liquid crystal and the substrate [22, 25, 27, 28, 38]). Typical values of the dimensional parameters for an LCD application are $h^* \sim 1 \times 10^{-6}$ m, $K^* \sim 1 \times 10^{-12}$ N, $\tilde{\mu}^* \sim 0.1$ N s m$^{-2}$, $\mathcal{A}^*_{\{0,h^*\}} \sim 10^{-4} - 10^{-6}$ N m$^{-1}$, $\tilde{\nu}^* \sim 10^{-10}$ N s m$^{-1}$ [17, 20, 26]. Hence the bulk elastic response timescale of the NLC is of the order of a few milliseconds, and $\delta \ll 1$, $\tilde{\nu} \ll 1$. We therefore use a quasistatic approximation and set $\delta = 0$ in Equations (4.4), giving

$$0 = \theta_{zz}, \tag{4.5}$$

$$0 = \theta_z - \frac{\mathcal{A}_0}{2}\sin 2(\theta - \alpha_0) \qquad \text{on} \qquad z = 0, \tag{4.6}$$

$$0 = \theta_z + \frac{\mathcal{A}_1}{2}\sin 2(\theta - \alpha_1) \qquad \text{on} \qquad z = 1. \tag{4.7}$$

The dimensionless forms of the gliding Models I and II given by Equations (4.2) and (4.3) are:

$$\text{Model I:} \quad \frac{d\alpha_{\{0,1\}}}{dt} = \begin{cases} \lambda_{\{0,1\}}(\theta(\cdot,t) - \alpha_{\{0,1\}}(t)) & \text{if} \quad |\alpha_{\{0,1\}}(t) - \alpha_{\{0,1\}}(0)| < \alpha_{\text{tol}}, \\ 0 & \text{if} \quad |\alpha_{\{0,1\}}(t) - \alpha_{\{0,1\}}(0)| = \alpha_{\text{tol}}; \end{cases} \tag{4.8}$$

$$\text{Model II:} \quad \frac{d\alpha_{\{0,1\}}}{dt} = \lambda_{\{0,1\}}[\theta(\cdot,t) - \alpha_{\{0,1\}}(t)]\left(1 - \frac{|\alpha_{\{0,1\}}(t) - \alpha_{\{0,1\}}(0)|}{\alpha_{\text{tol}}}\right), \tag{4.9}$$

where $\lambda_{\{0,1\}} = \lambda^*_{\{0,h^*\}}/\lambda^*_0$ (so $\lambda_0 = 1$ always; and in fact for all simulations shown in this chapter we also set $\lambda_1 = 1$). Equations (4.5)–(4.7) governing the director orientation will be dynamic once supplemented with the gliding model (Equations (4.8) or (4.9)) describing how $\alpha_{\{0,1\}}$ change in time. Note that the actual gliding timescale, $1/\lambda^*_0$, is important only if we wish to convert our dimensionless results back to real time (see Chapter 5 later, where we refine our gliding models and make a quantitative comparison to experimental data).

## 4.3 Analysis and Results

### 4.3.1 Solution Scheme

Equations (4.5)–(4.7) in conjunction with either Equation (4.8) or Equation (4.9) constitute a complete model to describe the director field angle $\theta(z,t)$ within a simple sandwich of NLC with gliding at both interfaces (dynamic evolution of $\alpha_0(t)$, $\alpha_1(t)$). Due to the quasistatic approximation, Equations (4.5)–(4.7) can be solved

independently of the gliding model if the anchoring angles $\alpha_{\{0,1\}}$ are assumed known: $\theta = az + b$ where $a$ and $b$ are fixed by Equations (4.6) and (4.7). Following [13], the director solution may be written as

$$\theta = az + \frac{1}{2}\sin^{-1}\left(\frac{2a}{\mathcal{A}_0}\right) + \alpha_0, \tag{4.10}$$

where $a$ satisfies a nonlinear algebraic equation

$$f(a) = a + a\frac{\mathcal{A}_1}{\mathcal{A}_0}\cos(2a + 2(\alpha_0 - \alpha_1)) + \frac{\mathcal{A}_1\sqrt{\mathcal{A}_0^2 - 4a^2}}{2\mathcal{A}_0}\sin(2a + 2(\alpha_0 - \alpha_1)) = 0 \tag{4.11}$$

(here, the time dependence in $a$, $\alpha_0$, $\alpha_1$ is suppressed for brevity). Given initial conditions $\alpha_0(0)$, $\alpha_1(0)$ for the anchoring angles and values $\mathcal{A}_0$, $\mathcal{A}_1$ for the anchoring strengths, Equations (4.10) and (4.11) describe possible initial states for the system. We choose values of $\mathcal{A}_0$ and $\mathcal{A}_1$ that correspond to "weak anchoring" ($\mathcal{A}^*_{\{0,h^*\}} \sim 10^{-6}\text{N m}^{-1}$). In addition, we expose any behavior due to different anchoring conditions at each substrate by taking unequal values $\mathcal{A}_0 \neq \mathcal{A}_1$: in all simulations presented in this chapter, we take $\mathcal{A}_0 = 5.0$, $\mathcal{A}_1 = 2.4$, as used in [13].

Depending on the values of $\{\alpha_0(0), \alpha_1(0)\}$, Equation (4.11) may have multiple solutions. For the chosen values of $\mathcal{A}_0$, $\mathcal{A}_1$, the number of solutions is always one or three, and we will focus on this case in the rest of the chapter. Choosing different values of $\mathcal{A}_0$ and $\mathcal{A}_1$, however, may lead to more than three solutions, each solution associated with a root of Equation (4.11)). In such cases, the multiple roots of larger amplitude correspond to complex director configurations where the director bends through large angles (greater than $\pi$). These configurations are unlikely to be observed in physical systems due to the associated high elastic energy, and will not be considered further. [Such solutions may be considered an artifact of our assumption of purely 2D geometry: real systems are 3D and the director can "escape" from a

highly-bent 2D solution, unwinding into the third dimension.] When Equation (4.11) has one root, the system has only one steady state (monostability); when it has three roots, the system is bistable (one of the three roots always represents an unstable solution for $\theta$; a local maximum of the free energy).

The results that we present are obtained as follows. From our chosen initial state, integrating either Equation (4.8) or Equation (4.9) through one time step using the appropriate integrating factor, we compute the evolution of the anchoring angles based on Models I and II. These anchoring angles are used to obtain a new director solution using Equations (4.10) and (4.11) at the new time step. To ensure accuracy, we use relatively small time step, $dt = 10^{-3}$; we have verified that this choice of $dt$ leads to results that are accurate to 0.1%.

### 4.3.2 Effect of Gliding on a Monostable System

We focus first on an initially monostable system, and consider how the proposed gliding Models I and II drive the evolution of the anchoring angles and director field under unlimited ($\alpha_{\text{tol}} = \pi/2$) and limited ($\alpha_{\text{tol}} < \pi/2$) gliding (we use $\alpha_{\text{tol}} = \pi/20$ as a representative example). We expect unlimited gliding to smooth the director solution throughout the layer, leading to a uniform solution at large time, while limited gliding may lead to a nonuniform steady state for the director.

Figure 4.1 shows a snapshot of $f(a)$, defined in Equation (4.11), for a monostable system. Figure 4.2(a) shows the evolution of the director field from the initial state represented by the root in Figure 4.1, under unlimited gliding. These results are computed using Model I; results obtained using Model II are very similar and are therefore omitted. Figure 4.2(b) shows the accompanying evolution of the anchoring angles $\alpha_0, \alpha_1$ for both gliding Models I and II. For both models, with $\alpha_{\text{tol}} = \pi/2$, the director field evolves to a solution uniform throughout the layer, with $\theta(z, \infty) = \alpha_0(\infty) = \alpha_1(\infty)$. However, the steady states attained

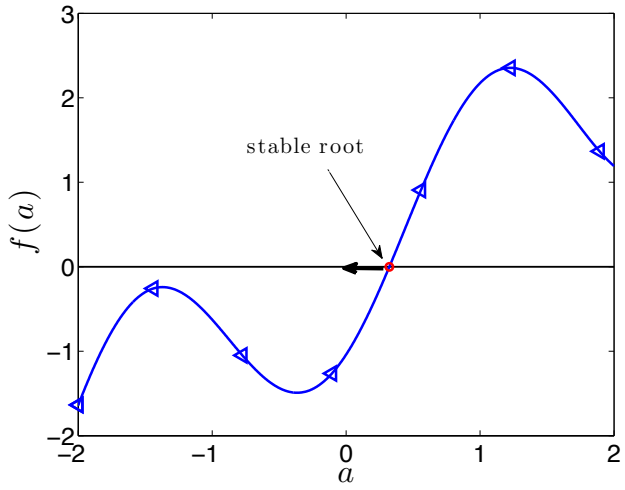


**Figure 4.1** The location of the root of $f(a)$, see Equation (4.11), for a monostable system. The anchoring angles are $\alpha_0(0) = 0$ and $\alpha_1(0) = \pi/6$. The arrow accompanying the root indicates its initial evolution under gliding (Model I). The symbols on the curves shown in this and upcoming figures are purely for identification with the legend, and bear no relation to the mesh-point used.

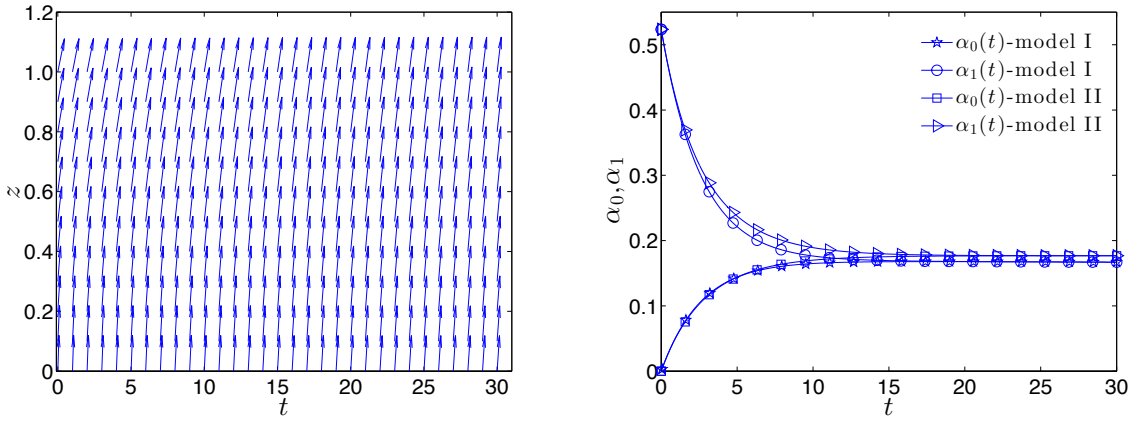


(a) (b)

**Figure 4.2** Gliding effect for $\alpha_{\text{tol}} = \pi/2$ (unlimited gliding) using Models I and II: $\alpha_0(0) = 0$, $\alpha_1(0) = \pi/6$ and $\lambda_0 = \lambda_1 = 1.0$ (these values for the dimensionless relaxation constants are assumed throughout this paper). (a) Evolution of the director field in time as result of gliding Model I. (b) Evolution of anchoring angles for Model I: $\alpha_0(t)$–($\star$), $\alpha_1(t)$–($\circ$); and Model II: $\alpha_0(t)$–($\square$), $\alpha_1(t)$–($\triangleright$).

by the two models are not the same in Figure 4.2(b): the additional smoothing factor $\left(1 - |\alpha_{\{0,1\}}(t) - \alpha_{\{0,1\}}(0)|/\alpha_{\text{tol}}\right)$ in Equation (4.3) becomes important, leading

to quantitatively different results. This observation highlights the importance of accurately capturing the intermediate dynamics in any gliding model (in Chapter 5 later, we present a model with more complicated dynamics, capable of capturing quantitatively the gliding behavior observed in experiments). Note also that, regardless of the model used, $\alpha_1(t)$ varies more from its initial value than does $\alpha_0(t)$ due to the lower associated anchoring strength ($\mathcal{A}_0 = 5.0$, $\mathcal{A}_1 = 2.4$).

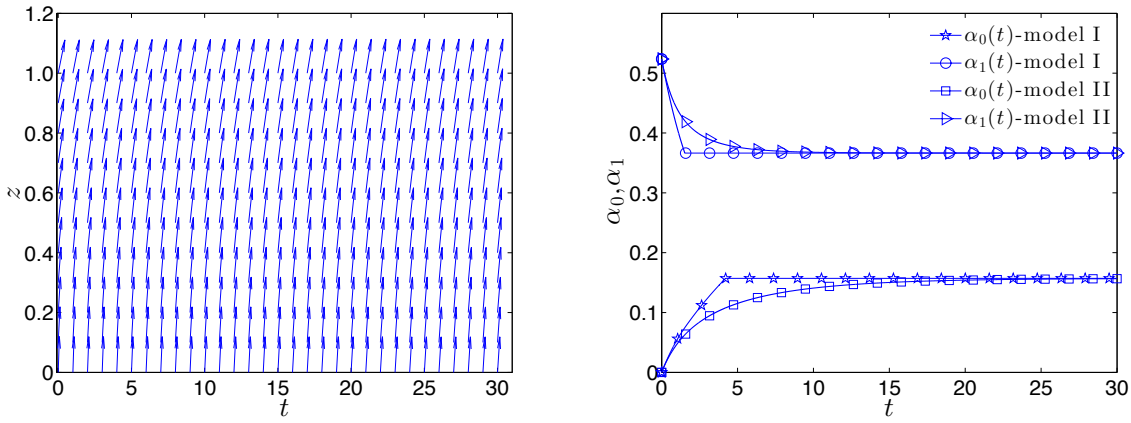


(a) (b)

**Figure 4.3** Gliding effect for $\alpha_{\text{tol}} = \pi/20$ (limited gliding) using Models I and II: $\alpha_0(0) = 0$, $\alpha_1(0) = \pi/6$ and $\lambda_0 = \lambda_1 = 1.0$. (a) Evolution of the director field in time as result of gliding Model I. (b) Evolution of anchoring angles for Model I: $\alpha_0(t)$–($\star$), $\alpha_1(t)$–($\circ$); and Model II: $\alpha_0(t)$–($\square$), $\alpha_1(t)$–($\triangleright$).

Figure 4.3 shows the evolution of the director solution and the anchoring angles under gliding Models I and II for $\alpha_{\text{tol}} = \pi/20$, with all other parameters as in Figure 4.2. We note that the anchoring angles at the two boundaries no longer settle at the same steady state value: $\alpha_0(\infty) \neq \alpha_1(\infty)$ leading to a director solution that is nonuniform throughout the layer at large times. In addition we observe that, unlike the unlimited gliding example of Figure 4.2, under limited gliding the two models lead to the same steady state solution at large times, at least for sufficiently small $\alpha_{\text{tol}}$ as used here. This is due to the fact that, for sufficiently small $\alpha_{\text{tol}}$, gliding stops (for both

models) due to the maximum gliding angle being reached: $|\alpha_{\{0,1\}}(t) - \alpha_{\{0,1\}}(0)| = \alpha_{\text{tol}}$ at finite time (see Equation (4.8) or Equation (4.9)).

### 4.3.3 Effect of Gliding on a Bistable System

The existence of two (or more) stable field-free steady states that are optically distinct is of relevance to applications, since in this case, contrast can be maintained in a display without an externally applied electric field (a field is required only to switch the device from one state to the other). Theoretical investigations of bistable devices have been carried out by many authors: see, eg. [13, 15, 17, 29] and references therein. In [15], bistability is obtained in a special case where the anchoring angles are $\pi/2$ out of phase and the anchoring strengths are the same at both boundaries; switching between the states is obtained through the application of a transient electric field and in particular, two-way switching is possible for weak anchoring only. In [13], Cummings *et al.* generalize the study by treating the anchoring conditions as adjustable parameters, providing the values of $\mathcal{A}_{\{0,1\}}, \alpha_{\{0,1\}}$, for which bistability and switching are possible. In the same spirit, bistability may be achieved in the simple model considered here by appropriate choice of (initial) anchoring conditions: whether the system remains bistable over long times depends on how the anchoring angles evolve under gliding. In this subsection, we consider the effect of gliding on bistable systems by means of specific examples.

Figure 4.4(a) shows an example of the function $f(a)$, defined in Equation (4.11), for a bistable system. The roots of this function determine director solutions as in Equation (4.10); here $f(a)$ has three roots, only two of which represent stable solutions, as discussed below. With anchoring strengths fixed, we find that whether the system specified by Equations (4.5)–(4.7) is bistable (three roots of $f(a)$) or monostable (one root of $f(a)$) depends primarily on the difference of the initial anchoring angles, $\Delta\alpha(0) = \alpha_1(0) - \alpha_0(0)$, with only weak dependence on individual

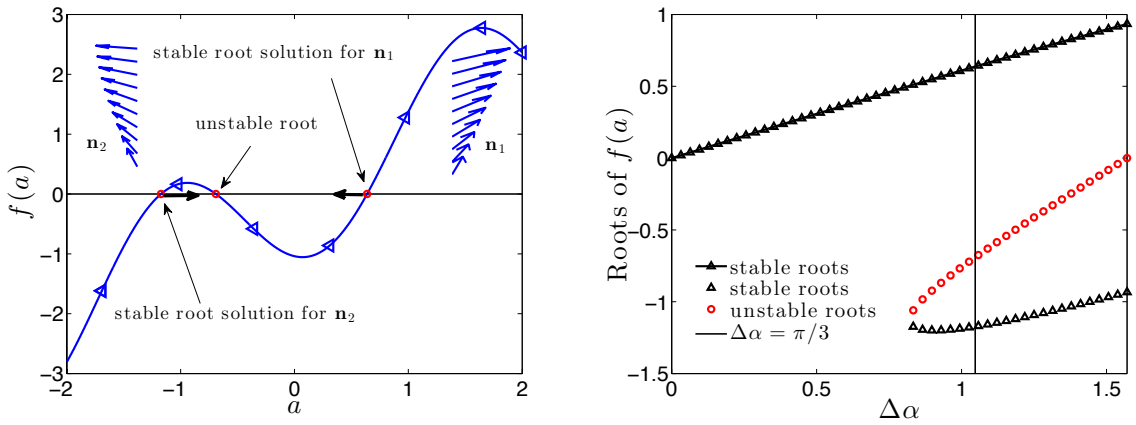


(a) (b)

**Figure 4.4** (a) Location of the roots of $f(a)$ for a bistable system with $\alpha_0(0) = 0$, $\alpha_1(0) = \pi/3$. The arrows accompanying the stable roots indicate their initial evolution under gliding. Two steady state configurations $\boldsymbol{n}_1$ and $\boldsymbol{n}_2$ are shown, corresponding to $a_1 \approx 0.63$ and $a_2 \approx -1.17$. (b) Dependence of solution multiplicity on $\Delta\alpha = \alpha_1(0) - \alpha_0(0)$ where $\Delta\alpha$ varies from 0 to $\pi/2$ with $\alpha_0(0) = 0$. When $f(a)$ (defined by Equation (4.11)) has three roots, two correspond to stable steady states ($\triangle$), and one to an unstable steady state ($\circ$). The vertical line is drawn at $\Delta\alpha(0) = \pi/3$, the state shown in (a).

values of the two anchoring angles; therefore for purposes of illustration we fix $\alpha_0(0) = 0$ and vary $\alpha_1(0)$. Figure 4.4(b) shows how the number of solutions of Equations (4.5)–(4.7) then depends on $\Delta\alpha(0)$. We observe that if $\Delta\alpha(0) = \alpha_1(0) - \alpha_0(0) < \Delta\alpha_c \approx 0.82$, the function $f(a)$, defined by Equation (4.11), has only one root, corresponding to a single solution $\boldsymbol{n} = (\sin\theta, 0, \cos\theta)$, where $\theta$ is given by Equation (4.10). Two stable steady states emerge if $\Delta\alpha(0) > \Delta\alpha_c$: in this case, $f(a)$ has three roots, two corresponding to stable solutions given by Equation (4.10) (local minima of the free energy given in Equation (2.4)), and one corresponding to an unstable solution (local maximum of the free energy). Note that the particular value of $\Delta\alpha_c$ in a given system depends also on the anchoring strengths, $\mathcal{A}_{\{0,1\}}$; in Figure 4.4, as elsewhere, these are set at $\mathcal{A}_0 = 5.0$, $\mathcal{A}_1 = 2.4$.

#### 4.3.3.1 Effect of Unlimited Gliding on a Bistable System.

The discussion presented so far in this section pertains to the initial states of a system before any gliding dynamics are seen. Since gliding can affect the structure of an initially bistable system, we explore its effect below, discussing a specific example. Before doing so, we observe that as the anchoring angles $\alpha_0(t)$, $\alpha_1(t)$ vary under gliding, the function $f(a)$ defined by Equation (4.11) evolves in time as well. In the following, we say that we "track" $\boldsymbol{n}_1/\boldsymbol{n}_2$ when the director solution (given by Equation (4.10)) whose behavior is dictated by the evolution of the largest/smallest root of $f(a)$, evolves under gliding. It is important to emphasize that this evolution under gliding is totally different for each steady state, as we now discuss.

Given values for the surface energies $\mathcal{A}_0$, $\mathcal{A}_1$, and initial values for the anchoring angles, $\alpha_0(0)$, $\alpha_1(0)$, the system has a choice of two steady states, $\boldsymbol{n}_1$ or $\boldsymbol{n}_2$, corresponding to two distinct roots of Equation (4.11). If we start with state $\boldsymbol{n}_1$ and track it under gliding, the anchoring angles will evolve according to the solution of Equation (4.8) or Equation (4.9). Since each of these equations depends on the director solution $\boldsymbol{n}_1$ itself, the evolution here is quite different than if we started from the solution $\boldsymbol{n}_2$.

Note also that, when we track solution $\boldsymbol{n}_1$, the solution $\boldsymbol{n}_2$ corresponding to the other (stable) root of $f(a)$ exists "in the background", but is not manifested. This "background" evolution of $\boldsymbol{n}_2$, when tracking $\boldsymbol{n}_1$, is again quite different from the evolution of $\boldsymbol{n}_2$ when it is the solution being tracked. The following explicit examples should clarify these remarks.

Consider the two possible scenarios for the evolution of $f(a)$ in Figure 4.4(a) with $\Delta\alpha(0) = \pi/3$. Initially this system has two stable steady states, $\boldsymbol{n}_1$ and $\boldsymbol{n}_2$, corresponding to the roots of $f(a)$ as shown in Figure 4.4(a). Figures 4.5(a) and 4.6(a) show the evolution of the director field when tracking $\boldsymbol{n}_1$ and $\boldsymbol{n}_2$ (respectively) under unlimited gliding using Model I. Similarly to the monostable case, independently of

which gliding model we choose, for $\alpha_{\text{tol}} = \pi/2$ gliding smooths the solution $\theta(z,t)$ as time progresses, leading ultimately to a director solution uniform throughout the domain. Note however that, in line with our remarks above, the large-time uniform solution obtained depends on which solution was tracked; compare the final states in Figures 4.5(a) and 4.6(a).

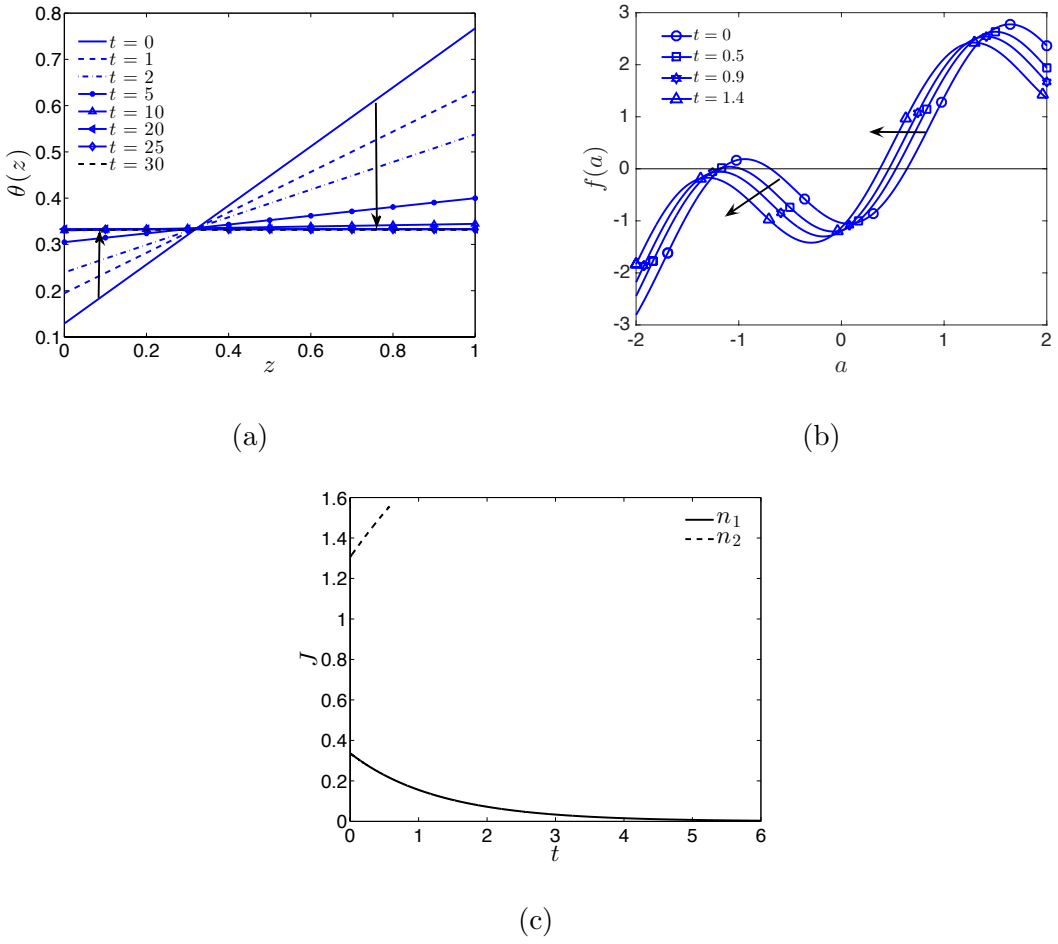


**Figure 4.5** (a) The evolution of director solution $\boldsymbol{n}_1$ under gliding Model I for $\alpha_0(0) = 0$, $\alpha_1(0) = \pi/3$ and $\alpha_{\text{tol}} = \pi/2$. (b) The evolution of $f(a)$ under gliding (same parameters) when tracking $\boldsymbol{n}_1$. Bistability is lost at $t \approx 0.6$. (c) The free energy $J(t)$ for $\boldsymbol{n}_1$ (solution tracked, solid curve) and $\boldsymbol{n}_2$ ("background" solution, dashed curve). The dashed curve stops where the background solution disappears.

As the steady states $\boldsymbol{n}_1$ and $\boldsymbol{n}_2$ evolve under gliding towards the uniform state, in either case, the system switches from bistable to monostable. To illustrate how bistability is lost, we show early time evolution of $f(a)$ in Figures 4.5(b) and 4.6(b).

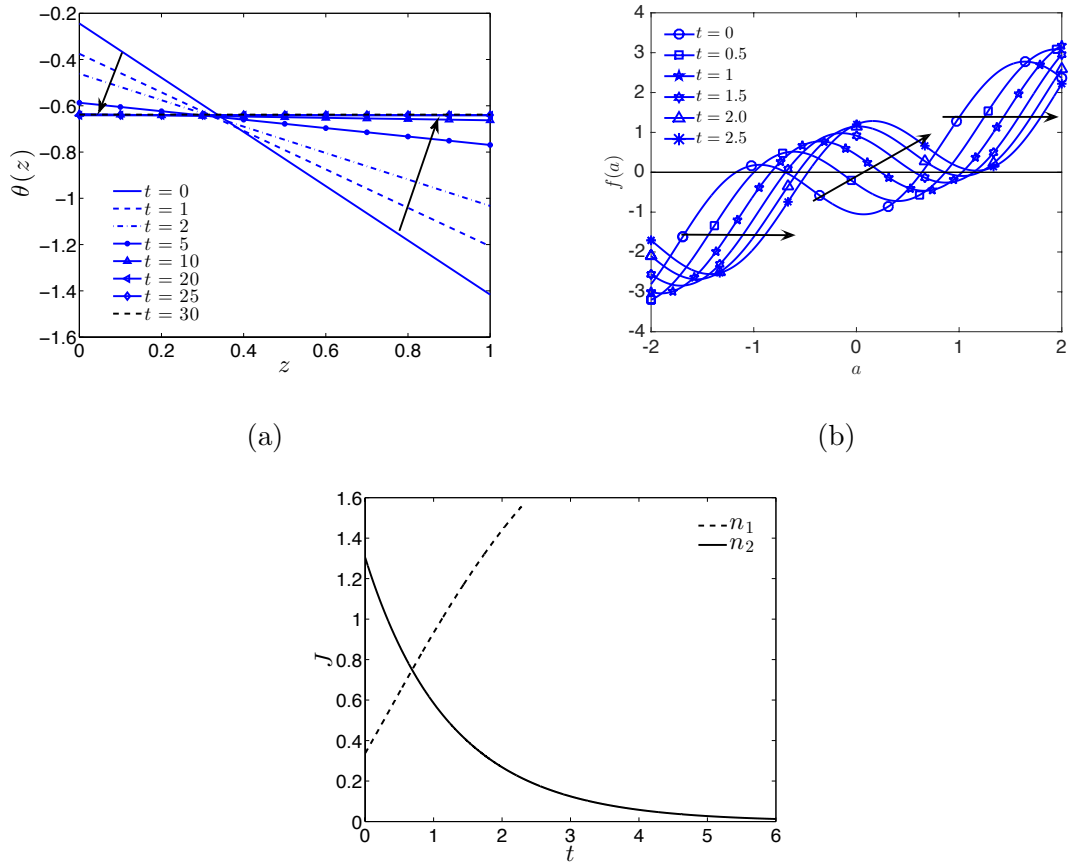


(a) (b)

(c)

**Figure 4.6** (a) The evolution of director solution $\boldsymbol{n}_2$ under gliding Model I for $\alpha_0(0) = 0$, $\alpha_1(0) = \pi/3$ and $\alpha_{\text{tol}} = \pi/2$. (b) The evolution of $f(a)$ under gliding (same parameters) when tracking $\boldsymbol{n}_2$. Bistability is lost at $t \approx 2.5$. (c) The free energy $J(t)$ for $\boldsymbol{n}_2$ (solution tracked, solid curve) and $\boldsymbol{n}_1$ ("background" solution, dashed curve). The dashed curve stops where the background solution disappears.

We see that in both cases, $f(a)$ evolves in a way that leads to the loss of two roots under gliding, leaving only a single root, corresponding to one stable steady state. Figure 4.5(b) shows that, while tracking $\boldsymbol{n}_1$, the root corresponding to $\boldsymbol{n}_1$ persists in time while the root corresponding to $\boldsymbol{n}_2$ disappears at $t \approx 0.6$ ($f(a)$ moves to the left and down). Similarly Figure 4.6(b) shows that, when tracking $\boldsymbol{n}_2$, the root corresponding to $\boldsymbol{n}_2$ persists in time while the root corresponding to $\boldsymbol{n}_1$ disappears at $t \approx 2.5$ ($f(a)$ moves to the right and up). These figures also illustrate that the

time at which bistability is destroyed, $t_b$, depends on which state we are tracking, $\boldsymbol{n}_1$ or $\boldsymbol{n}_2$.

As the director solution $\boldsymbol{n}_1$ (or $\boldsymbol{n}_2$) is tracked under gliding, the director begins to relax and smooth towards a uniform state, as in Figure 4.5(a) (or Figure 4.6(a)). As this happens, the total energy associated with $\boldsymbol{n}_1$ (or $\boldsymbol{n}_2$) decreases. At the same time, however, the total energy associated with the other "background" stable state $\boldsymbol{n}_2$ (or $\boldsymbol{n}_1$) increases as shown in Figure 4.5(c) (or 4.6(c)). If, as is the case in Figures 4.5 and 4.6, gliding is not halted, the energy of that background state $\boldsymbol{n}_2$ (or $\boldsymbol{n}_1$) will ultimately increase to a stage where that solution is no longer a local minimum of the free energy (at which point that steady state ceases to exist, simultaneously with the loss of roots of $f(a)$).

In the particular case considered in Figures 4.5 and 4.6, bistability is destroyed faster when tracking $\boldsymbol{n}_1$. This seems to be a consequence of the higher bulk energy associated with the director solution for $\boldsymbol{n}_2$. This solution $\boldsymbol{n}_2$ represents a shallower local minimum of the free energy for this parameter set, so that it is destroyed sooner under gliding. Figures 4.5(c) and 4.6(c) show the total free energies (given by $J = J^* h^*/K^*$; see Equation (2.4)) of both the solution being tracked (solid line) and the "background" solution (dashed line): we see that in both cases the solution being tracked decreases its total free energy under gliding, while the energy of the background solution increases. In these unlimited gliding examples, the dashed line stops abruptly in both cases, corresponding to the loss of the background solution (its free energy at that point ceases to be a local minimum in the energy landscape and the solution disappears). Note that it is never the solution being tracked that disappears under gliding but always the other solution, resulting in a continuous evolution of $a$. The tracked solution always decreases its total free energy, becoming more stable with time, while the reverse applies to the background solution. Gliding Model II leads to similar results: although the time at which bistability is destroyed varies

slightly from gliding Model I, it too ultimately destroys bistability provided that $\alpha_{\text{tol}}$ is sufficiently large, as in Model I.

**4.3.3.2 Effect of Limited Gliding in Model I.** To determine how limited gliding, using Model I, affects the structure of an initially bistable system in time, we solve Equations (4.5)–(4.8) for a range of values of $\alpha_{\text{tol}}$. Figure 4.7 shows the times, $t_b$, at which bistability is destroyed, for different values of $\alpha_{\text{tol}}$ and $\Delta\alpha(0)$. Both steady states $\boldsymbol{n}_1$ and $\boldsymbol{n}_2$ are considered separately. We first discuss the general properties of the behavior of the gliding system, and then discuss the specific properties of each steady state separately. We observe that if $\alpha_{\text{tol}}$ is small, then gliding lasts for a short

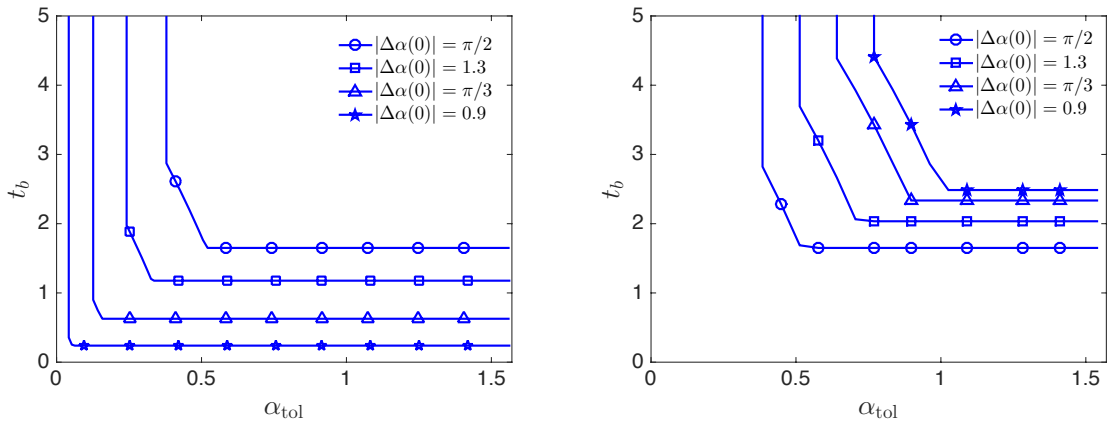


(a) (b)

**Figure 4.7** The time, $t_b$, at which bistability of a system is destroyed, vs $\alpha_{\text{tol}}$ given a steady state $\boldsymbol{n}_1$ or $\boldsymbol{n}_2$ and various $\Delta\alpha(0) = \alpha_1(0) - \alpha_0(0)$ with $\alpha_0(0) = 0$. Gliding Model I is used here.

time only, and the system will retain its bistability independently of which solution we track, while if $\alpha_{\text{tol}}$ is sufficiently large, then the system will glide until bistability is destroyed. Figure 4.7 shows four different bistable cases, characterized by different values of $\Delta\alpha(0)$ and, while results are quantitatively different between these four cases, three common key features are observed. First, if $\alpha_{\text{tol}}$ is sufficiently small, then gliding always stops before bistability is destroyed, hence $t_b = \infty$. Second, if $\alpha_{\text{tol}}$ is

sufficiently large, then bistability will be lost before either anchoring angle has glided through the tolerance value; therefore in such situations $t_b$ is independent of $\alpha_{\text{tol}}$ (the horizontal portions of the graphs). Third, the horizontal and vertical portions of the graphs are connected by intermediate sloped portions. These relate to situations where, depending on the value of $\alpha_{\text{tol}}$ and the initial anchoring conditions, gliding may stop first at one boundary but continue at the other, leading to ultimate loss of bistability.

The transitions between the different portions of the $(\alpha_{\text{tol}}, t_b)$ graphs depend on which solution is considered ($\boldsymbol{n}_1$ or $\boldsymbol{n}_2$), and on the initial state, characterized by $\Delta\alpha(0)$. Due to the special symmetry of the case $\Delta\alpha(0) = \pi/2$, where $\boldsymbol{n}_1$ and $\boldsymbol{n}_2$ are simple mirror images, these two curves are the same in Figures 4.7(a), 4.7(b). However, for other values of $\Delta\alpha(0)$, the two corresponding steady states, $\boldsymbol{n}_1$ and $\boldsymbol{n}_2$, give rise to different behavior. We find that, in line with our observations about energetics in the unlimited gliding case at the end of Section 4.3.3.1, in general when tracking $\boldsymbol{n}_2$ we require larger values of $\alpha_{\text{tol}}$ to destroy bistability (compare Figures 4.5 and 4.6: the solution $\boldsymbol{n}_1$ is associated with a relatively deep free energy minimum and takes longer to eliminate under gliding). Therefore, when tracking solution $\boldsymbol{n}_2$, gliding must proceed for a longer time in order to eliminate the stable steady state $\boldsymbol{n}_1$ and destroy bistability, hence higher values of $\alpha_{\text{tol}}$ are required for this to happen.

Since the number of steady states (at any given time) in an initially bistable system depends on both $\alpha_{\text{tol}}$ and the difference in initial anchoring angles $\Delta\alpha(0)$, we now further investigate how $\Delta\alpha(0)$ influences bistability under gliding. We define $\alpha_{\text{tol}}^{\text{min}}$ to be the smallest value of $\alpha_{\text{tol}}$ that leads to loss of bistability under gliding, for each value of $\Delta\alpha(0)$. Figure 4.8 plots $\alpha_{\text{tol}}^{\text{min}}$ versus $\Delta\alpha(0)$ for both initial steady states $\boldsymbol{n}_1$ and $\boldsymbol{n}_2$. We observe that $\alpha_{\text{tol}}^{\text{min}}$ increases (very nearly linearly) with $\Delta\alpha(0)$ for $\boldsymbol{n}_1$, but decreases (again almost linearly) with $\Delta\alpha(0)$ for $\boldsymbol{n}_2$. The two curves in

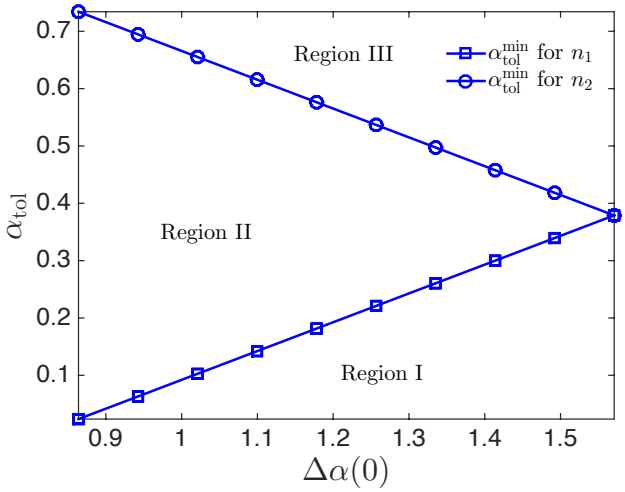


**Figure 4.8** $\alpha_{\text{tol}}^{\min}$ (representing the smallest value of $\alpha_{\text{tol}}$ that leads to loss of bistability under gliding) plotted as a function of $\Delta\alpha(0)$ for each steady state ($\boldsymbol{n}_1$ ($\square$) and $\boldsymbol{n}_2$ ($\circ$)). These plots identify three regions in $(\alpha_{\text{tol}}, \Delta\alpha(0))$ parameter space with initial steady states $\boldsymbol{n}_1$ and $\boldsymbol{n}_2$: Region I: bistability is not destroyed regardless of which steady state is tracked; Region II: bistability is lost when tracking $\boldsymbol{n}_1$ but not for $\boldsymbol{n}_2$; and Region III: bistability is lost independently of which steady state we start from.

Figure 4.8 meet where $\Delta\alpha(0) = \pi/2$: this is again due to the mirror-image symmetry of $\boldsymbol{n}_1$ and $\boldsymbol{n}_2$ in this situation (with $\alpha_0(0) = 0$).

We can use these results to identify regions in $(\Delta\alpha(0), \alpha_{\text{tol}})$ space where the system retains its bistability, depending on which director solution is tracked. With the chosen values of anchoring strengths and $\alpha_0(0) = 0$, we distinguish three such regions in Figure 4.8: Region I, in which bistability is never destroyed regardless of which steady state is tracked; Region II, in which bistability is lost when tracking $\boldsymbol{n}_1$ but not when tracking $\boldsymbol{n}_2$; and Region III, in which bistability is lost regardless of whether $\boldsymbol{n}_1$ or $\boldsymbol{n}_2$ is tracked.

#### 4.3.3.3 Effect of Limited Gliding in Model II.

We now briefly outline results analogous to those of Subsection 4.3.3.2 for gliding Model II, Equations (4.5)–(4.7) and Equation (4.9). Figure 4.9 (analogous to Figure 4.7) shows time $t_b$ at which bistability is destroyed, as a function of $\alpha_{\text{tol}}$. The behavior is qualitatively similar

to that of Model I, but smoothed. In the regions to the left of the nearly vertical portion of the curves, $\alpha_{\text{tol}}$ is sufficiently small that bistability is never destroyed. When tracking $\boldsymbol{n}_2$ under gliding, larger values of $\alpha_{\text{tol}}$ are needed to destroy bistability than when tracking $\boldsymbol{n}_1$ (see also Figures 4.5 and 4.6). Also, for sufficiently large (but fixed) $\alpha_{\text{tol}}$, $t_b$ decreases with $\Delta\alpha(0)$ for $\boldsymbol{n}_1$ and increases as $\Delta\alpha(0)$ decreases for $\boldsymbol{n}_2$. Again the results for the symmetric case $\Delta\alpha(0) = \pi/2$, in which $\boldsymbol{n}_1$ and $\boldsymbol{n}_2$ are mirror-images, are identical in Figures 4.9(a) and 4.9(b), as anticipated.

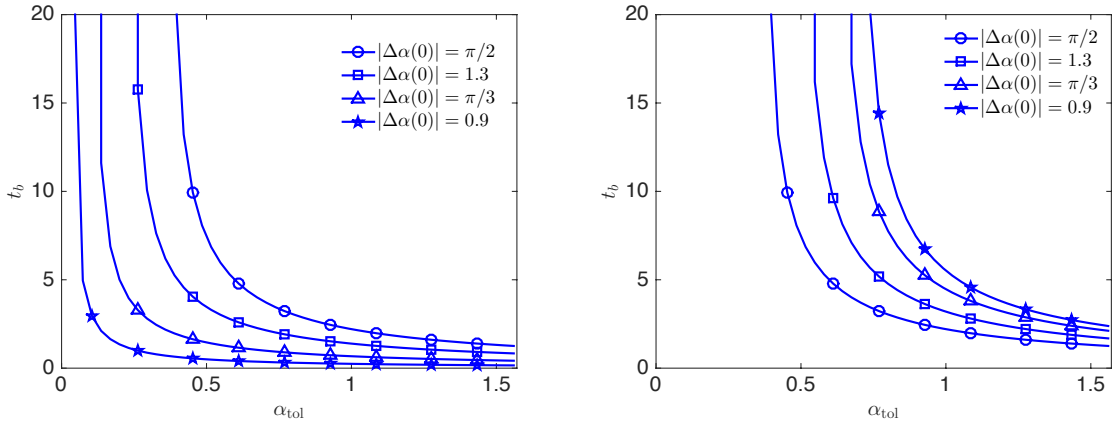


(a) (b)

**Figure 4.9** The time at which bistability of a system is destroyed, $t_b$ vs $\alpha_{\text{tol}}$ given a steady state $\boldsymbol{n}_1$ or $\boldsymbol{n}_2$ and various $\Delta\alpha(0)$ using gliding Model II. Compare with Figure 4.7 for Model I.

Unsurprisingly, Models I and II generate quantitatively different results. Comparing the plots of $t_b$ for $\boldsymbol{n}_1$ in both models (see Figures 4.7(a) and 4.9(a)), we observe that when $\alpha_{\text{tol}}$ is small, $t_b$ is larger for Model II, with the reverse trend for large $\alpha_{\text{tol}}$. Similarly, when tracking $\boldsymbol{n}_2$ in Model II (see Figure 4.9(b)), bistability is destroyed faster for large values of $\alpha_{\text{tol}}$ and slower for small values of $\alpha_{\text{tol}}$ (see Figure 4.7(b)).

### 4.3.4 Effect of Switching and Unlimited Gliding in a Bistable System

Switching between the two stable steady states in an initially bistable system is possible in the absence of gliding [13, 15]: with the application of a suitable transient electric field, one can achieve two way switching in the appropriate parameter regimes. Motivated by the relevance of switching in devices that are both flexible and bistable, and by our results in Section 4.3.3, we now examine a bistable system in which both unlimited gliding ($\alpha_{\text{tol}} = \pi/2$) and switching act sequentially, and we investigate the effect that such switching has on the system dynamics.

As an illustrative example, we consider an initially bistable system with anchoring conditions $\alpha_0(0) = 0$, $\alpha_1(0) = \pi/3$. As noted above, in practice two way switching would be obtained through transient application of an electric field; however in the present work, we simply impose the switch between states at specified times: we switch the system instantaneously from one stable state to the other by selecting the alternative (stable) root of Equation (4.11) at the chosen switching time to obtain the new director solution (in any practical application, switching would occur on a timescale much faster than gliding, so from the point of view of the gliding dynamics this instantaneous switch is reasonable). Gliding is then continued, but now with the new steady state. For the example, illustrated in Figure 4.10, we initially track $\boldsymbol{n}_2$, and then impose a series of switches at chosen switching times $t = 1, 2, 3, 4$, etc. Note that the initial steady state influences only the details of the results that follow; similar results are obtained if we initially track $\boldsymbol{n}_1$.

Figure 4.10(a) shows the evolution of the director field over four successive switches. Figure 4.10(b) shows the evolution over many more successive switches, via the plot of the root, $a(t)$, of Equation (4.11) that corresponds to the director solution being tracked under gliding; and via the corresponding total free energy $J(t) = J^*h^*/K^*$ (see Equation (2.4)) of that solution. We observe that, in contrast to the case of unlimited gliding without switching, bistability is not destroyed, even

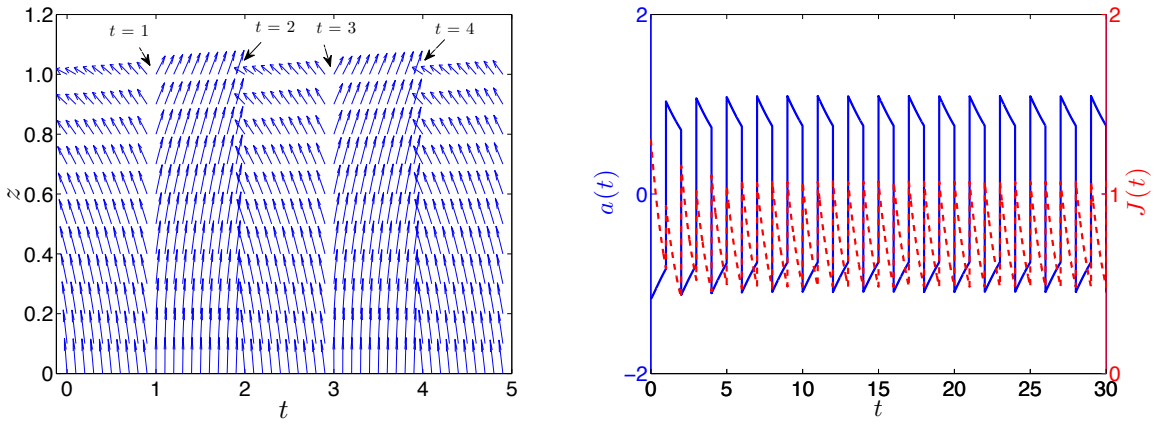


(a) (b)

**Figure 4.10** (a) Switching from $\boldsymbol{n}_2 \to \boldsymbol{n}_1 \to \boldsymbol{n}_2 \to \boldsymbol{n}_1 \to \boldsymbol{n}_2$ for $\alpha_0(0) = 0$, $\alpha_1(0) = \pi/3$ using gliding Model I. (b) Switching and gliding dynamics for the same system over long times, monitored by plotting the selected root $a$ (solid curve) of Equation (4.10) and the free energy $J$ (dashed curve) of the corresponding solution.

though gliding occurs continuously throughout. If switching had not been imposed, then bistability would have been lost at $t_b \approx 2.3$, see Figure 4.7.

Figure 4.10(b) shows that, except at switching events, where energy is put into the system to make the switch, $|a(t)|$ (the total director bending angle across the layer) and $J(t)$ (the system free energy) are always decreasing under gliding, no matter which state we track. The director is always relaxing towards a uniform state between switches, lowering its energy as it does so. However, recalling the results of Figures 4.5 and 4.6, we know that as this happens, the "background" solution is simultaneously increasing its free energy.

Consider the behavior of $|a(t)|$ and $J(t)$ at the switching times $t = 1, 2, 3, 4, ..., n$. At each switching time, both $|a(t)|$ and $J(t)$ jump (the states before and after the switch have different energies). Consider, for example, the switch from $\boldsymbol{n}_2 \to \boldsymbol{n}_1$ at $t = 2$. Here, $|a(2^+)| > |a(2^-)|$ (the $\pm$ superscripts denote right- and left-handed limits, respectively), and $J(2^+) > J(2^-)$, indicating that (i) the solution after switching ($\boldsymbol{n}_2$ here) has a greater elastic bend across the layer than the solution before the switch

($\boldsymbol{n}_1$), and that (ii) energy input is required to effect the switch (which in practice would most likely come from transient application of an electric field). Figure 4.10(b) reveals that, though the initial behavior of the system is irregular, after many regularly-spaced switches both $J(t)$ and $|a(t)|$ fall into a periodic behavior. This implies that regular switching can sustain bistability indefinitely: while gliding acts to dissipate elastic energy from the bulk, the act of switching puts new energy into the system. Providing that switching takes place sufficiently often, the bulk elastic energy can be maintained at a high enough level to retain the bistability. Another way to view this periodic behavior is that the regular switching reverses the effect of the gliding. Consider times $t = n$ sufficiently large that we are in the periodic regime. Immediately after a switch (to solution $\boldsymbol{n}_1|_{t=n^+}$, say) this solution begins to glide, evolving eventually to $\boldsymbol{n}_1|_{t=(n+1)^-}$. We can undo this gliding exactly, if we now switch to solution $\boldsymbol{n}_2|_{t=(n+1)^+}$, allow it to glide for one time unit to $\boldsymbol{n}_2|_{t=(n+2)^-}$, and then switch to $\boldsymbol{n}_1|_{t=(n+2)^+} \equiv \boldsymbol{n}_1|_{t=n^+}$.

The example shown in Figure 4.10 raises an interesting question: Since switching reverses the gliding effect in a bistable system, and we know that indefinite gliding with no switching leads inevitably to loss of bistability, how often must we switch to retain bistability? To answer this question (at least for our specific example), we modify the previous procedure: instead of switching between steady states at the chosen fixed times, we now let the system glide until it is about to lose bistability, then switch, ensuring that switching occurs at $t_{lb}$, which we define as the last time for which the system is bistable. Figure 4.11 shows an example of this procedure, applied repetitively. Figure 4.11(a) shows the director field and Figure 4.11(b) plots $a(t)$ and $J(t)$ as switching between the states occurs. As above, bistability can be maintained indefinitely with this approach. In addition, with this switching strategy we observe that $|a(t)|$ and $J(t)$ both fall into a periodic behavior immediately after the first switch occurs.

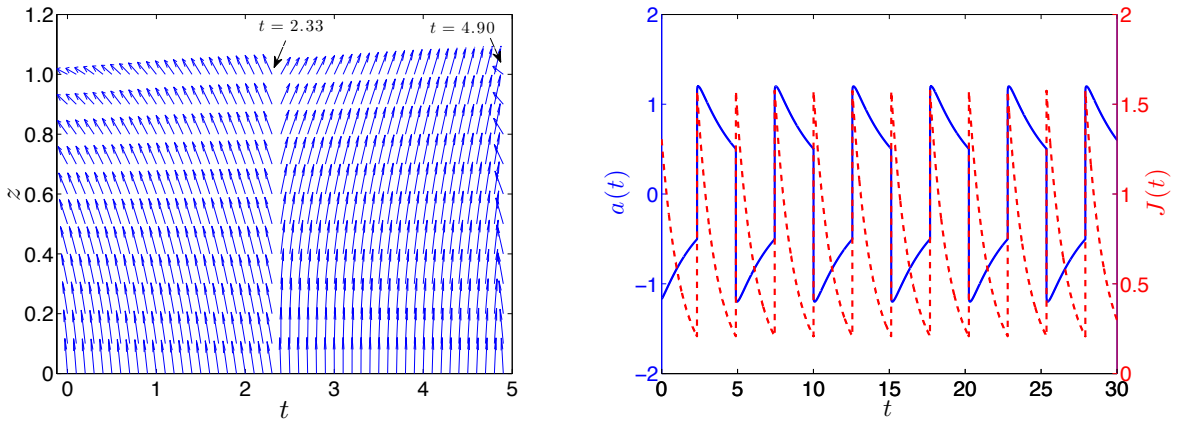


(a) (b)

**Figure 4.11** (a) Switching from $\boldsymbol{n}_2 \to \boldsymbol{n}_1 \to \boldsymbol{n}_2 \to \boldsymbol{n}_1$ for $\alpha_0(0) = 0$ and $\alpha_1(0) = \pi/3$ using gliding Model I, with all switches imposed when the system is about to lose bistability. (b) Switching and gliding dynamics for the same system over long times, monitored by plotting the selected root $a$ (solid curve) of Equation (4.10) and the free energy $J$ (dashed curve) of the corresponding solution.

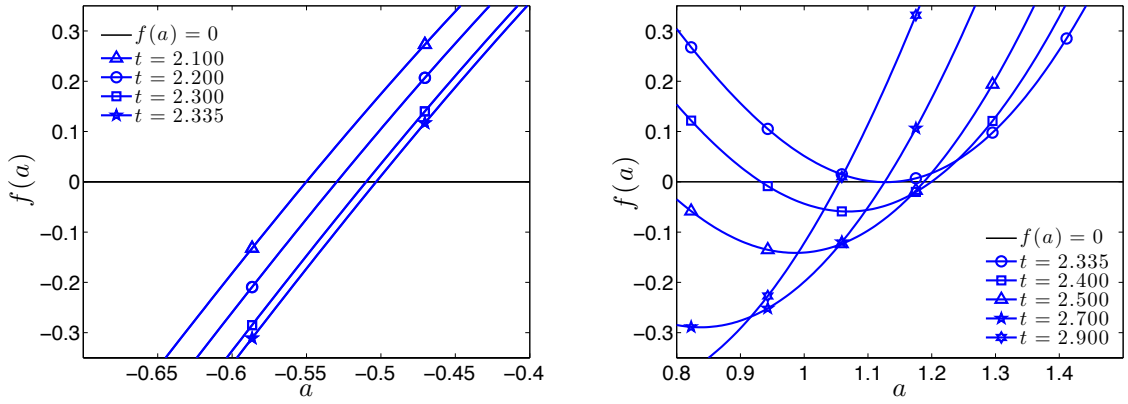


(a) (b)

**Figure 4.12** Evolution of $f(a)$, Equation (4.11), close to the root and the switching time $t = 1.650$ from $\boldsymbol{n}_2 \to \boldsymbol{n}_1$ when $\alpha_0 = 0$, $\alpha_1(0) = \pi/34$. The switch takes place just before bistability would have been lost, as may be seen in (b).

It is curious that this particular switching strategy changes the dynamics of the director solution immediately after the switch. For $t = t_{lb}^{+}$, $|a(t)|$ starts to *increase* briefly, before the anticipated decrease under gliding. This behavior is reflected both in the plot of the director in Figure 4.11(a), and in the plot of $a(t)$ in Figure 4.11(b).

Plotting the evolution of $f(a)$ before and after the first switching time $t_{lb} = 2.335$ (shown in Figure 4.12), we observe that when tracking the initial solution $\boldsymbol{n}_2$, $f(a)$ (and the corresponding root) moves to the right (see Figure 4.12(a)) while after switching to $\boldsymbol{n}_1$, $f(a)$ moves to the left and down (see Figure 4.12(b)). A transition phase occurs at $t = 2.335^+$ immediately following the switch where the root $|a(t)|$ continues to increase despite the change in evolution of $f(a)$ at the switch time (see profiles of $f(a)$ at $t = 2.335$ and $t = 2.400$ in Figure 4.12(b)). Note however that, though this non-monotone behavior of $a(t)$ under gliding immediately following switching is curious, the total energy following the switch immediately begins to decrease in time under the gliding, as anticipated.

Another interesting question to ask is how the energy lost due to gliding (compensated by the energy input in switching) depends on the switching interval, and whether there is an "optimum" switching strategy minimizing total energy expenditure. To answer this question, we consider a general periodic switching strategy, and compute the total energy lost due to gliding, $\Delta J_{n+1} = J(t)|_{t_n^+} - J(t)|_{t_{n+1}^-}$, for different switching intervals $\Delta t = t_{n+1}^- - t_n^+$. Table 4.1 shows the total energy expenditure, $S_{\Delta J}$, for the period $t = 20$ to $t = 100$, during which the system has settled into a periodic behavior. We observe that, at least for the case considered here, the total energy input needed to maintain bistability decreases as the time interval at which switching is applied increases (even though more energy is lost during each gliding cycle as its length increases). We conjecture that the most energy-efficient approach to maintaining the bistability is to switch as late as possible.

Although in this section we have used specific examples to illustrate our results, we believe that certain conclusions apply quite generally. To summarize: (i) If an initially bistable system undergoes unlimited gliding, and no switching between states occurs, then loss of bistability is inevitable (the system will approach a uniform director solution); (ii) if switching between the states is imposed sufficiently

**Table 4.1** Total Energy Input as a Result of Switching Measured from $t = 20$ until $t = 100$

| Switching Interval | Total Energy Input $S_{\Delta J}$ |
|---|---|
| $t = 0.5$ | 47.34 |
| $t = 1.0$ | 46.79 |
| $t = 1.5$ | 44.71 |
| $t = 2.0$ | 44.58 |
| $t = 2.3$ | 42.67 |
| $t = t_{lb}$ | 42.39 |

often (specifically, one must always switch to the "background" solution before it disappears) then bistability can be retained indefinitely; (iii) if the switching is imposed periodically then the whole system will approach a periodic state at large times; and (iv) if we always wait the maximum time before switching (waiting until the background state is about to disappear) then the periodic behavior is attained immediately (possibly with some anomalous behavior in $a(t)$).

Finally, we remark that these examples and observations represent a worst-case scenario in which gliding is unlimited, so that loss of bistability is inevitable with no switching. Introduction of limited gliding $\alpha_{\text{tol}} < \pi/2$ will only improve matters since, as we already know, if $\alpha_{\text{tol}}$ is sufficiently small then bistability can be retained indefinitely even with no switching.

## 4.4 Conclusions

We present two Models (I and II) that describe the evolution of the director field within a confined layer of nematic liquid crystal, bounded by two infinite polymeric plates, at each of which anchoring is weak. At these plates, director gliding may occur:

the anchoring angle or easy axis undergoes a continuous realignment under the torque due to the bulk elasticity of the nematic layer. In Model I, gliding occurs at a rate proportional to the difference between the anchoring angle and the director angle at the interface considered, but stops abruptly once the deviation of the anchoring angle from its initial value reaches some tolerance value, $\alpha_{\text{tol}}$ (abrupt cessation). In Model II, gliding is halted smoothly as $\alpha_{\text{tol}}$ is approached (smooth cessation). Both models exploit the separation in timescales between gliding (long timescale) and elastic response (short timescale) to justify a quasistatic approximation for the director field orientation within the layer, with the model dynamics driven purely by the gliding. We investigate in detail how director gliding, governed by each model, affects the evolution of the director field, as $\alpha_{\text{tol}}$, and the initial anchoring angles, vary. For large $\alpha_{\text{tol}}$, gliding leads to a director solution that is uniform throughout the domain, for both gliding models.

We pay particular attention to the behavior under gliding of an initially bistable system. For large values of $\alpha_{\text{tol}}$, gliding destroys bistability independently of the model chosen. However, the time at which bistability is destroyed is model dependent. Furthermore, we investigate how switching between stable steady states, in the presence of gliding, can affect the number of available steady states at a given time. We conclude that switching can retain bistability, even under unlimited gliding, as long as it occurs sufficiently often. Furthermore, we find that if retention of bistability is the sole aim, then it is advantageous to switch as late as possible (just before the system is about to lose bistability): such a strategy minimizes the energy lost due to gliding.

# CHAPTER 5

# ELECTRIC FIELD INDUCED GLIDING IN A NEMATIC LIQUID CRYSTAL LAYER: COMPARISON WITH EXPERIMENTAL DATA

## 5.1 Introduction

Chapter 4 focused on the phenomenon of director gliding in NLC layers that consist of different anchoring orientations at each boundary. In this chapter, we expand the investigation to include a study that focuses on director gliding in the presence of an electric field. Multiple experiments have observed both azimuthal and zenithal gliding [26–28, 38, 39, 42, 43] in nematic liquid crystals. In this chapter, we focus on the experiments carried out by Joly *et al.* [28] and Buluy *et al.* [9] which present experimental evidence for zenithal gliding.

The experiment in [28] consists of a NLC layer (5CB) confined between two substrates with different anchoring properties: the lower substrate is spin-coated with polyimide Nissan SE 3510 and treated mechanically to give weak, nearly planar anchoring, while the upper substrate is treated to obtain strong planar anchoring (see [28] for details). An electric field is applied perpendicular to the layer for 140 hours, during which time the zenithal anchoring angle at the lower substrate is observed to increase by 2.2° (the strong anchoring at the upper substrate is unaffected). The electric field is then permanently shut off and the system starts to relax back to its initial state. After 13 days, the authors observe that the easy axis has glided back almost to its initial position. This behavior is schematized in Figure 5.1.

The experiment in [9] provides evidence of both azimuthal and zenithal gliding. We focus on the zenithal gliding, which was observed in the following setup, very similar to that of [28]; a layer of 5CB was confined between two parallel bounding surfaces, one coated with a polymer (PVCN-F) at which gliding occurs; the other treated to obtain strong planar anchoring. Anchoring at the polymer-coated surface

is weak and very nearly planar, with a pretilt angle of just 0.8°. An electric field is applied perpendicular to the PVCN-F surface for 16 hours, followed by an electric field shut off. Zenithal gliding is observed in the PVCN-F coated layer after the electric field is removed (see the schematic in Figure 5.2).

Both investigations present simple models that they use to obtain the best fit to each experiment. In Ref. [28], the authors argue that the director angle at the gliding substrate can be fitted by a sum of no fewer than three exponential terms, with the three exponents determined independently for field *on* and *off* cases (six exponents total). Buluy *et al.* [9] present a similar model but consisting of two exponential terms, chosen specifically to best fit the experimental data. In this chapter, we develop a mathematical model that aims to capture the mechanics of the interaction between NLC molecules and the adjacent polymer coated boundary, and that fits the gliding data observed in both sets of experiments. This investigation is structured as follows: in Section 5.2, we supplement the mathematical model that governs the evolution of the director field (presented in Chapter 2) with a gliding model that captures the slow reorientation of the easy axis. Section 5.3 summarizes the experimental data observed in [9] and [28] respectively and discusses how our results compare with the observed gliding data. Section 5.4 discusses the conclusions.

## 5.2 Mathematical Model

As in the previous chapters, we rely on the mathematical model developed in Chapter 2 to describe the evolution of the director field in a NLC layer bounded by two parallel plates where a uniform electric field can be applied. We supplement these equations with a gliding model (in the form of an ordinary differential equation) that aims to capture the gliding behavior observed in [9] and [28]. Before we dive into the details of our gliding model, we briefly schematize the key features of the two experimental systems.

Figure 5.1 summarizes the gliding evolution observed by Joly *et al.* [28]. Under prolonged application of an applied field (140 hours) and with an initial preferred anchoring angle of 6.7° at the gliding surface, these authors tracked the evolution of the easy axis, observing that it reaches a plateau value of 8.9°. After the electric field is turned off, the easy axis is tracked again, and it is observed to glide back almost to its initial position, but not quite. The experimental data show that the easy axis glides back to a value of approximately 7.3° after 13 days (0.6° higher than its initial preferred position), indicating that gliding is only partially reversible.

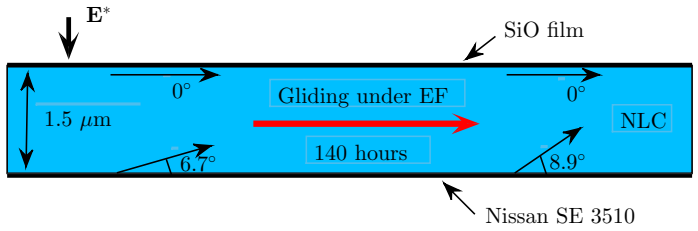


(a)

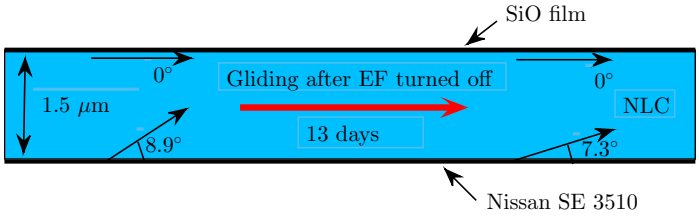


(b)

**Figure 5.1** Schematic summarizing the drift of the easy axis (gliding) in [28] (a) during the time of application of an electric field; and (b) after the electric field is turned off. Anchoring angles are not drawn to scale.

Similarly, Figure 5.2 schematizes the experimental procedure of Buluy *et al.* [9]. An electric field is applied continuously for 16 hours across a layer of NLC bounded by two parallel plates, only one of which experiences gliding. A preferred anchoring angle of 0.8° was measured before the electric field is applied; and at the time the field is removed, the anchoring angle has increased (via gliding) to 3.0°. After the electric field is removed, the authors track the relaxation of the easy axis back towards its initial position.

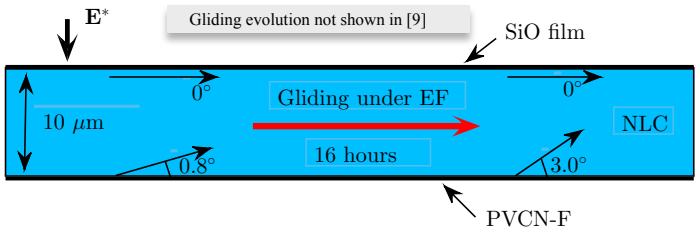


(a)

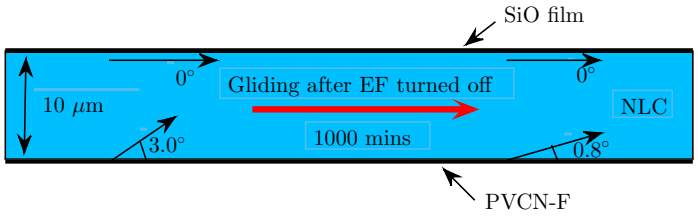


(b)

**Figure 5.2** Schematic summarizing the drift of the easy axis (gliding) in [9] (a) during the time of application of an electric field; and (b) after the electric field is turned off. Anchoring angles are not drawn to scale.

In order to fit our model results directly to the data of [9,28], we introduce two important notational changes in this chapter: both anchoring angles $\alpha$ and director angle $\theta$ are here measured from the horizontal direction, as is indicated in Figures 5.1 and 5.2. This modifies the governing equations given by Equations (2.6) slightly; the new (dimensionless) versions are given in Equations (5.3)-(3.2c) below. Our model assumes that the gliding rate is proportional to the difference between the anchoring angle and the director angle at the gliding surface. In addition we assume, consistent with the data and with our model in Chapter 4, that gliding is not unlimited. Instead, we hypothesize that it persists until the anchoring angle has changed by a maximal amount, $\alpha_{\text{tol}}$, or until the director takes the same value as the anchoring angle at the gliding boundary: $\theta(0, t^*) = \alpha_0(t^*)$. Mathematically, our proposed model (which generalizes that of Chapter 4 takes the form of an ordinary differential equation for the anchoring angle, $\alpha_0(t^*)$, at the gliding boundary $z^* = 0$:

$$\frac{d\alpha_0}{dt^*} = \lambda_0^*[\alpha_0(t^*) - \theta(0,t^*)]\left(1 - \frac{|\alpha_0(t^*) - \alpha_0(0)|}{\alpha_{\text{tol}}}\right)^n, \tag{5.1}$$

where $\lambda_0^*$ is a relaxation rate of the anchoring angle at $z^* = 0$ and $n > 0$ is an exponent that we introduce to capture the nonlinear dynamics that are observed in the experiments. Since no gliding occurs at the boundary $z^* = h^*$, the anchoring angle $\alpha_{h^*}$ remains fixed. When $\alpha_{\text{tol}} = 0$, no gliding occurs while as $\alpha_{\text{tol}} \to \pi/2$, gliding is unlimited. The model of Chapter 4 is recovered by setting $n = 1$.

### 5.2.1 Scaling and Nondimensionalization

We nondimensionalize the modified versions of Equations (2.6) as follows:

$$z = \frac{z^*}{h^*}, \quad t = \lambda_0^* t^* \qquad \mathcal{A}_0 = \frac{h^* \mathcal{A}_0^*}{K^*}, \tag{5.2}$$

where $h^*$ is the thickness of the NLC layer which varies depending on the experimental setup. Note that time is scaled using the gliding timescale, $(\lambda_0^*)^{-1}$. This parameter will depend on system characteristics such as substrate material and treatment, and the NLC used. Due to the polar nature of the molecules in the polymeric coatings used in the experiments, $\lambda_0^*$ may also depend on the strength of the applied electric field. We believe that the applied field affects not only the orientation of the NLC molecules, but may also influence directly the orientation of the polymer molecules in the coating layer. (The material used to coat the gliding surface in [28] is the polyimide Nissan SE 3510, which has a small dielectric constant of approximately 3.0 [1].) Therefore, we use different values (based on the experimental data) for $\lambda_0^*$ in "field on" and "field off" cases.

After nondimensionalization, the modified versions of Equations (2.6) become:

$$\delta\theta_t = \theta_{zz} + \mathcal{D}\sin 2\theta, \tag{5.3}$$

$$\delta\tilde{\nu}\theta_t = \theta_z - \frac{\mathcal{A}_0}{2}\sin 2(\theta-\alpha_0) - \frac{\mathcal{F}}{2}\sin 2\theta \quad \text{on} \quad z=0, \tag{5.4}$$

$$-\delta\tilde{\nu}\theta_t = \theta_z + \frac{\mathcal{A}_1}{2}\sin 2(\theta-\alpha_1) - \frac{\mathcal{F}}{2}\sin 2\theta \quad \text{on} \quad z=1. \tag{5.5}$$

Here, as in Chapter 4, $\delta = ({h^*}^2\mu^*\lambda_0^*)/K^*$ represents the ratio between the timescales of the bulk elastic response of the NLC, given by ${h^*}^2\mu^*/K^*$ and the gliding response, $1/\lambda_0^*$. The parameters $\tilde{\nu}$, $\mathcal{D}$ and $\mathcal{F}$ are the dimensionless surface viscosity, dielectric and flexoelectric strengths respectively, as in Chapter 2. With the following parameter values: $h = 1.5$ $\mu$m in [28], $h = 10\mu$m in [9] ($K^*$, $\tilde{\mu}^*$, $\tilde{\nu}^*$ defined as in Chapters 3 and 4) and relaxation rates in the range of $0.15 - 20$ hr$^{-1}$ (based on the experimental data [9, 28]; see later), we observe that $\delta \ll 1$ and $\tilde{\nu} \ll 1$. Since we believe the anchoring strength at the upper (non-gliding) boundary is much stronger than the lower (gliding boundary) in both experiments, we assume strong anchoring at the upper boundary, leading to the following equations:

$$0 = \theta_{zz} + \mathcal{D}\sin 2\theta, \tag{5.6}$$

$$0 = \theta_z - \frac{\mathcal{A}_0}{2}\sin 2(\theta-\alpha_0) - \frac{\mathcal{F}}{2}\sin 2\theta \quad \text{on} \quad z=0, \tag{5.7}$$

$$\theta = \alpha_1 \quad \text{on} \quad z=1, \tag{5.8}$$

where the weak anchoring boundary condition at $z = 1$ is replaced by the Dirichlet condition (Equation (5.8)) appropriate in the limit $\delta \to 0$, $\mathcal{A}_1 \to \infty$. The dimensionless form of Equation (5.1) can be written as

$$\frac{d\alpha_0}{dt} = [\alpha_0(t) - \theta(0,t)]\left(1 - \frac{|\alpha_0(t) - \alpha_0(0)|}{\alpha_{\text{tol}}}\right)^n. \tag{5.9}$$

Equations (5.6)–(5.9) make up the complete model that describes the evolution of the easy axis within a NLC layer where gliding can occur at the lower

interface. Given the preferred anchoring conditions at both boundaries, we solve Equations (5.6)–(5.8) using the built-in MATLAB program BVP4c and obtain a solution for the director angle $\theta(z)$. We use this solution in Equation (5.9) to compute the anchoring angle $\alpha_0$ at the next time step, which is then used to obtain a new director solution using Equations (5.6)–(5.8) at the new time step. This process is repeated until $\theta(0,t) = \alpha_0(t)$ or until $|\alpha_0(t) - \alpha_0(0)| = \alpha_{\text{tol}}$, at which point gliding stops.

## 5.3 Analysis and Results

In this section, we first summarize briefly the experimental results presented in [9,28] and give a brief discussion of the models the authors use to describe the gliding process. Then, we present our numerical results from Equations (5.6)–(5.9) and make a direct comparison with the experimental data.

### 5.3.1 Overview of Experimental Results Presented in Ref. [28]

The experimental setup considered in [28] consists of a NLC layer bounded between two substrates treated such that only the lower substrate exhibits gliding with anchoring strong and planar at the upper boundary. The preferred anchoring orientation at the gliding boundary is $\alpha_0 = 6.7°$, measured from the horizontal axis (Figure 5.1). Joly *et al.* [28] state that anchoring is "strong" at this gliding boundary but do not provide precise values for anchoring strength, only a lower bound on anchoring extrapolation length at the boundary. In the absence of firm data, we take $\mathcal{A}_0 = 1000$ for the dimensionless anchoring strength at the gliding boundary, an order of magnitude larger than their lower bound on this quantity.

Based on the values reported in [8,17,28], we solve our model with the following parameter values: $h = 1.5$ $\mu$m, $\varepsilon_{\parallel} - \varepsilon_{\perp} \sim 5$ and $e_1^* + e_3^* \sim 5 \times 10^{-12}$C m$^{-1}$ for the dielectric and flexoelectric coefficients respectively, and obtain $\mathcal{F} = 31.21$ and $\mathcal{D} = 69$

when $E^* = 5V\mu\text{m}^{-1}$. Note that $\alpha_{\text{tol}}$ and $n$ cannot be estimated directly from [28] and they are chosen suitably to obtain the best fit to the data (Section 5.3.2).

Joly *et al.* [28] observe the easy axis to glide (zenithally) through an angle of 2.2° over the 150 hours during which the electric field is applied, increasing from its initial angle of 6.7° to 8.9°. On removal of the electric field, they observe that the easy axis direction glides back towards its initial position. After 13 days, its angle has decreased to 7.3°, 0.6° larger than its value before the electric field was first applied. The experimental data observed in [28] are produced using [3].

### 5.3.2 Comparison of Model Results with Data of [28]

We solve Equations (5.6)–(5.9) to obtain the evolution of the anchoring angle, $\alpha_0(t^*)$, at the gliding substrate, and the director angle, $\theta(0, t^*)$ there. As discussed in Section 5.3.1 above, the values of several model parameters have already been fixed. In order to obtain a good quantitative fit to the data in dimensional time, we investigate the model behavior as parameters $\alpha_{\text{tol}}$ and $n$ are varied. The remaining parameter, the relaxation rate $\lambda_0^*$, set to $\lambda_0^* = 0.15\ \text{hr}^{-1}$ when the electric field is turned on and $\lambda_0^* = 20\ \text{hr}^{-1}$ when the electric field is turned off, is obtained by fitting the early time behavior; the values of $\alpha_{\text{tol}}$ and $n$ mainly affect the intermediate-to-late time behavior.

To quantify how well our mathematical model predicts the gliding behavior in [28], we introduce a measure, $||\theta_{\text{exp}} - \theta_{\text{num}}||_2$, the $L_2$ norm of the difference of the experimental data and numerical results. The norm $||\theta_{\text{exp}} - \theta_{\text{num}}||_2$ is calculated for each value of $n$ and $\alpha_{\text{tol}}$ for both gliding scenarios: (a) when an electric field is turned on; and (b) after the electric field is turned off. In each scenario (plots of $||\theta_{\text{exp}} - \theta_{\text{num}}||_2$ vs. $\alpha_{\text{tol}}$ not shown here), we observe that for each value of $n$, there exists an optimal value of $\alpha_{\text{tol}}^{\text{opt}}$ that produces the best global fit i.e., the gliding curve with the lowest error.

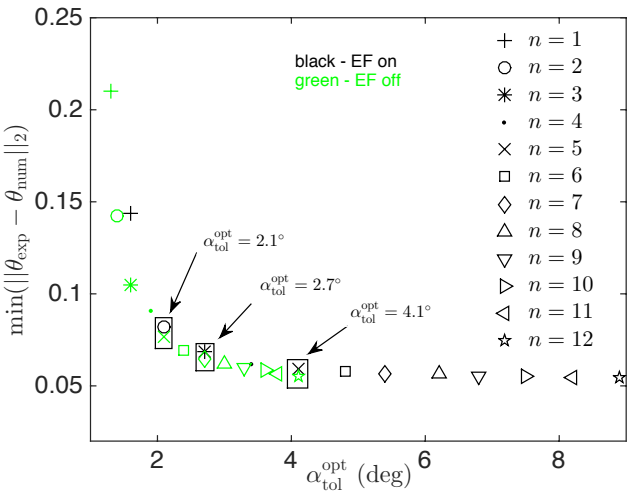


**Figure 5.3** Best global fit: $\min(||\theta_{\text{exp}} - \theta_{\text{num}}||_2)$ vs $\alpha_{\text{tol}}^{\text{opt}}$ for electric field *on* and electric field *off*. Each data point represents different $n$ values in each case.

Figure 5.3 presents the lowest norm $\min||\theta_{\text{exp}} - \theta_{\text{num}}||_2$ for each $n$ plotted against the optimal value, $\alpha_{\text{tol}}^{\text{opt}}$, when an electric field is applied (shown in black) and after the electric field is shut off (shown in green). We observe that the norm, $\min||\theta_{\text{exp}} - \theta_{\text{num}}||_2$ decreases as $n$ increases, for both electric field *on* and *off* cases, reaching a plateau value of 0.075 for $n > 6$. Hence, we can say that a highly nonlinear model (higher values of $n$ in Equation (5.9)) predicts better the gliding behavior in both electric field *on* and *off* scenarios.

We note that so far we have assumed that we vary two parameters independently, $\alpha_{\text{tol}}$ and $n$, to obtain a good quantitative fit to the experimental results shown in [28]. Taking a closer look at Figure 5.3 however, we observe that this is not necessary: there exist solutions to our gliding model with $\min||\theta_{\text{exp}} - \theta_{\text{num}}||_2 < 0.1$ in both electric field *on* and *off* gliding scenarios when $\alpha_{\text{tol}}^{\text{opt}} = 2.1°$, $\alpha_{\text{tol}}^{\text{opt}} = 2.7°$ and $\alpha_{\text{tol}}^{\text{opt}} = 4.1°$. Taking $\alpha_{\text{tol}} = 4.1°$ together with $n = 5$ (electric field *on*) and $n = 12$ (electric field *off*) leads to a gliding curve with error norm $\min||\theta_{\text{exp}} - \theta_{\text{num}}||_2 = 0.06$, for both electric field *on* and *off* cases. These values however imply a highly nonlinear gliding model (see Equation (5.9)). Note that one can lower the values of $n$ for both electric field *on* and *off* cases by choosing $\alpha_{\text{tol}} = 2.7°$ or $\alpha_{\text{tol}} = 2.1°$. In each case,

we obtain a global fit that is in good quantitative agreement with the experimental data, but now the norm is slightly higher for both electric field *on* and *off* cases with $||\theta_{\text{exp}} - \theta_{\text{num}}||_2 \approx 0.07$ for $\alpha_{\text{tol}} = 2.1^\circ$ and $||\theta_{\text{exp}} - \theta_{\text{num}}||_2 \approx 0.08$ for $\alpha_{\text{tol}} = 2.7^\circ$ respectively. If we wish to obtain a good fit while limiting the nonlinearity of the model (keeping $n$ small) we may choose $\alpha_{\text{tol}} = 2.1$ (with $n = 2$ for field *on* and $n = 5$ for field *off*) to describe the gliding behavior observed in [28] (See Figure 5.3).

We now expand our investigation to obtain the best gliding fit by fixing $n$ while varying $\alpha_{\text{tol}}$. Figure 5.4 presents the diagram illustrating the lowest norm $\min||\theta_{\text{exp}} - \theta_{\text{num}}||_2$ vs. $n$ for the two gliding scenarios depicted in [28]. We observe that in both cases, as the value of $n$ increases, the error measured by the norm $\min||\theta_{\text{exp}} - \theta_{\text{num}}||_2$ decreases, reaching a plateau value of less than 0.06 when $n = 12$. Here, we can obtain the best fit to the experimental data observed when $n = 12$ and $\alpha_{\text{tol}} = 8.9^\circ$ for the electric field *on* and $\alpha_{\text{tol}} = 4.1^\circ$ for the electric field *off* case (see Equation (5.9)). As in the previous case, one can consider lower values of $n$ at the expense of decreasing the accuracy of the numerical results. Indeed, taking $n = 2$ leads to the norm $||\theta_{\text{exp}} - \theta_{\text{num}}||_2 \approx 0.08$ and $||\theta_{\text{exp}} - \theta_{\text{num}}||_2 \approx 0.14$ for the electric field *on* (with $\alpha_{\text{tol}}^{\text{opt}} = 2.1^\circ$) and electric field *off* (with $\alpha_{\text{tol}}^{\text{opt}} = 1.4^\circ$) case, respectively.

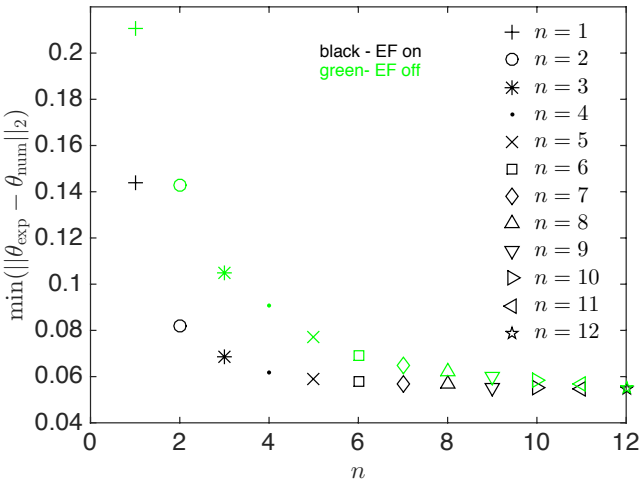


**Figure 5.4** Best global fit: $\min(||\theta_{\text{exp}} - \theta_{\text{num}}||_2)$ vs $n$ for electric field *on* and electric field *off*.

We now show explicitly how our model, with these parameter values, compares to the experimental data of [28]. Figure 5.5 shows the gliding evolution of $\theta(0, t^*)$ plotted on the same graph with the experimental gliding data obtained in [28] (a) when an electric field is turned on and (b) after the electric field is turned off. In the first case, we use $n = 12$ and $\alpha_{\text{tol}} = 8.9°$ while in the latter case, we use $n = 12$ and $\alpha_{\text{tol}} = 4.1°$; these parameters produce gliding curves with the lowest error $||\theta_{\text{exp}} - \theta_{\text{num}}||_2 < 0.06$. We observe that our results provide excellent fit to the gliding evolution shown in [28].

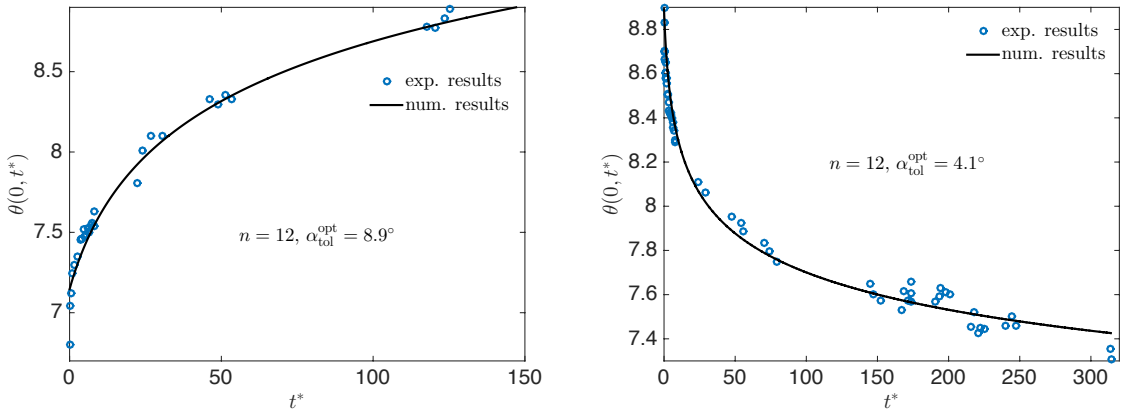


**Figure 5.5** Evolution of $\theta(0, t^*)$ and the experimental zenithal easy axis gliding in [28] for $n = 12$ when (a) an electric field is turned *on* and $\alpha_{\text{tol}}^{\text{opt}} = 8.9°$ and (b) after the electric field is turned *off* and $\alpha_{\text{tol}}^{\text{opt}} = 4.1°$.

### 5.3.3 Overview of Experimental Results Presented in Ref. [9]

Buluy *et al.* [9] consider a setup similar to that of [28], where a layer of 5CB is bounded between two parallel plates, 10 $\mu$m apart, treated such that only the lower substrate exhibits gliding. The initial preferred anchoring orientation is measured to be $\alpha_0 = 0.8°$ from the horizontal axis, with anchoring strength $\mathcal{A}_0^* \sim 0.25 \times 10^{-3} \text{Jm}^{-2}$, corresponding to $\mathcal{A}_0 = 312$ (Equation (5.2) with $h = 10$ $\mu$m). An electric field of magnitude $1\text{V}\mu\text{m}^{-1}$ is applied perpendicularly to the substrate for a period of 16 hours, during which gliding occurs. The field is then removed and the new easy axis

orientation is measured: 3.0°. The easy axis then begins to glide back towards its original orientation, and its evolution is tracked over a period of 1000 minutes. The experimental data are reproduced using [3].

### 5.3.4 Comparison of Model Results with Data of [9]

We compare the experimental results obtained in [9] under zenithal gliding with the numerical results obtained by solving Equation (5.6)–(5.9). We use the same technique as described at the end of Section 5.2.1 to obtain the gliding evolution of $\theta(0, t^*)$. Given the following parameters: $\mathcal{A}_0 = 312$, $\alpha_0 = 0.8°$, $\mathcal{F} = \mathcal{D} = 0$, we obtain good quantitative agreement with the experimental data provided that we choose the values of $\alpha_{\text{tol}}$ and $n$ that minimize the norm $||\theta_{\text{exp}} - \theta_{\text{num}}||_2$. As in [28], the relaxation rate $\lambda_0^*$ is obtained by fitting the early time behavior of the numerical results to the experimental ones and it is set to $\lambda_0^* = 3.7\ \text{min}^{-1}$.

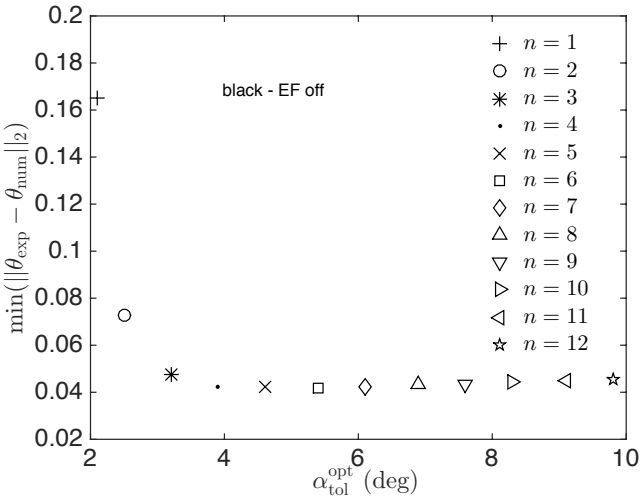


**Figure 5.6** Best global fit: $\min(||\theta_{\text{exp}} - \theta_{\text{num}}||_2)$ vs $\alpha_{\text{tol}}^{\text{opt}}$ for electric field *off*. Each data point represents different $n$ values (see legend).

Here, as in Section 5.3.2, we observe that for each value of $n$, there exists an optimal value of $\alpha_{\text{tol}}^{\text{opt}}$ that produces the best global fit to the experimental data, hence we plot the lowest norm $\min||\theta_{\text{exp}} - \theta_{\text{num}}||_2$ against the optimal value of $\alpha_{\text{tol}}^{\text{opt}}$ for each $n$. Figure 5.6 illustrates that as $n$ increases, the error between the numerical

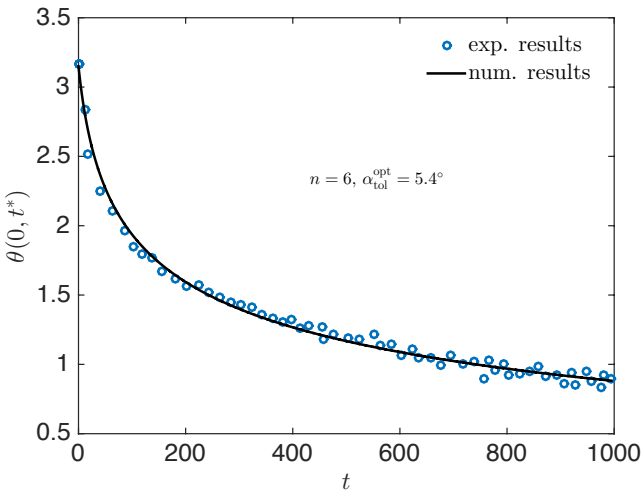


**Figure 5.7** Evolution of $\theta(0, t^*)$ and the experimental zenithal easy axis gliding in [9] after the electric field is turned *off* when $n = 6$ and $\alpha_{\text{tol}}^{\text{opt}} = 5.4°$.

results and experimental data decreases at first (when $n < 6$), reaching its lowest norm ($||\theta_{\text{exp}} - \theta_{\text{num}}||_2 < 0.05$) when $n = 6$ (and $\alpha_{\text{tol}} = 5.4°$), followed by a slow increase when $n > 6$. Due to the lack of data in the electric field *on* scenario in [9], we cannot compare gliding in the presence of an electric field. In this case then, we may conclude that the choice $n = 6$ and $\alpha_{\text{tol}} = 5.4°$ leads to the best global approximation of the results reported in Ref. [9]. As shown in Figure 5.7, we compare the gliding evolution of $\theta(0, t^*)$ after an electric field is turned off ($n = 6$ and $\alpha_{\text{tol}} = 5.4°$) with the gliding data shown in [9] and observe that these parameters lead to a good global fit to the experimental data, with an error norm $||\theta_{\text{exp}} - \theta_{\text{num}}||_2 \approx 0.04$.

## 5.4 Conclusions

We present a mathematical model that describes the evolution of the director field within a NLC layer bounded between two parallel plates where an electric field is applied perpendicularly to the plates and zenithal gliding occurs only at one boundary. We investigate in detail the long term evolution of the easy axis on the gliding surface when the layer is subjected to an electric field and after the electric field

is turned off. Our gliding model assumes that the anchoring angle, $\alpha_0$, reorients at a rate that is proportional to the difference between the anchoring angle and the surface director at the gliding surface. Gliding persists until the anchoring angle has changed by a maximal amount, $\alpha_{\text{tol}}$, or until the director takes the same value as the preferred anchoring angle at the boundary. We take advantage of the separation of the time scales between gliding and the elastic response, and assume a quasistatic model (using Ericksen-Leslie continuum theory for nematics) to describe the evolution of the director field within the layer. We investigate in detail how the easy axis evolves in time under the gliding model described by Equation (5.9) and compare our numerical results with the experimental data observed in Ref. [9, 28].

Both [9] and [28] consider a NLC layer bounded between two parallel plates, such that one substrate is treated to have a preferred anchoring orientation (0.8° in [9] and 6.7° in [28]) while the upper substrate is treated to obtain strong planar anchoring. An electric field is applied parallel to the $z$ direction for a set amount of time (16 hours in [9] and 140 hours in [28]). During the electric field *on* part of the experiment, Ref. [28] reports zenithal gliding reorientation of 2.2° while Ref. [9] does not provide any information on the gliding evolution of the easy axis. The electric field is then permanently shut off and both experiments measure the reorientation of the easy axis: both experiments observe the easy axis reorientation back almost to its initial position.

Each experiment uses an exponential function comprised of multiple exponentials to find the best fitting curve to the observed data. In this chapter, we use the experimental evidence provided in [9] and [28] and compare the numerical results obtained by solving Equations (5.6)–(5.9). We observe that given the appropriate parameter values $\mathcal{A}_0, \alpha_0, \lambda_0^*, \mathcal{F}, \mathcal{D}$ for each experiment, our gliding model predicts the gliding data observed in [9, 28] extremely well; our best global fit has an error norm: $||\theta_{\text{exp}} - \theta_{\text{num}}||_2 < 0.05$ for both electric field *on* and *off* scenarios in [28] and electric

field *off* scenario in [9]. We note that the "best fit" provided by our model for Ref. [28] is obtained using a highly nonlinear gliding model (large value of $n$) . Smaller values of $n$ can be used to capture the gliding dynamics, at the expense of somewhat higher error norms.

# CHAPTER 6

# CONCLUSION

In this dissertation, we develop a mathematical model that describes the evolution of a director field within a layer of nematic liquid crystal bounded between two parallel plates, where an external field may be applied across the layer. Such setup is important in LCD technology since it is representative of a single pixel in an LCD display. As such, we study the effect of an applied field and the effect of director gliding on a NLC layer.

In Chapter 3 we investigate how flexoelectricity affects the evolution of the director field for strong and weak anchoring, as well as the number and type of director configurations present in a NLC layer. We initially consider a special type of NLC layer (a Freedericksz Transition cell) and investigate how flexoelectricity affects the solution structure of the cell. We observe that the solution $\theta_h$ is stable for $0 < \mathcal{F} < \mathcal{F}_f$ (the Freedericksz transition threshold); solution $\theta_n$ is stable for $\mathcal{F}_f < \mathcal{F} < \mathcal{F}_s$ (the saturation threshold) and solution $\theta_v$ is stable for $\mathcal{F} > \mathcal{F}_s$. Also, the Freedericksz and saturation thresholds ($\mathcal{F}_f$ and $\mathcal{F}_s$) increase with stronger flexoelectric effect. We extend the investigation to include the effect of flexoelectricity on a general NLC layer, by allowing the anchoring conditions to vary at each boundary. We observe that varying the anchoring conditions can change the structure and stability of the possible director configurations. In some cases, the horizontal and vertical states are no longer solutions; in other cases, the system permits bistability (two stable director configurations). In cases where bistability is observed, we find that the system remains bistable for weak electric fields and loses bistability as the electric field is increased.

In Chapters 4 and 5, we describe the evolution of the director field within a confined NLC layer, bounded by two polymer-coated plates where director gliding may occur. Director gliding can occur due to a prolonged exposure of the NLC layer

to an external field or as result of the NLC layer having different anchoring conditions (specifically different anchoring angles) at each boundary. Each case may lead to the formation of "ghost images" that can form over a long period of time in LCD displays. These images would be more prominent in the case of flexible (polymer-based) LCD displays.

In Chapter 4, we present two models in the form of two ordinary differential equations that aim to capture the gliding dynamics that may arise due to different anchoring conditions prescribed at each substrate. Both models assume that gliding occurs at a rate proportional to the difference between the anchoring angle and the director angle at the interface and that gliding does not occur indefinitely; instead gliding stops after some time, as shown in [27] and [28]. The main difference between the presented models is the way they describe the intermediate dynamics of director gliding: in Model I, gliding stops abruptly as the anchoring angle reaches its allowed maximal amount of deviation (dictated by a parameter $\alpha_{\text{tol}}$) while in Model II, gliding is halted smoothly as $\alpha_{\text{tol}}$ is approached. Using both models, we investigate how director gliding affects the evolution of the director field, as model parameters vary. Particular attention is paid to the behavior under gliding of an initially bistable system. In this case, we find that gliding may destroy bistability.

In Chapter 5, we consider the experimental evidence of zenithal gliding in the presence of an electric field [9, 28] and develop a mathematical model (similar to Model II presented in Chapter 4) to describe the slow orientation of the easy axis under gliding. We investigate in detail how the easy axis evolves in time under the gliding model and compare our numerical results with the experimental data observed in Ref. [9, 28]. We observe that given the appropriate parameter values for each experiment, our gliding model predicts the zenithal gliding observed in [9, 28] very well for both electric field *on* and *off* scenarios.

In the future, our models can be extended to a more realistic three-dimensional geometry. Our current models, while useful, are restrictive since they do not allow for the director field to "twist" out of its bounding plane (to a potentially lower energy, more stable, configuration). Thus, it is possible that some of the states that are allowable within our current framework may not be stable to perturbations within a more general 3D framework. In 3D, two angles are required to characterize the director field: the polar angle $\theta$ introduced in this work, and additional azimuthal angle $\phi$, not considered here. The energetics of this director field are well-known; however a study into the effect of director gliding in 3D geometry has not been carried out. An important future direction of this research is to develop a mathematical model that accurately describes the phenomenon of director gliding in 3D geometry while addressing possible challenges that arise in this setup.

# APPENDIX A

# ANALYTICAL APPROACH

We augment our numerical approach in Chapter 3 by two analytical approaches to determine the stability of the steady solutions to Equation (3.2). The first consists of using the calculus of variations to calculate the first and second variation of the total free energy of the system. In certain cases we can show that the second variation of a particular solution $\theta$ (a zero of the first variation) is either strictly positive (energy minimum; stable) or strictly negative (energy maximum; unstable).

We also use linear stability analysis (LSA) as our second approach where we linearize Equations (3.2) around the two solutions that are known explicitly ($\theta_v(z,t) = 0$, $\theta_h(z,t) = \pi/2$) and seek to determine whether perturbations to these solutions exhibit growth or decay in time.

## A.1 Calculus of Variations

We determine the stability of the steady solutions $\theta_v(z) = 0$ and $\theta_h(z) = \pi/2$ in the presence of an external field. Since we will consider only the equilibrium solutions, we omit the $t$ dependence. The total free energy for our system is given by

$$J = \int_0^1 W(\theta, \theta_z)\, dz + g_0(\theta)|_{z=0} + g_1(\theta)|_{z=1}, \tag{A.1}$$

where $W$, $g_0$ and $g_1$ are the dimensionless bulk and surface energy densities obtained by nondimensionalizing Equation (2.4) using the scales in Equations (3.1):

$$W = \frac{\theta_z^2}{2} - \mathcal{D}\cos^2\theta + \frac{\mathcal{F}\theta_z}{2}\sin 2\theta, \tag{A.2}$$

$$g_{\{0,1\}} = \frac{\mathcal{A}_{\{0,1\}}}{2}\sin^2(\theta - \alpha_{\{0,1\}}). \tag{A.3}$$

We look for equilibrium solutions $\theta(z)$ that minimize $J$ as follows: let $\theta(z) \to \theta(z) + \epsilon\eta(z)$ $(0 < \epsilon \ll 1)$: this assumption leads to $J \to J[\theta + \epsilon\eta] = J_0 + \epsilon J_1 + \epsilon^2 J_2 + \mathcal{O}(\epsilon^3)$. For $\theta(z)$ to be a minimizer of $J$ (a stable solution), we require $J_1 = 0$ and $J_2 > 0$ for all admissible variations $\eta$. If on the other hand $J_2 < 0$ then we have a local maximum of the free energy, and hence an unstable steady solution. After Taylor expansion, the expression for $J_1$ takes the following form:

$$J_1 = \int_0^1 \eta(W_\theta - (W_{\theta_z})_z)\, dz + \eta(g_{1\theta} + W_{\theta_z})|_{z=1} + \eta(g_{0\theta} - W_{\theta_z})|_{z=0}. \tag{A.4}$$

After integration by parts, the second variation $J_2$ can be expressed as follows:

$$\begin{aligned} J_2 = {} & \tfrac{1}{2}\int_0^1 \{\eta^2[W_{\theta\theta} - (W_{\theta\theta_z})_z] + {\eta_z}^2 W_{\theta_z\theta_z}\}\, dz + \eta^2(g_{1\theta\theta} + W_{\theta\theta_z})|_{z=1} \\ & + \eta^2(g_{1\theta\theta} - W_{\theta\theta_z})|_{z=0}. \end{aligned} \tag{A.5}$$

We check the stability of the director solution $\theta_v(z) = 0$ and $\theta_h(z) = \pi/2$ by evaluating $J_2$ when $\alpha_{\{0,1\}} = \pi/2$ ($J_1$ must always vanish for any steady solution).

### A.1.1 Stability of Director Solution $\theta_v(z) = 0$

Substituting $W$ and $g_{\{0,1\}}$ given by Equations (A.2)–(A.3) into $J_1$ and $J_2$ (see Equations (A.4-A.5)) and manipulating the expressions, we first verify that $J_1 = 0$ for $\theta(z) = 0$, and that $J_2 > 0$ for sufficiently large $\mathcal{F}$. The first and second variations are evaluated as:

$$\begin{aligned} J_1 = {} & \int_0^1 \eta[\mathcal{D}\sin 2\theta - \theta_{zz}]dz + \eta\left(\frac{\mathcal{A}_1}{2}\sin 2(\theta - \alpha_1) + \theta_z + \frac{\mathcal{F}}{2}\sin 2\theta\right)|_{z=1} \\ & + \eta\left(\frac{\mathcal{A}_0}{2}\sin 2(\theta - \alpha_0) - \theta_z - \frac{\mathcal{F}}{2}\sin 2\theta\right)|_{z=0}, \end{aligned} \tag{A.6}$$

$$J_2 = \frac{1}{2}\int_0^1 \eta^2[2\mathcal{D}\cos 2\theta - 2\mathcal{F}\theta_z \sin 2\theta - 2\mathcal{F}\theta_z \cos 2\theta]\, dz$$
$$+ \frac{1}{2}\int_0^1 \eta_z^2\, dz + \eta^2(\mathcal{A}_1 \cos 2(\theta - \alpha_1) + \mathcal{F}\cos 2\theta)|_{z=1} \qquad \text{(A.7)}$$
$$+ \eta^2(\mathcal{A}_0 \cos 2(\theta - \alpha_0) - \mathcal{F}\cos 2\theta)|_{z=0}.$$

We assume that the two surface energies are equal, $\mathcal{A}_0 = \mathcal{A}_1$. Setting $\theta = \theta_v = 0$, $J_1 = 0$ and $J_2$ simplifies to:

$$J_2 = \frac{1}{2}\int_0^1 \{2\frac{\mathcal{F}^2}{\Upsilon}\eta^2 + \eta_z^2\}\, dz - \frac{\mathcal{A}}{2}(\eta^2|_{z=1} + \eta^2|_{z=0}) + \frac{\mathcal{F}}{2}(\eta^2|_{z=1} - \eta^2|_{z=0}). \qquad \text{(A.8)}$$

Observe that the first term in Equation (A.8) dominates for larger $|\mathcal{F}|$ and we conclude the following: when $|\mathcal{F}|$ is sufficiently large and for finite anchoring strength $\mathcal{A}$ and finite values of $\Upsilon$, $J_2 > 0$. This establishes that $\theta(z) = 0$ is a minimum energy solution and therefore stable.

Similarly, we can determine the sign of $J_2$ in the limiting case when $\mathcal{F} \to 0$ and anchoring is sufficiently strong. We obtain:

$$J_2 \approx \frac{1}{2}\int_0^1 \eta_z^2\, dz + \eta^2(-\mathcal{A} + \mathcal{F})|_{z=1} + \eta^2(-\mathcal{A} - \mathcal{F})|_{z=0}$$

for $|\mathcal{F}| \ll \mathcal{A}$, which leads to the following result: when $|\mathcal{F}|$ is sufficiently small and simultaneously $\mathcal{A}$ is sufficiently large, $J_2 < 0$ and $\theta(z) = 0$ is a solution locally maximizing the free energy and therefore unstable.

### A.1.2 Stability of Director Solution $\theta_h(z) = \pi/2$

A similar approach is taken to determine the stability of $\theta_h(z) = \pi/2$ for large $|\mathcal{F}|$. We first check that $J_1 = 0$ for $\theta_h(z) = \pi/2$, which a glance at Equation (A.6) confirms. Calculating the second variation $J_2$ for $\theta_h(z) = \pi/2$ by letting $\mathcal{D} = \mathcal{F}^2/\Upsilon$ and $\mathcal{A}_0 = \mathcal{A}_1$ in Equation (A.7), we obtain:

$$J_2 \;\; = \tfrac{1}{2}(\textstyle\int_0^1 -2\frac{\mathcal{F}^2}{\Upsilon}\eta^2\, dz + \int_0^1 \eta_z^2\, dz + \eta^2(\mathcal{A} - \mathcal{F})|_{z=1} + \eta^2(\mathcal{A} + \mathcal{F})|_{z=0}). \qquad \text{(A.9)}$$

As before we conclude that when $|\mathcal{F}|$ is sufficiently large and $\mathcal{A}$ is finite, $J_2 < 0$, establishing that $\theta_h(z) = \pi/2$ is a local energy maximizer and therefore unstable.

Similarly we can determine the sign of $J_2$ for $\theta(z) = \pi/2$ in the limiting case when $\mathcal{F} \to 0$. We obtain from Equation (A.9),

$$J_2 \approx \int_0^1 \eta_z^2 \, dz + \eta^2(\mathcal{A} - \mathcal{F})|_{z=1} + \eta^2(\mathcal{A} + \mathcal{F})|_{z=0}$$

and we conclude: when $|\mathcal{F}|$ is sufficiently small and simultaneously $\mathcal{A}$ is sufficiently large, $J_2 > 0$ and $\theta_h(z) = \pi/2$ is a solution locally minimizing the free energy and therefore stable.

Together with the numerical results, we can conclude that in the presence of a strong electric field ($|\mathcal{F}|$ sufficiently large), $\theta_v(z) = 0$ is a stable solution while $\theta_h(z) = \pi/2$ is unstable. If stronger anchoring is imposed on the boundaries, then a larger value of $|\mathcal{F}|$ is needed for $\theta_v(z) = 0$ to become stable. In addition, in the presence of a weak electric field ($|\mathcal{F}|$ sufficiently small), and $\mathcal{A}$ sufficiently large, the director solution $\theta_v(z) = 0$ is an unstable solution while $\theta_h(z) = \pi/2$ is stable. We observed numerically that in the presence of weak anchoring, the saturation threshold increased with $\mathcal{A}$ and $\Upsilon$ and although we cannot arrive to the same conclusion analytically, we observe that the sign of $J_2$ depends heavily on the anchoring and electric field strength indicating that the stability of the solutions depends strongly on the parameters $\mathcal{A}, \mathcal{F}$.

## A.2 Linear Stability Analysis

We now use linear stability analysis (LSA) to determine if the director solutions $\theta_v(z) = 0$ and $\theta_h(z) = \pi/2$ pertaining to a system with weak anchoring ($\mathcal{A}_{\{0,1\}} = 5.0$) are stable or unstable. We consider planar anchoring angles $\alpha_0 = \alpha_1 = \pi/2$ and various electric field strengths, always keeping $\Upsilon = 1$. We approach the problem as follows: consider a perturbation of the steady state solution $\theta_0$ of the following form:

$$\theta = \theta_0 + \varepsilon\omega(z, t), \tag{A.10}$$

where $\varepsilon \ll 1$. Substituting Equation (A.10) into Equations (3.2) and retaining only the order $\varepsilon$ terms, we obtain the following linear system:

$$\begin{aligned}
\tilde{\nu}\omega_t(z,t) &= \omega_{zz}(z,t) - 2\mathcal{D}\,\cos 2\theta_0 \omega(z,t), \\
\tilde{\nu}\omega_t(0,t) &= \omega_z(0,t) + (-\mathcal{A}_0 \cos 2(\theta_0 - \alpha_0) + \mathcal{F}\cos 2\theta_0)\,\omega(0,t), \\
-\tilde{\nu}\omega_t(1,t) &= \omega_z(1,t) + (\mathcal{A}_1 \cos 2(\theta_0 - \alpha_1) + \mathcal{F}\cos 2\theta_0)\,\omega(1,t).
\end{aligned} \tag{A.11}$$

We solve the linear boundary value problem given by Equations (A.11) for $\theta_0 = \theta_{v,h}(z) = 0, \pi/2$ and determine whether perturbations to each solution $\theta_0(z)$ grow or decay in time. Specifically, we look for solutions of the following form:

$$\omega_1(z,t) = e^{(k^2 - 2D\cos 2\theta_0)t}[A\cosh kz + B\sinh kz], \tag{A.12}$$

$$\omega_2(z,t) = e^{(-k^2 - 2D\cos 2\theta_0)t}[A\cos kz + B\sin kz]. \tag{A.13}$$

Each solution $\omega_i(z,t)$, $i = 1, 2$ satisfies the linear system given by Equation (A.11) provided that the coefficients $A$ and $B$ are chosen to satisfy the boundary conditions. We now consider each case in detail.

### A.2.1 Perturbation of Hyperbolic Type, Equation (A.12)

To obtain a nontrivial solution of type (A.12), we need to solve the following expression:

$$\begin{aligned}
D_1 \equiv \mathrm{Det}(\omega_1) &= [\mathrm{k}^2 - 2\mathcal{D}\cos 2\theta_0 + \mathcal{A}_0 \cos 2(\theta_0 - \alpha_0) - \mathcal{F}\cos 2\theta_0)] \\
&\times [(k^2 - 2\mathcal{D}\cos 2\theta_0)\tanh(k) + k + (\mathcal{A}_1 + \cos 2(\theta_0 - \alpha_1) + \mathcal{F}\cos 2\theta_0)\tanh(k)] \\
&+ k[(k^2 - 2\mathcal{D}\cos 2\theta_0 + \mathcal{A}_1 \cos 2(\theta_0 - \alpha_1) + \mathcal{F}\cos 2\theta_0 + k\tanh(k)] = 0
\end{aligned} \tag{A.14}$$

and find nonzero values of $k$ that correspond to nontrivial solutions of Equation (A.11). We find the values of $k$ using the bisection method and observe that the evolution of $\omega_1(z,t)$ in time is driven by the exponential term $e^{(k^2 - 2\mathcal{D}\cos 2\theta_0)t}$. Specifically, if $k^2 - 2\mathcal{D}\cos 2\theta_0 < 0$ for nonzero values of $k$ that satisfy Equation (A.14) then the

perturbation $\omega_1(z,t) \to 0$ as $t \to \infty$. Similarly, if $k^2 - 2\mathcal{D}\cos 2\theta_0 > 0$ for nonzero $k$ satisfying Equation (A.14) then $\omega_1(z,t) \to \infty$ as $t \to \infty$. Note that when $k = 0$, the perturbation $\omega_1(z,t) = Ae^{(-2\mathcal{D}\cos 2\theta_0)t}$ does not satisfy the boundary value problem given by Equation (A.11) unless the coefficient $A$ is zero, giving the zero solution. Before we can draw any conclusions about the stability of each director solution, we must also consider perturbations given by Equation (A.13).

### A.2.2 Perturbation of Oscillatory Type, Equation (A.13)

Similarly, to obtain a nonzero solution for Equation (A.13), we need to solve the following expression:

$$\begin{aligned} D_2 \equiv \mathrm{Det}(\omega_2) &= [k^2 + 2\mathcal{D}\cos 2\theta_0 - \mathcal{A}_0 \cos 2(\theta_0 - \alpha_0) + \mathcal{F}\cos 2\theta_0] \\ &\times [(k^2 + 2\mathcal{D}\cos 2\theta_0 - \mathcal{A}_1 \cos 2(\theta_0 - \alpha_1) + \mathcal{F}\cos 2\theta_0)\sin(k) - k\cos(k)] \\ &- k[(k^2 + 2\mathcal{D}\cos 2\theta_0 - \mathcal{A}_1 \cos 2(\theta_0 - \alpha_1) + \mathcal{F}\cos 2\theta_0)\cos(k) + k\sin(k)] = 0. \end{aligned} \tag{A.15}$$

Again, Equation (A.15) is solved numerically using the bisection method to determine the nonzero values of $k$ that allow for nontrivial solutions for Equation (A.11). Now the evolution of $\omega_2(z,t)$ in time is driven by the exponential term $e^{(-k^2 - 2\mathcal{D}\cos 2\theta_0)t}$. If $-k^2 - 2\mathcal{D}\cos 2\theta_0 > 0$ for nonzero values of $k$ that satisfy Equation (A.15) then the perturbation $\omega_2(z,t) \to \infty$ as $t \to \infty$. Similarly, if $-k^2 - 2\mathcal{D}\cos 2\theta_0 < 0$ then the perturbation $\omega_2(z,t) \to 0$ as $t \to \infty$.

### A.2.3 Stability of Solutions $\theta_v(z) = 0$ and $\theta_h(z) = \pi/2$ using Linear Stability Analysis

We determine the stability of the steady solutions $\theta_v(z) = 0$ and $\theta_h(z) = \pi/2$ by combining the results obtained for both perturbations $\omega_i(z,t), i = 1, 2$ as follows: if both exponents in $\omega_i(z,t)$ are negative (i.e., $k^2 - 2\mathcal{D}\cos 2\theta_0 < 0$ and $-k^2 - 2\mathcal{D}\cos 2\theta_0 < 0$) for nontrivial values of $k$ that satisfy Equations (A.14) and (A.15) respectively, then

the perturbations $\omega_i(z,t)$ decay in time leading to a stable steady state $\theta(z)$. If at least one expression is positive, then at least one perturbation $\omega_i(z,t)$ grows in time leading to an unstable steady state. We now present two tables that display the values of $k$ that satisfy Equation (A.11) for each perturbation $\omega_i(z,t), i = 1, 2$. In addition, we present the evolution of each perturbation as $t \to \infty$ to determine the stability of each director solutions: $\theta_v(z) = 0$ and $\theta_h(z) = \pi/2$ for different electric field strengths.

**Table A.1** Evolution of $\omega_1(z,t) = e^{(k^2 - 2\mathcal{D}\cos 2\theta_0)t}[A\cosh kz + B\sinh kz]$ for $\theta_0 = 0$ and $\theta_0 = \pi/2$ for Weak Anchoring $\mathcal{A}_0 = \mathcal{A}_1 = 5$ and Different Electric Field Strengths, Always with $\Upsilon = 1$

| $\theta(z)$ | $\alpha_0$ | $\alpha_1$ | $\mathcal{F}$ | $\mathcal{D}$ | $k$ | $\lim_{t\to\infty}\omega_1(z,t)$ |
|---|---|---|---|---|---|---|
| 0 | $\pi/2$ | $\pi/2$ | 1 | 1 | $\pm$1.9538, $\pm$2.3815 | $\infty$, $\infty$ |
| $\pi/2$ | $\pi/2$ | $\pi/2$ | 1 | 1 | 0 | N/A |
| 0 | $\pi/2$ | $\pi/2$ | 5 | 25 | $\pm$6.5887, $\pm$7.2620 | 0, $\infty$ |
| $\pi/2$ | $\pi/2$ | $\pi/2$ | 5 | 25 | 0 | N/A |
| 0 | $\pi/2$ | $\pi/2$ | 9 | 81 | $\pm$12.0797, $\pm$12.7759 | 0, $\infty$ |
| $\pi/2$ | $\pi/2$ | $\pi/2$ | 9 | 81 | 0 | N/A |
| 0 | $\pi/2$ | $\pi/2$ | 20 | 400 | $\pm$27.5223, $\pm$28.2271 | 0, 0 |
| $\pi/2$ | $\pi/2$ | $\pi/2$ | 20 | 400 | 0 | N/A |

Based on our LSA results shown in Tables (A.1–A.2), for parameter values $\mathcal{F} = \mathcal{D} = 1$ and symmetric anchoring conditions, we conclude that $\theta_v(z) = 0$ is an unstable steady state and $\theta_h(z,t) = \pi/2$ a stable state. As we increase the electric field strength to $\mathcal{F} = 5$, $\mathcal{D} = 25$ and $\mathcal{F} = 9$, $\mathcal{D} = 81$, we observe that neither

$\theta_v(z) = 0$ nor $\theta_h(z) = \pi/2$ are stable. In fact our numerical results show that $\theta_n(z)$ is the stable solution in this case. Moreover, for a higher electric field strength $\mathcal{F} = 20$ and $\mathcal{D} = 400$, LSA shows that $\theta_v(z) = 0$ is a stable state while $\theta_h(z)$ is unstable. Note that for all choices of $\mathcal{F}$, $\mathcal{D}$ used here, the material parameter $\Upsilon = 1$.

**Table A.2** Evolution of $\omega_2(z,t) = e^{(-k^2-2\mathcal{D}\cos 2\theta_0)t}[A\cos kz + B\sin kz]$ for $\theta_0 = 0$ and $\theta_0 = \pi/2$ for Weak Anchoring $\mathcal{A}_0 = \mathcal{A} = 1 = 5$ and Different Electric Field Strengths, with $\Upsilon = 1$

| $\theta(z)$ | $\alpha_0$ | $\alpha_1$ | $\mathcal{F}$ | $\mathcal{D}$ | $k$ | $\lim_{t\to\infty}\omega_2(z,t)$ |
|---|---|---|---|---|---|---|
| 0 | $\pi/2$ | $\pi/2$ | 1 | 1 | $\pm 3.4842$, $\pm 6.5394$, others | 0, 0, 0 |
| $\pi/2$ | $\pi/2$ | $\pi/2$ | 1 | 1 | $\pm 2.0930$, $\pm 2.8918$, others | 0, 0, 0 |
| 0 | $\pi/2$ | $\pi/2$ | 5 | 25 | $\pm 3.2333$, $\pm 6.4098$, others | 0, 0, 0 |
| $\pi/2$ | $\pi/2$ | $\pi/2$ | 5 | 25 | $\pm 3.0228$, $\pm 5.8396$, others | $\infty$, $\infty$, 0 |
| 0 | $\pi/2$ | $\pi/2$ | 9 | 81 | $\pm 13.1757$, $\pm 6.3418$, others | 0, 0, 0 |
| $\pi/2$ | $\pi/2$ | $\pi/2$ | 9 | 81 | $\pm 3.1704$, $\pm 6.1932$, others | $\infty$, $\infty$, 0 |
| 0 | $\pi/2$ | $\pi/2$ | 20 | 400 | $\pm 3.1491$, $\pm 6.2977$, others | 0, 0, 0 |
| $\pi/2$ | $\pi/2$ | $\pi/2$ | 20 | 400 | $\pm 3.1339$, $\pm 6.26723$, others | $\infty$, $\infty$, 0 |

Although these analytical approaches are very useful to validate our numerical results, they have their limitations. In the case of the calculus of variations method, we are able to draw conclusions only in the limiting cases where $|\mathcal{F}|$ is small or large compared to the anchoring strength $\mathcal{A}_{\{0,1\}}$. When using LSA, we are able to linearize only around known solutions, namely $\theta(z) = 0, \pi/2$ and for symmetric anchoring conditions only. We still rely on our numerical investigation to determine the stability of the nontrivial steady state as well as asymmetric boundary conditions.

# BIBLIOGRAPHY


[1] http://www.mit.edu/~6.777/matprops/polyimide.htm. (Accessed on November 28, 2016).

[2] Advances in display technologies; and e-papers and flexible displays. *Proc. SPIE Conf.*, 7956(4):613–618, 2011.

[3] Data thief III. http://datathief.org, 2015. (Accessed on November 28, 2016).

[4] K. E. Atkinson. *An Introduction to Numerical Analysis*. Wiley, Hoboken, NJ, 1989.

[5] L. M. Blinov and V. Chigrinov. *Electrooptic Effects in Liquid Crystal Materials*. Springer, New York, NY, 1994.

[6] C. V. Brown and N. J. Mottram. Influence of flexoelectricity above the nematic Freedericksz transition. *Phys. Rev. E*, 68(31):317021–317025, 2003.

[7] G. P. Bryan-Brown, C. V. Brown, and J. C. Jones. Zenithal bistable device. *U.S. Patent 6249332*, 1995.

[8] A. Buka and N. Éber. *Flexoelectricity in Liquid Crystals: Theory, Experiments and Applications*. Imperial College Press, London, UK, 2013.

[9] O. Buluy, A. Iljin, E. Ouskova, Y. Reznikov, C. Blanc, M. Nobili, and K. Antonova. Anchoring and gliding of easy axis of 5CB on photoaligning PVCN-F surface. *J. Soc. Inf. Disp.*, 14(7):603–610, 2006.

[10] S. Chandrasekhar. *Liquid Crystals*. Cambridge University Press, Cambridge, UK, 2007.

[11] M. C. Choi, Y. Kim, and C. S. Ha. Polymers for flexible displays: From material selection to device applications. *Prog. Poly. Sci.*, 33(6):581–630, 2008.

[12] L. J. Cummings, C. Cai, and L. Kondic. Bifurcation properties of nematic liquid crystals exposed to an electric field: Switchability, bistability, and multistability. *Phys. Rev. E*, 88(1):012509, 2013.

[13] L. J. Cummings, C. Cai, and L. Kondic. Towards an optimal model for a bistable nematic liquid crystal display device. *J. Eng. Math.*, 80(1):21–38, 2013.

[14] L. J. Cummings, E. Mema, C. Cai, and L. Kondic. Electric-field variations within a nematic-liquid-crystal layer. *Phys. Rev. E*, 90(1):012503, 2014.

[15] L. J. Cummings and G. Richardson. Bistable nematic liquid crystal device with flexoelectric switching. *Eur. J. Appl. Math*, 17(4):435–463, 2006.

[16] F. P. Da Costa, M. Grinfeld, N. J. Mottram, and J. T. Pinto. Uniqueness in the Freedericksz transition with weak anchoring. *J. Differ. Equations*, 246(7):2590–2600, 2009.

[17] A. J. Davidson and N. J. Mottram. Flexoelectric switching in a bistable nematic device. *Phys. Rev. E*, 65(5):051710, 2002.

[18] P. G. De Gennes and J. Prost. *The physics of liquid crystals*. Oxford University Press, New York, NY, 1995.

[19] A. Derzhanski, A. G. Petrov, and M. D. Mitov. One-dimensional dielectric-flexoelectric defomations in nematic layers. *J. Phys. (Paris)*, 39(3):273–285, 1978.

[20] G. E. Durand and E. G. Virga. Hydrodynamic model for surface nematic viscosity. *Phys. Rev. E*, 59(4):4137–4142, 1999.

[21] J. L. Ericksen. Theory of anisotropic fluids. *J. Rheol.*, 4(1):29–39, 1960.

[22] S. Faetti, M. Nobili, and I. Raggi. Surface reorientation dynamics of nematic liquid crystals. *Eur. Phys. J. B*, 11(3):445–453, 1999.

[23] V. Fréedericksz and A. Repiewa. Theoretisches und experimentelles zur frage nach der natur der anisotropen flüssigkeiten. *Z. Phys.*, 42(7):532–546, 1927.

[24] J. S. Gwag, J. H. Kim, M. Yoneya, and H. Yokoyama. Surface nematic bistability at nanoimprinted topography. *Appl. Phys. Lett.*, 92(15):153110, 2008.

[25] I. Jánossy. High-precision measurement of azimuthal rotation of liquid crystals on solid substrates. *J. App. Phys.*, 98(4):043523, 2005.

[26] I. Jánossy. Kinetics of director gliding on a polymer liquid-crystal interface. *Phys. Rev. E*, 81:031714, 2010.

[27] I. Jánossy and T. I. Kósa. Gliding of liquid crystals on soft polymer surfaces. *Phys. Rev. E*, 70:052701, 2004.

[28] S. Joly, K. Antonova, P. Martinot-Lagarde, and I. Dozov. Zenithal gliding of the easy axis of a nematic liquid crystal. *Phys. Rev. E*, 70(51):050701, 2004.

[29] P. J. Kedney and F. M. Leslie. Switching in a simple bistable nematic cell. *Liq. Cryst.*, 24(4):613–618, 1998.

[30] Y. Kurioz, V. Reshetniak, and Y. Reznikov. Orientation of a liquid crystal on a soft photoaligning surface. *Mol. Cryst. Liq. Cryst. Sci. Technol., Sect. A*, 375:535–541, 2002.

[31] J. H. Lee and T. H. Yoon. P-77: Image sticking in a flexible liquid crystal display stabilized with polymers: Surface gliding effect. *SID Int. Sym. Dig. Tec.*, 43(1):1343–1345, 2012.

[32] F. M. Leslie. Some constitutive equations for anisotropic fluids. *Q. J. Mech. Appl. Math*, 19(3):357–370, 1966.

[33] F. M. Leslie. Some constitutive equations for liquid crystals. *Arch. Rational Mech. Anal.*, 28(4):265–283, 1968.

[34] R. B. Meyer. Piezoelectric effects in liquid crystals. *Phys. Rev. Lett.*, 22(18):918–921, 1969.

[35] G. Napoli. Weak anchoring effects in electrically driven Freedericksz transitions. *J. Phys. A: Mathematical and General*, 39(1):11–31, 2006.

[36] P. Palffy-Muhoray. The diverse world of liquid crystals. *Phys. Today*, 60(9):54–60, 2007.

[37] S. V. Pasechnik, V. G. Chigrinov, and D. V. Shmeliova. *Liquid Crystals: Viscous and Elastic Properties*. Wiley-VCH, Weinheim, Germany, 2009.

[38] S. V. Pasechnik, V. G. Chigrinov, D. V. Shmeliova, V. A. Tsvetkov, V. N. Kremenetsky, L. Zhijian, and A. V. Dubtsov. Slow relaxation processes in nematic liquid crystals at weak surface anchoring. *Liq. Cryst.*, 33(2):175–185, 2006.

[39] S. V. Pasechnik, A. V. Dubtsov, D. V. Shmeliova, D. A. Semerenko, V. G. Chigrinov, M. A. Sinenko, and A. D. Kiselev. Modeling reorientation dynamics of electrically assisted light-induced gliding of nematic liquid-crystal easy axis. *Adv. Cond. Matter Phys.*, 2013:363157, 2013.

[40] A. Rapini and M. Papoular. Distorsion d'une lamelle nematique sous champ magnetique, conditions d'ancrage aux parois. *J. Phys. Colloq. (Paris)*, 30:54, 1969.

[41] I. W. Stewart. *The Static and Dynamic Continuum Theory of Liquid Crystals.* Taylor & Francis, London, UK, 2004.

[42] P. Vetter, Y. Ohmura, and T. Uchida. Study of memory alignment of nematic liquid crystals on polyvinyl alcohol coatings. *Jpn. J. Appl. Phys, Part 2: Letters*, 32(9A):L1239–L1241, 1993.

[43] V. P. Vorflusev, H. Kitzerow, and V. G. Chigrinov. Azimuthal surface gliding of a nematic liquid crystal. *Appl. Phys. Lett.*, 70(25):3359–3361, 1997.

[44] E. Willman, F. A. Fernandez, R. James, and S. E. Day. Switching dynamics of a post-aligned bistable nematic liquid crystal device. *J. Display Technol.*, 4(3):276–281, 2008.

[45] D. K. Yang and S. T. Wu. *Fundamentals of Liquid Crystal Devices*. John Wiley & Sons, 2006.

[46] P. Yeh and C. Gu. *Optics of Liquid Crystal Displays*. Wiley, Hoboken, NJ, 2009.